



HAL
open science

Study of passive microwave and millimetre wave components based on matematerials and ferrite

Tao Zhou

► **To cite this version:**

Tao Zhou. Study of passive microwave and millimetre wave components based on matematerials and ferrite. Other. INSA de Lyon, 2012. English. NNT : 2012ISAL0017 . tel-00782328

HAL Id: tel-00782328

<https://theses.hal.science/tel-00782328>

Submitted on 29 Jan 2013

HAL is a multi-disciplinary open access archive for the deposit and dissemination of scientific research documents, whether they are published or not. The documents may come from teaching and research institutions in France or abroad, or from public or private research centers.

L'archive ouverte pluridisciplinaire **HAL**, est destinée au dépôt et à la diffusion de documents scientifiques de niveau recherche, publiés ou non, émanant des établissements d'enseignement et de recherche français ou étrangers, des laboratoires publics ou privés.

Thèse

Présentée devant

L'institut national des sciences appliquées de Lyon

Pour obtenir le grade de

Docteur

École doctorale: Electronique, Electrotechnique et Automatique

Par

ZHOU Tao

**Etude de composants passifs hyperfréquences
à base de métamatériaux et de ferrite
(Study of passive microwave and millimeter wave
components based on metamaterials and ferrite)**

Soutenue le 6 Mars 2012 devant la Commission d'examen

Rapporteur	FLECHET Bernard	Professeur (Université de Savoie)
Examineur	CALMON Francis	Professeur (INSA de Lyon)
Rapporteur	PARRA Thierry	Professeur (Université Paul Sabatier)
Examineur	GAUTIER Brice	Professeur (INSA de Lyon)
Co-directeur de thèse	VINCENT Didier	Professeur (Telecom Saint-Etienne)
Directeur de thèse	LE BERRE Martine	Maître de conférences HdR (INSA de Lyon)

Laboratoire de recherche: UMR CNRS 5270, Institut des Nanotechnologies de Lyon

INSA Direction de la Recherche - Ecoles Doctorales – Quinquennal 2011-2015

SIGLE	ECOLE DOCTORALE	NOM ET COORDONNEES DU RESPONSABLE
CHIMIE	<p>CHIMIE DE LYON http://www.edchimie-lyon.fr</p> <p>Insa : R. GOURDON</p>	<p>M. Jean Marc LANCELIN Université de Lyon – Collège Doctoral Bât ESCPE 43 bd du 11 novembre 1918 69622 VILLEURBANNE Cedex Tél : 04.72.43 13 95 directeur@edchimie-lyon.fr</p>
E.E.A.	<p>ELECTRONIQUE, ELECTROTECHNIQUE, AUTOMATIQUE http://edeea.ec-lyon.fr</p> <p>Secrétariat : M.C. HAVGOUDOUKIAN eea@ec-lyon.fr</p>	<p>M. Gérard SCORLETTI Ecole Centrale de Lyon 36 avenue Guy de Collongue 69134 ECULLY Tél : 04.72.18 60 97 Fax : 04 78 43 37 17 Gerard.scorletti@ec-lyon.fr</p>
E2M2	<p>EVOLUTION, ECOSYSTEME, MICROBIOLOGIE, MODELISATION http://e2m2.universite-lyon.fr</p> <p>Insa : H. CHARLES</p>	<p>Mme Gudrun BORNETTE CNRS UMR 5023 LEHNA Université Claude Bernard Lyon 1 Bât Forel 43 bd du 11 novembre 1918 69622 VILLEURBANNE Cédex Tél : 04.72.43.12.94 e2m2@biomserv.univ-lyon1.fr</p>
EDISS	<p>INTERDISCIPLINAIRE SCIENCES- SANTE http://ww2.ibcp.fr/ediss</p> <p>Sec : Safia AIT CHALAL Insa : M. LAGARDE</p>	<p>M. Didier REVEL Hôpital Louis Pradel Bâtiment Central 28 Avenue Doyen Lépine 69677 BRON Tél : 04.72.68 49 09 Fax :04 72 35 49 16 Didier.revel@creatis.uni-lyon1.fr</p>
INFOMATHS	<p>INFORMATIQUE ET MATHEMATIQUES http://infomaths.univ-lyon1.fr</p>	<p>M. Johannes KELLENDONK Université Claude Bernard Lyon 1 INFOMATHS Bâtiment Braconnier 43 bd du 11 novembre 1918 69622 VILLEURBANNE Cedex Tél : 04.72. 44.82.94 Fax 04 72 43 16 87 infomaths@univ-lyon1.fr</p>
Matériaux	<p>MATERIAUX DE LYON</p> <p>Secrétariat : M. LABOUNE PM : 71.70 –Fax : 87.12 Bat. Saint Exupéry Ed.materiaux@insa-lyon.fr</p>	<p>M. Jean-Yves BUFFIERE INSA de Lyon MATEIS Bâtiment Saint Exupéry 7 avenue Jean Capelle 69621 VILLEURBANNE Cédex Tél : 04.72.43 83 18 Fax 04 72 43 85 28 Jean-yves.buffiere@insa-lyon.fr</p>
MEGA	<p>MECANIQUE, ENERGETIQUE, GENIE CIVIL, ACOUSTIQUE</p> <p>Secrétariat : M. LABOUNE PM : 71.70 –Fax : 87.12 Bat. Saint Exupéry mega@insa-lyon.fr</p>	<p>M. Philippe BOISSE INSA de Lyon Laboratoire LAMCOS Bâtiment Jacquard 25 bis avenue Jean Capelle 69621 VILLEURBANNE Cedex Tél :04.72.43.71.70 Fax : 04 72 43 72 37 Philippe.boisse@insa-lyon.fr</p>
ScSo	<p>ScSo*</p> <p>M. OBADIA Lionel</p> <p>Sec : Viviane POLSINELLI Insa : J.Y. TOUSSAINT</p>	<p>M. OBADIA Lionel Université Lyon 2 86 rue Pasteur 69365 LYON Cedex 07 Tél : 04.78.69.72.76 Fax : 04.37.28.04.48 Lionel.Obadia@univ-lyon2.fr</p>

*ScSo : Histoire, Géographie, Aménagement, Urbanisme, Archéologie, Science politique, Sociologie, Anthropologie

Remerciements

Cette thèse a été effectuée à l'Institut des Nanotechnologies de Lyon – INL (UMR CNRS 5270), dont le directeur est Monsieur Guy Hollinger, elle a été dirigé par Madame Martine LE BERRE et Monsieur Didier VINCENT. Je les remercie de m'avoir accueilli dans ce laboratoire et soutenu tout au long de mon travail.

Je voudrais remercier mon directeur de thèse, Madame Martine LE BERRE, Maître de conférences de l'INSA de LYON, pour m'avoir proposé ce sujet et pour avoir accepté de diriger ma thèse. Je la remercie d'avoir trouvé le temps, m'avoir conseillé et m'encouragé tout au long de mon travail. Je voudrais qu'elle trouve ici toute l'expression de ma reconnaissance.

Je tiens aussi à remercier mon co-directeur de thèse, Monsieur Didier VINCENT, Professeur à l'université Jean Monnet de Saint-Etienne, pour son soutien et son suivi.

Je remercie tout particulièrement Monsieur Francis CALMON, Professeur de l'INSA de LYON, qui a cordialement accepté d'être membre du jury lors de ma thèse.

J'adresse toute ma reconnaissance à Monsieur Brice GAUTIER, Professeur de l'INSA de LYON, qui a cordialement accepté d'être membre du jury lors de ma thèse.

Un très grand merci à Monsieur Bernard FLECHET, Professeur de l'Université de Savoie, et à Monsieur PARRA Thierry, Professeur de l'Université Paul Sabatier, qui ont cordialement accepté d'être rapporteur de ce travail.

Je tiens également à remercier madame Béatrice Payet-Gervy, Maître de conférences à l'université Jean Monnet de Saint-Etienne, pour son aide dans la partie mesure de cette thèse.

J'ai une énorme pensée pour toute ma famille, mes parents, et mes frères, sans qui je n'en serais pas là aujourd'hui.

Enfin, je terminerais en remerciant tous mes collègues pour les bons moments que nous avons partagés : Wael HOURANI, Wei XUAN, Fengyuan SUN, Ahmed GHARBI, Sylvain PELLOQUIN, Jean-Etienne LORIVAL, Hassan CHAMAS, Antonin GRANDFOND, Guillaume HYVERT.

A tous Merci...

Contents

General introduction

1 Basic concepts

1.1 Introduction

1.2 Transmission line theory

1.2.1 Traditional reciprocal transmission line

1.2.2 Nonreciprocal transmission line

1.2.3 Transmission line network analysis

1.2.3.1 Impedance and admittance matrices

1.2.3.2 Transmission matrix [ABCD]

1.2.3.3 Scattering and transfer matrices

1.3 Coplanar waveguide

1.3.1 Conventional coplanar waveguide

1.3.1.1 CPW has infinite-width ground planes

1.3.1.2 CPW has finite-width ground planes

1.3.1.3 Consideration of conductor thickness

1.3.1.4 Attenuation constant

1.3.2 Conductor backed coplanar waveguide

1.4 Magnetic material

1.4.1 Diamagnetism

1.4.2 Paramagnetism

1.4.3 Ferromagnetism and Ferrimagnetism

1.4.4 Antiferromagnetism

1.4.5 Ferrites

1.5 Metamaterials

1.5.1 Definition of metamaterials

1.5.2 History of metamaterials

1.5.3 Applications of metamaterials

1.5.3.1 Guided wave applications

1.5.3.2 Radiated wave applications

1.5.3.3 Other applications of interest

1.5.3.4 Example of the zeroth-order resonator

1.6 Conclusion

1.7 Bibliography

2 Conventional coplanar components on alumina

2.1 Introduction

2.2 Fabrication of coplanar components on alumina

2.2.1 Photolithography

2.2.2 Vacuum deposition / evaporation

2.3 Simulation and modelling

2.3.1 Finite element simulation

2.3.2 Modelling

2.3.2.1 Analytical modelling of CPW

2.3.2.2 Analytical modelling of gap capacitors

2.3.2.3 Analytical modelling of interdigital capacitors

2.3.2.4 Analytical modelling of shunt inductor

2.3.2.5 Calculation of capacitance and inductance from
S parameters

2.4 Results of coplanar components on alumina

2.4.1 CPW on alumina

2.4.1.1 S parameters

2.4.1.2 Propagation constant

2.4.1.3 Change in reference planes

2.4.2 Coplanar gap capacitor

2.4.2.1 Measured and simulated S parameters

2.4.2.2 Values of capacitance

2.4.3 Coplanar interdigital capacitor

2.4.3.1 Measured and simulated S parameters

2.4.3.2 Values of capacitance

2.4.4 Coplanar shunt inductor

2.4.4.1 Measured and simulated S parameters

2.4.4.2 Values of inductance

2.5 Conclusion

2.6 Bibliography

3 Coplanar components on ferrite

3.1 Introduction

3.2 Ferrite material

3.2.1 Spinel

3.2.2 Garnet

3.2.3 Hexaferrite

3.3 Fabrication of coplanar components on YIG

3.3.1 Polish of film

3.3.2 Fabrication of component

3.4 Modelling, simulation, and calculation

3.4.1 Modelling of ferrite material

3.4.2 Simulation

3.4.3 Calculation of propagation constant

3.5 Coplanar component on substrate ferrite

3.5.1 CPW on substrate BaM

3.5.1.1 Applied field out of the plane of CPW – filter

3.5.1.2 Applied field in the plane of CPW – isolator

3.5.2 CPW on YIG without applied Field

3.5.2.1 S parameters

3.5.2.2 Propagation constant

3.5.3 CPW on YIG with applied field in the plane of CPW

3.5.3.1 S parameters

3.5.3.2 Propagation constant

3.5.4 Coplanar gap capacitor on YIG

3.5.4.1 Measured and simulated S parameters

3.5.4.2 Values of capacitors

3.5.5 Coplanar inter-digital capacitor on YIG

3.5.5.1 Measured and calculated S parameters

3.5.5.2 Values of capacitors

3.5.6 Coplanar inductor on YIG

3.6 Conclusion

3.7 Bibliography

4 Coplanar composite right/left-handed metamaterials

4.1 Introduction

4.2 Modelling, simulation, and calculation

4.2.1 Transmission line approach of metamaterials

4.2.2 Simulation and calculation

4.2.3 Example

4.3 CRLH metamaterials on alumina

4.3.1 Equivalent circuits

4.3.2 Measured and simulated S parameters

4.3.3 Propagation constants

4.4 CRLH metamaterials on YIG without applied field

4.4.1 Equivalent circuits

4.4.2 Measured S parameters

4.4.3 Propagation constants

4.5 CRLH metamaterials on YIG with applied field

4.5.1 Measured S parameters

4.5.2 Propagation constants

4.6 Conclusion

4.7 Bibliography

General conclusion

List of publications

General introduction

This thesis concerns passive microwave and millimeter wave components based on ferrites and metamaterials. The main objective of this work is to study the physical properties of combined left-handed transmission lines associated with negative permeability ferrite. The modelling, fabrication and characterization of components have been achieved in collaboration between the INL and LT2C.

As a coplanar transmission line, coplanar waveguide (CPW) offers several attractive features, it is very suitable for microwave and millimeter wave components. The CPW can be easily use to integrate some basic lumped elements such as coplanar capacitors and shunt inductors, which can be easily applied to build composite right/left-handed transmission lines, filters, resonators... The properties of CRLH TL which consist of distributed structures with lumped components will be studied in this thesis: the equivalent circuits, the S parameters, the propagation constants.

Since the first microwave ferrite device was proposed in 1949, the ferrite materials have been applied to many microwave components such as isolators, circulators, phase shifters, and filters. The development of ferrite components was strongly related to the knowledge of spin interaction in ferrite materials. The ferrite materials are so important that, for some purposes, we can not find an alternative semiconductor device that satisfies similar requirements.

In the past 10 years, there has been a great deal of interest in the composite right/left-handed (CRLH) transmission lines (TLs) metamaterials (MTMs), which introduced by Caloz et al. and other groups. The CRLH TLs can be realized by using traditional right-handed (RH) TLs loaded with series capacitors (IDCs) and shunt inductors. Novel microwave applications like guided wave application and radiated wave application can be realized by using the unique features of MTMs, they exhibit new performance compared with similar classical devices, these novel CRLH components are couplers, zeroth order resonators, zeroth order antennas, leaky-wave antenna, filters etc.

In this thesis we propose several coplanar components based on metamaterials, with which we can get a novel property “left-handed” or “CRLH”. When the CRLH TLs are integrated with substrate ferrites, we expected a new property which combines the “CRLH” property and nonreciprocity together. We can get nonreciprocity by modeling the ferrite substrate, and “left-handed” property by modeling the structure of CRLH.

This manuscript contains four chapters. The first chapter of this manuscript will focus on theories of microwave transmission lines, coplanar waveguides, magnetic materials and general concepts about metamaterials. We will begin with the theories of traditional transmission lines and nonreciprocal transmission lines, and then we will present the analysis of transmission lines,

methods of calculation of the parameters characterizing wave propagation (matrix [Z] matrix [Y], matrix [ABCD] and matrix [S]). The classification of magnetic materials will be presented in different groups. Finally, we will introduce metamaterials. The definition, history, and some applications of metamaterials in microwave and millimetre wave will be indicated.

In the second chapter, we will present the conventional coplanar components on alumina substrate. We will start with the fabrication of components. Then we will simulate and modelize coplanar waveguides, capacitors, and inductors. Finally, we will discuss the calculated results, the simulated and measured CPW, capacitances, and inductances, we will compare the results.

In the third chapter, we focus on coplanar components on ferrite substrate. We will discuss the important characteristics of ferrite materials classified into different groups depending on their properties, and the main characteristics of ferrites used in this work. We will present the process of fabrication of components when it differs from the one on alumina. Then we will show simulations and modeling of coplanar waveguide on ferrite, coplanar capacitances and the behavior due to coplanar inductances on ferrite.

The fourth chapter is devoted to metamaterials based on the CRLH TL. This type of TL allows a negative phase velocity in a certain frequency band. We will make the modeling, 3D simulations, and parameter extraction of the CRLH metamaterial. Then we will present the CRLH TL on alumina and on YIG (with field and without applied field). The variations of the experimental and simulated parameters S , the propagation constants β as a function of frequency are presented.

1 Basic concepts

1.1 Introduction

Microwaves are electromagnetic waves with frequencies ranging from 300 MHz to 300 GHz (wavelengths: 1 m to 1 mm) [1]. This definition includes ultra high frequency (300 MHz-3 GHz, or 1 to 0.1m) [2], Super high frequency (3GHz-30 GHz, or 10cm to 1 cm) [3], and extremely high frequency (30 GHz-300GHz, or 10mm to 1mm) [4]. With RF engineering, the band from 300 MHz to 30 GHz is typically considered to be “microwaves”, the frequency band above 30 GHz is considered to be “millimetre waves”[2,4].

The tremendous growth in mobile communications during the past 20 years has caused a great increase in the need for microwave and millimetre wave components. Besides this, microwave and millimetre wave components are widely used in application areas, such as radar and navigation systems, satellite communication networks, remote sensing, and industrial measurements [5]. Microwave and millimetre wave components are becoming more available and affordable because of advances in the design, processing, testing, and packaging technology. There exist a lot of microwave and millimetre-wave components, for example, coplanar waveguides (CPWs) [6-14], metamaterials (MTMs) [15-22], components based on ferrite materials [1-3], as will be introduced in the coming chapter.

1.2 Transmission line theory

Transmission line (TL) is widely used in radio-frequency domains, the TL is a special cable designed to carry electromagnetic signals [1-10]. There are many types of TL such as coaxial cable [1-3], microstrip line [10], stripline [10] and waveguide [1-2]. The CPW [6-7] will be discussed in Chapter 2 and Chapter 3.

1.2.1 Conventional reciprocal TL

The TL theory bridges the gap between field analysis and circuit theory, it is very important in microwave and millimetre wave network analysis [1]. The wave propagate along the TL can be approached from a specialization of Maxwell’s equations or from an extension of circuit theory.

The key difference between the TL theory and the circuit theory is the electrical length. The physical length of a TL network may be a considerable fraction of a wavelength, or many wavelengths, while the circuit theory assumes that the physical length of a network is much smaller than the electrical

wavelength. The circuit theory is a lumped element network, while the TL is a distributed element network.

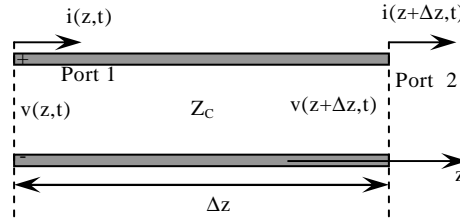


Figure 1.1 Transmission line

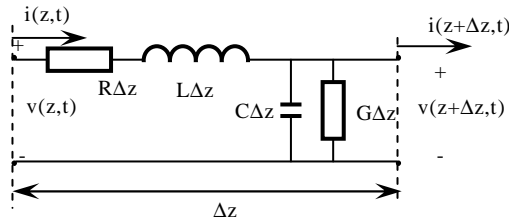


Figure 1.2 Equivalent circuit of TL

The TL is shown in Figure 1. 1, it's composed of 2-wire line, and since TL (for TEM propagation) wave propagation has at least 2 conductors [1]. The short line length Δz of TL can be modelled as a lumped element circuit consists of R, L, C and G, as shown in Figure 1.2.

where,

R is series resistance per unit length, in Ω/m , represents the resistance due to the finite conductivity of the 2 lines.

L is series inductance per unit length, in H/m , represents the self-inductance of the 2 lines.

C is shunt capacitance per unit length, in S/m , represents the capacitance due to the close proximity of the 2 lines.

G is shunt conductance per unit length, in F/m , represents the conductance due to the dielectric loss in the material between the 2 lines.

From the equivalent circuit of TL, for finding the voltage and current on the TL, Kirchhoff's voltage law (KVL) and Kirchhoff's current law (KCL) can be applied to get:

$$v(z + \Delta z, t) = v(z, t) - R \Delta z i(z, t) - L \Delta z \frac{\partial i(z, t)}{\partial t} \quad (1.1)$$

$$i(z + \Delta z, t) = i(z, t) - G \Delta z v(z + \Delta z, t) - C \Delta z \frac{\partial i(z + \Delta z, t)}{\partial t} \quad (1.2)$$

Dividing the 2 equations by Δz ($\Delta z \rightarrow 0$), the telegrapher equations-time domain form of TL are given:

$$\frac{v(z + \Delta z, t) - v(z, t)}{\Delta z} = -R i(z, t) - L \frac{\partial i(z, t)}{\partial t} = -R i(z, t) - j\omega L i(z, t) \quad (1.3)$$

$$\frac{i(z + \Delta z, t) - i(z, t)}{\Delta z} = -G v(z, t) - C \frac{\partial v(z, t)}{\partial t} = -G v(z, t) - j\omega C v(z, t) \quad (1.4)$$

For the sinusoidal steady-state condition (cosine-based phases), the 2 equations can be simplified as:

$$\frac{dV(z)}{dz} = -(R + j\omega L)I(z) = -ZI(z) \quad (1.5)$$

$$\frac{dI(z)}{dz} = -(G + j\omega C)V(z) = -YV(z) \quad (1.6)$$

where Z and Y are the series impedance and shunt admittance per unit length.

The 2 equations can be solved simultaneously to give wave equations of $V(z)$ and $I(z)$

$$\frac{d^2V(z)}{dz^2} - \gamma^2 V(z) = 0 \quad (1.7)$$

$$\frac{d^2I(z)}{dz^2} - \gamma^2 I(z) = 0 \quad (1.8)$$

where the complex propagation constant

$$\gamma = \alpha + j\beta = \sqrt{ZY} = \sqrt{(R + j\omega L)(G + j\omega C)} \quad (1.9)$$

Travelling wave solutions to wave equations of $V(z)$ and $I(z)$

$$V(z) = V_0^+ e^{-\gamma z} + V_0^- e^{\gamma z} \quad (1.10)$$

$$I(z) = I_0^+ e^{-\gamma z} + I_0^- e^{\gamma z} \quad (1.11)$$

Where V_0^+ , V_0^- , I_0^+ and I_0^- are unknown amplitudes of voltage and current waves of port 1 and port 2, the $e^{-\gamma z}$ and $e^{\gamma z}$ represents wave propagation in the +z direction, and wave propagation in the -z direction, respectively.

Applying Equation 1.5 to the equation 1.11 given

$$I(z) = \frac{\gamma}{R + j\omega L} (V_0^+ e^{-\gamma z} - V_0^- e^{\gamma z}) \quad (1.12)$$

Dividing the Equation 1.10 and Equation 1.11 with the equation 1.12, the characteristic impedance Z_c is given:

$$Z_c = \frac{R + j\omega L}{\gamma} = \sqrt{\frac{R + j\omega L}{G + j\omega C}} \quad (1.13)$$

$$\frac{V_0^+}{I_0^+} = \frac{V_0^-}{I_0^-} = \sqrt{\frac{Z}{Y}} = Z_c \quad (1.14)$$

The wavelength of TL is

$$\lambda_g = \frac{2\pi}{\beta} \quad (1.15)$$

The phase velocity

$$V_p = \lim_{\Delta t \rightarrow 0} \frac{\Delta z}{\Delta t} = \frac{\omega}{\beta} = \lambda_g f \quad (1.16)$$

The group velocity

$$V_g = \left(\frac{d\beta}{d\omega} \right)^{-1} = \frac{V_p}{1 - \frac{\omega}{v_g} \frac{dV_p}{d\omega}} \quad (1.17)$$

For a TL with infinite conductor conductivity ($\sigma \rightarrow \infty$), zero dielectric conductivity ($\sigma \rightarrow 0$) and no radiation loss, the loss of TL is very small and can be neglected, the circuit components (R and G) which represent loss become zero, $R = G = 0$

The corresponding propagation constant can be simplified as

$$\gamma = \alpha + j\beta = \sqrt{(R + j\omega L)(G + j\omega C)} = j\omega\sqrt{LC} \quad (1.18)$$

where the attenuation constant $\alpha = 0$, $\beta = \omega\sqrt{LC}$

The characteristic impedance of TL is a real number

$$Z_c = \sqrt{\frac{L}{C}} \quad (1.19)$$

The wavelength of lossless TL

$$\lambda_g = \frac{2\pi}{\beta} = \frac{2\pi}{\omega\sqrt{LC}} \quad (1.20)$$

The phase velocity

$$V_p = \frac{\omega}{\beta} = \frac{1}{\sqrt{LC}} \quad (1.21)$$

1.2.2 Novel nonreciprocal TL

Non reciprocal isotropic medium was first introduced by Tellegen in 1948 [23]. The realization of the gyrator by a new medium, which obtained by imbedding permanent electric and magnetic dipoles in a host medium, was discussed by him. The plane wave propagation in such medium was presented by Chambers in 1956 [24]. The theory of nonreciprocal and no symmetrical uniform TLs was proposed by Ismo Lindell in 1992 [25].

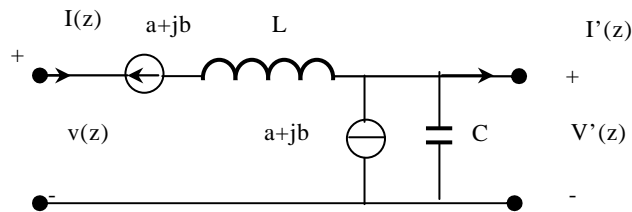


Figure 1.3 The equivalent circuit of a nonreciprocal TL

The equivalent circuit of a nonreciprocal TL is shown in Figure 1.3. Like the previous reciprocal TL, L is the distributed series inductance per unit length, C is the distributed capacitance per unit length, a and b are 2 new parameters of TL (similar to L and C), a is due to chirality, b is due to non-reciprocity. A voltage-controlled voltage source and a current-controlled current source are added to the equivalent circuit of conventional reciprocal TL.

The impedances and admittances of this TL can be written as:

$$Z = j\omega L \quad (1.22)$$

$$Z' = j\omega(a - jb) \quad (1.23)$$

$$Y = j\omega C \quad (1.24)$$

$$Y' = j\omega(a + jb) \quad (1.25)$$

The 2 new parameters a and b of TL can be written as:

$$a = k_r \sqrt{LC} \quad (1.26)$$

$$b = \chi_r \sqrt{LC} \quad (1.27)$$

where k_r is the relative chirality parameter, which corresponds to non-reciprocity on transmission in circuit theory, χ_r is the relative Tellegen parameter, which corresponds to non reciprocity in electromagnetic theory. the parameter b can also be presented in terms of an angle θ :

$$b = \sin \theta \sqrt{LC} \quad (1.28)$$

The voltage and current relationships between 2 ports are:

$$V'(z) = -j\omega(a - jb)V(z) - j\omega LI(z) \quad (1.29)$$

$$I'(z) = -j\omega CV(z) - j\omega(a + jb)I(z) \quad (1.30)$$

Solve the engine value problem of the above wave equations, we get:

$$\omega(a - jb)V + \omega LI = \mathcal{V} \quad (1.31)$$

$$\omega CV + \omega(a + jb)I = \mathcal{I} \quad (1.32)$$

Travelling wave solutions to wave equations of $V(z)$ and $I(z)$

$$V(z) = V_0^+ e^{-\gamma^+ z} + V_0^- e^{\gamma^- z} \quad (1.33)$$

$$I(z) = I_0^+ e^{-\gamma^+ z} + I_0^- e^{\gamma^- z} \quad (1.34)$$

where

$$\gamma^+ = \omega \sqrt{LC - b^2} + \omega a = \gamma_0 \left(\sqrt{1 - \chi_r^2} + k_r \right) = \gamma_0 (\cos \theta + k_r) \quad (1.35)$$

$$\gamma^- = \omega \sqrt{LC - b^2} - \omega a = \gamma_0 \left(\sqrt{1 - \chi_r^2} - k_r \right) = \gamma_0 (\cos \theta - k_r) \quad (1.36)$$

$$\gamma_0 = \omega \sqrt{LC} \quad (1.37)$$

The characteristic impedances

$$Z^+ = \frac{\gamma^+ - \omega(a + jb)}{\omega C} = \frac{\omega L}{\gamma^+ - \omega(a - jb)} \quad (1.38)$$

$$Z^- = \frac{\gamma^- + \omega(a + jb)}{\omega C} = \frac{\omega L}{\gamma^- + \omega(a - jb)} \quad (1.39)$$

The above formulas can also be written:

$$Z^+ = \sqrt{\frac{L}{C} - \frac{b^2}{C^2}} - j\frac{b}{c} = Z_c e^{-j\theta} \quad (1.40)$$

$$Z^- = \sqrt{\frac{L}{C} - \frac{b^2}{C^2}} + j\frac{b}{c} = Z_c e^{+j\theta} \quad (1.41)$$

$$Z_c = \frac{1}{Y_c} = \sqrt{\frac{L}{C}} \quad (1.42)$$

The characteristic admittances:

$$Y^+ = Y_c e^{+j\theta} \quad (1.43)$$

$$Y^- = Y_c e^{-j\theta} \quad (1.44)$$

It is indicated that, the propagation constant γ^\pm depend on the parameter a (k_r), the impedance Z^\pm and admittance Y^\pm depend on the parameter b (χ_r).

1.2.3 Transmission line network analysis

1.2.3.1 Impedance and admittance matrices

The impedance matrix $[Z]$ and admittance matrix $[Y]$ are defined by the terminal/port voltages and currents of networks [1-3], as shown in Figure 1.4. The 2 ports in the figure can be any TL mode.

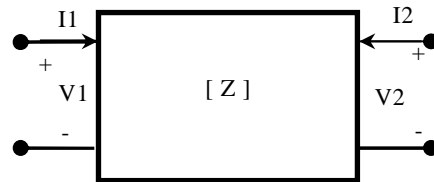


Figure 1.4 2-port network

The relationships of voltages and currents of the network between port 1 and port 2:

$$V_1 = Z_{11}I_1 + Z_{12}I_2 \quad (1.45)$$

$$V_2 = Z_{21}I_1 + Z_{22}I_2 \quad (1.46)$$

Its matrix form

$$\begin{bmatrix} V_1 \\ V_2 \end{bmatrix} = \begin{bmatrix} Z_{11} & Z_{12} \\ Z_{21} & Z_{22} \end{bmatrix} \begin{bmatrix} I_1 \\ I_2 \end{bmatrix} \quad (1.47)$$

Similarly, the admittance matrix $[Y]$ can be obtained:

$$I_1 = Y_{11}V_1 + Y_{12}V_2 \quad (1.48)$$

$$I_2 = Y_{21}V_1 + Y_{22}V_2 \quad (1.49)$$

Its matrix form

$$\begin{bmatrix} I_1 \\ I_2 \end{bmatrix} = \begin{bmatrix} Y_{11} & Y_{12} \\ Y_{21} & Y_{22} \end{bmatrix} \begin{bmatrix} V_1 \\ V_2 \end{bmatrix} \quad (1.50)$$

From the above equations, we can see that both [Z] matrix and [Y] matrix relate the port voltages and currents, and are the inverses of each other

$$[Z] = [Y]^{-1} \quad (1.51)$$

The impedance parameters can be obtained as:

$$Z_{11} = \left. \frac{V_1}{I_1} \right|_{I_2=0}, \text{ looking in input impedance of port 1, when port 2 open ended}$$

$$Z_{12} = \left. \frac{V_1}{I_2} \right|_{I_1=0}, \text{ transfer impedance between port 1 to port 2, when port 1 open ended}$$

$$Z_{21} = \left. \frac{V_2}{I_1} \right|_{I_2=0}, \text{ transfer impedance between port 2 to port 1, when port 2 open ended}$$

$$Z_{22} = \left. \frac{V_2}{I_2} \right|_{I_1=0}, \text{ looking in input impedance of port 2, when port 1 open ended}$$

Similarly, we can find the admittance parameters as:

$$Y_{11} = \left. \frac{I_1}{V_1} \right|_{V_2=0}, \text{ looking in input admittance of port 1, when port 2 short ended}$$

$$Y_{12} = \left. \frac{I_1}{V_2} \right|_{V_1=0}, \text{ transfer admittance between port 1 to port 2, when port 1 short ended}$$

$$Y_{21} = \left. \frac{I_2}{V_1} \right|_{V_2=0}, \text{ transfer admittance between port 2 to port 1, when port 2 short ended}$$

$$Y_{22} = \left. \frac{I_2}{V_2} \right|_{V_1=0}, \text{ looking in input admittance of port 2, when port 1 short ended}$$

If the network is lossless, the [Z] parameters and [Y] parameters are purely imaginary, if the network is lossy, The [Z] parameters and [Y] parameters are complex.

If the network is reciprocal, The [Z] parameters and [Y] parameters are symmetric,

$$Z_{ij} = Z_{ji}, \quad Y_{ij} = Y_{ji} \quad (1.52)$$

The nonreciprocal network is shown in Figure 1.5.

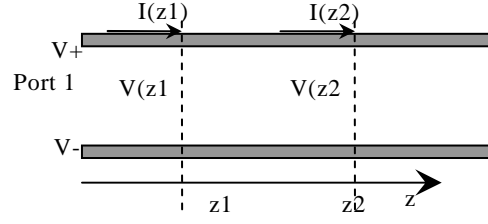


Figure 1.5 The nonreciprocal network

At point $z1$ of network

$$V(z1) = V^+ e^{-j\gamma^+ z1} + V^- e^{j\gamma^- z1} \quad (1.53)$$

$$I(z1) = Y^+ V^+ e^{-j\gamma^+ z1} - Y^- V^- e^{j\gamma^- z1} \quad (1.54)$$

At point $z2$ of network

$$V(z2) = V^+ e^{-j\gamma^+ z2} + V^- e^{j\gamma^- z2} \quad (1.55)$$

$$I(z2) = Y^+ V^+ e^{-j\gamma^+ z2} - Y^- V^- e^{j\gamma^- z2} \quad (1.56)$$

where

$$\gamma^+ = \omega\sqrt{LC - b^2} + \alpha a = \gamma_0 \left(\sqrt{1 - \chi_r^2} + k_r \right) = \lambda_0 (\cos \theta + k_r) \quad (1.57)$$

$$\gamma^- = \omega\sqrt{LC - b^2} - \alpha a = \gamma_0 \left(\sqrt{1 - \chi_r^2} - k_r \right) = \lambda_0 (\cos \theta - k_r) \quad (1.58)$$

$$\gamma_0 = \omega\sqrt{LC} \quad (1.59)$$

Assume $z2 > z1$, the impedance matrix is found

$$\begin{pmatrix} V(z1) \\ V(z2) \end{pmatrix} = \begin{pmatrix} Z11 & Z12 \\ Z21 & Z22 \end{pmatrix} \begin{pmatrix} I(z1) \\ I(z2) \end{pmatrix} \quad (1.60)$$

where

$$Z11 = -jZ_c \frac{\cos(\gamma_0 t \cos \theta - \theta)}{\sin(\gamma_0 t \cos \theta)} \quad (1.61)$$

$$Z12 = -jZ_c \frac{\cos \theta e^{jkr \gamma_0 t}}{\sin(\gamma_0 t \cos \theta)} \quad (1.62)$$

$$Z21 = -jZ_c \frac{\cos \theta e^{-jkr \gamma_0 t}}{\sin(\gamma_0 t \cos \theta)} \quad (1.63)$$

$$Z22 = -jZ_c \frac{\cos(\gamma_0 t \cos \theta + \theta)}{\sin(\gamma_0 t \cos \theta)} \quad (1.64)$$

$$Z_c = \frac{1}{Y_c} = \sqrt{\frac{L}{C}} \quad (1.65)$$

$$t = z2 - z1 \quad (1.66)$$

Lossless nonreciprocal network,

$$Z11^* = -Z11 \quad (1.67)$$

$$Z22^* = -Z22 \quad (1.68)$$

$$Z_{12}^* = -Z_{21} \quad (1.69)$$

$$Z_{21}^* = -Z_{12} \quad (1.70)$$

$$[Z] = Zc^2 \quad (1.71)$$

The non-symmetry of network

$$Z_{11} \neq Z_{22} \quad (1.72)$$

The non-reciprocity of network

$$Z_{12} \neq Z_{21} \quad (1.73)$$

1.2.3.2 The transmission matrix (ABCD)

The ABCD parameters are defined by the terminal/port voltages and currents of networks [1-3], as shown in Figure 1.6; it's quite convenient to obtain the ABCD matrix of cascaded networks.

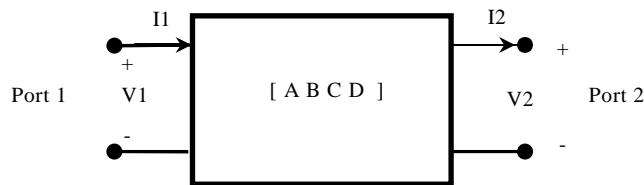


Figure 1.6 2-port network with ABCD matrix

The relations of voltages and currents between port 1 and port 2:

$$V_1 = A V_2 + B I_2 \quad (1.74)$$

$$I_1 = C V_2 + D I_2 \quad (1.75)$$

Its matrix form

$$\begin{bmatrix} V_1 \\ I_1 \end{bmatrix} = \begin{bmatrix} A & B \\ C & D \end{bmatrix} \begin{bmatrix} V_2 \\ I_2 \end{bmatrix} \quad (1.76)$$

For a cascade network shown in Figure 1.7

$$\begin{bmatrix} V_1 \\ I_1 \end{bmatrix} = \begin{bmatrix} A_1 & B_1 \\ C_1 & D_1 \end{bmatrix} \begin{bmatrix} V_2 \\ I_2 \end{bmatrix} = \begin{bmatrix} A_1 & B_1 \\ C_1 & D_1 \end{bmatrix} \begin{bmatrix} A_2 & B_2 \\ C_2 & D_2 \end{bmatrix} \begin{bmatrix} V_3 \\ I_3 \end{bmatrix} \quad (1.77)$$

It is found that the overall [ABCD] matrix of a cascaded network can be easily evaluated by multiplying the ABCD matrix of each individual network:

$$[ABCD]_n = \begin{bmatrix} A_1 & B_1 \\ C_1 & D_1 \end{bmatrix} \begin{bmatrix} A_2 & B_2 \\ C_2 & D_2 \end{bmatrix} \dots \begin{bmatrix} A_n & B_n \\ C_n & D_n \end{bmatrix} \quad (1.78)$$

where N is the number of cascaded network.

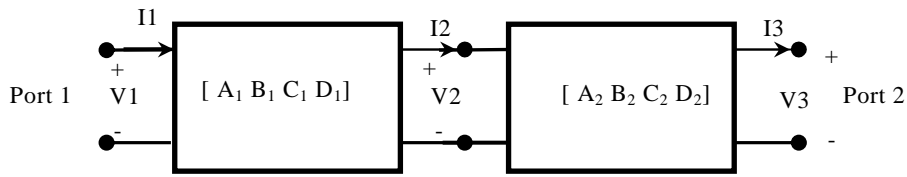


Figure 1.7 2-port cascade network

The ABCD parameters can be found as:

$A = \left. \frac{V_1}{V_2} \right|_{I_2=0}$, the voltage ratio of port 1 and port2, when port 2 is open ended.

$B = \left. \frac{V_1}{I_2} \right|_{V_2=0}$, the transferring impedance from port 1 to port2, when port 2 is short ended.

$C = \left. \frac{I_1}{V_2} \right|_{I_2=0}$, the transferring admittance from port 2 to port 1, when port 2 is open ended.

$D = \left. \frac{I_1}{I_2} \right|_{V_2=0}$, the current ratio of port 1 and port 2, when port 2 is short ended.

The relationships between ABCD parameters and impedance parameters

$$\begin{bmatrix} A & B \\ C & D \end{bmatrix} = \frac{1}{Z_{21}} \begin{bmatrix} Z_{11} & Z_{11}Z_{22} - Z_{12}Z_{21} \\ 1 & Z_{22} \end{bmatrix} \quad (1.79)$$

Network	[ABCD]
	$\begin{bmatrix} 1 & Z \\ 0 & 1 \end{bmatrix}$
	$\begin{bmatrix} 1 & 0 \\ Y & 1 \end{bmatrix}$
	$\begin{bmatrix} \cos \gamma l & jZ \sin \gamma l \\ jY \sin \gamma l & \cos \gamma l \end{bmatrix}$
	$\begin{bmatrix} (Y_2 + Y_3)/Y_3 & 1/Y_3 \\ (Y_1 Y_2 + Y_1 Y_3 + Y_2 Y_3)/Y_3 & (Y_1 + Y_3)/Y_3 \end{bmatrix}$

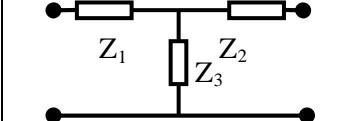
	$\begin{bmatrix} (Z_1 + Z_3)/Z_3 & (Z_1Z_2 + Z_1Z_3 + Z_2Z_3)/Z_3 \\ 1/Z_3 & (Z_2 + Z_3)/Z_3 \end{bmatrix}$
---	---

Table 1.1 The ABCD parameters of some 2-port network

1.2.3.3 Scattering parameters and transfer parameters

A) Scattering parameters

Scattering parameters (S parameters) are the most frequently used in RF engineering, for their derivation is based on forward and backward-travelling waves. The S parameters are defined by incident waves and reflected waves on TL networks [9]. A 2-port network is shown in Figure 1.8, the voltage waves on the terminals are used to define the S parameters of the network.

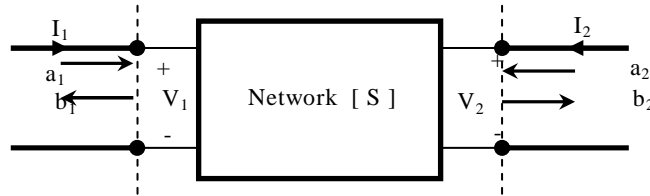


Figure 1.8 S parameters of 2-port network

Assume that the voltages and currents stimulated in ports, as shown in the figure. According to the TL theory, the port voltages and currents can be decomposed into backward travelling and forward travelling waves propagating on the transmission connected to the network:

$$V_1 = V_1^+ + V_1^- \quad (1.80)$$

$$I_1 = \frac{1}{Z_c} (V_1^+ - V_1^-) \quad (1.81)$$

$$V_2 = V_2^+ + V_2^- \quad (1.82)$$

$$I_2 = \frac{1}{Z_c} (V_2^+ - V_2^-) \quad (1.83)$$

where Z_c is the characteristic impedance of the TL connected to the network.

The forward and backward travelling voltage waves can be determined by the solutions of the above equations:

$$V_1^+ = \frac{V_1 + Z_c I_1}{2} \quad (1.84)$$

$$V_1^- = \frac{V_1 - Z_C I_1}{2} \quad (1.85)$$

$$V_2^+ = \frac{V_2 + Z_C I_2}{2} \quad (1.86)$$

$$V_2^- = \frac{V_2 - Z_C I_2}{2} \quad (1.87)$$

The incident and reflected voltages on 2 ports of the network are normalized by the characteristic impedance Z_C .

$$a_1 = \frac{V_1^+}{\sqrt{Z_C}} \quad (1.88)$$

$$a_2 = \frac{V_2^+}{\sqrt{Z_C}} \quad (1.89)$$

$$b_1 = \frac{V_1^-}{\sqrt{Z_C}} \quad (1.90)$$

$$b_2 = \frac{V_2^-}{\sqrt{Z_C}} \quad (1.91)$$

The normalized voltages and currents of the 2 ports

$$u_1 = \frac{V_1^+ + V_1^-}{\sqrt{Z_C}} = a_1 + b_1 \quad (1.92)$$

$$i_1 = \frac{(V_1^+ - V_1^-)}{\sqrt{Z_C}} = a_1 - b_1 \quad (1.93)$$

$$u_2 = \frac{V_2^+ + V_2^-}{\sqrt{Z_C}} = a_2 + b_2 \quad (1.94)$$

$$i_2 = \frac{(V_2^+ - V_2^-)}{\sqrt{Z_C}} = a_2 - b_2 \quad (1.95)$$

The incident and reflected powers can be describe by incident and reflected waves:

$$P_1^+ = \frac{1}{2} |a_1|^2 \quad (1.96)$$

$$P_1^- = \frac{1}{2} |b_1|^2 \quad (1.97)$$

$$P_2^+ = \frac{1}{2} |a_2|^2 \quad (1.98)$$

$$P_2^- = \frac{1}{2} |b_2|^2 \quad (1.99)$$

The S parameters can be defined as the following form:

$$b_1 = S_{11} a_1 + S_{12} a_2 \quad (1.100)$$

$$b_2 = S_{21} a_1 + S_{22} a_2 \quad (1.101)$$

The matrix form of the above equations

$$\begin{bmatrix} b_1 \\ b_2 \end{bmatrix} = \begin{bmatrix} S_{11} & S_{12} \\ S_{21} & S_{22} \end{bmatrix} \begin{bmatrix} a_1 \\ a_2 \end{bmatrix} \quad (1.102)$$

The physical significance of S parameters:

$S_{11} = \left. \frac{b_1}{a_1} \right|_{a_2=0}$, represents the reflectance of port 1, when port 2 well matched,

$S_{21} = \left. \frac{b_2}{a_1} \right|_{a_2=0}$, represents the transmission coefficient from port 1 to port 2, when port 2 well matched,

$S_{12} = \left. \frac{b_1}{a_2} \right|_{a_1=0}$, represents the transmission coefficient from port 2 to port 1, when port 1 well matched ,

$S_{22} = \left. \frac{b_2}{a_2} \right|_{a_1=0}$, represents the reflectance of port 2, when port 1 well matched.

The relationships between S parameters and transmission parameters ABCD:

$$S_{11} = \frac{A + B - C - D}{A + B + C + D} \quad (1.103)$$

$$S_{12} = \frac{2(AD - BC)}{A + B + C + D} \quad (1.104)$$

$$S_{21} = \frac{2}{A + B + C + D} \quad (1.105)$$

$$S_{22} = \frac{-A + B - C + D}{A + B + C + D} \quad (1.106)$$

B) Transfer parameters

One disadvantage of the S parameters is that it's difficult to get the S parameters of cascade networks, while it's quite convenient to obtain the transfer matrix [T] of cascaded networks [9]. The overall T parameters of cascade networks can be obtained by multiplying the T parameters of each individual network.

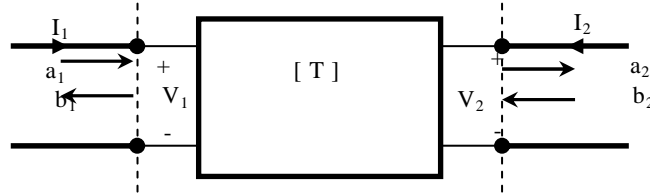


Figure 1.9 Transfer parameters of 2-port network

The T parameters can be defined

$$\begin{bmatrix} a_1 \\ b_1 \end{bmatrix} = \begin{bmatrix} T_{11} & T_{12} \\ T_{21} & T_{22} \end{bmatrix} \begin{bmatrix} a_2 \\ b_2 \end{bmatrix} \quad (1.107)$$

The T parameters of a cascade n network are

$$[T]_n = \begin{bmatrix} T_{11} & T_{12} \\ T_{21} & T_{22} \end{bmatrix} \begin{bmatrix} T_{22} & T_{23} \\ T_{32} & T_{33} \end{bmatrix} \dots \begin{bmatrix} T_{n,n} & T_{n,n+1} \\ T_{n+1,n} & T_{n,n} \end{bmatrix} \quad (1.108)$$

The relationships between T parameters and S parameters are

$$\begin{bmatrix} T_{11} & T_{12} \\ T_{21} & T_{22} \end{bmatrix} = \begin{bmatrix} \frac{1}{S_{21}} & -\frac{S_{22}}{S_{21}} \\ \frac{S_{11}}{S_{21}} & \frac{S_{12}S_{21} - S_{11}S_{22}}{S_{21}} \end{bmatrix} \quad (1.109)$$

$$\begin{bmatrix} S_{11} & S_{12} \\ S_{21} & S_{22} \end{bmatrix} = \begin{bmatrix} \frac{T_{21}}{T_{11}} & -\frac{T_{12}T_{21} - T_{11}T_{22}}{S_{21}} \\ \frac{1}{T_{11}} & -\frac{T_{12}}{T_{11}} \end{bmatrix} \quad (1.110)$$

For getting the S parameters of a 2 port cascade networks, the S parameters of each individual network can be converted to T parameters. Then, the overall T parameters of the cascade networks can be find easily. Finally, the S parameters can be evaluated by the overall T parameters.

1.3 Coplanar waveguide

Coplanar waveguide (CPW) was first demonstrated by C.P.Wen [6] in 1969, since then it was widely used in microwave and millimetre wave integrated components [7,15]. The CPW is a type of planar TL, which fabricated on a dielectric substrate. A conventional CPW consists of centre strip conductor and 2 ground planes on dielectric substrate is shown in Figure 1.10.

The CPW supports a quasi-TEM mode of propagation; it offers several attractive features, such as uniplanar construction, easy integration, simple fabrication, low dispersion, size reduction without limit and radiation loss reduction. A ground plane exists between any two adjacent lines, hence it has a week cross talk effects between adjacent lines. The characteristic impedance is determined by the ratio of $W/(W+2G)$, so the size reduction is possible without

limit, the only disadvantage being higher losses. The circuits using CPWs can be produced denser than microstrip circuits, which make CPW ideally suited for microwave and millimeter wave integrated components applications.

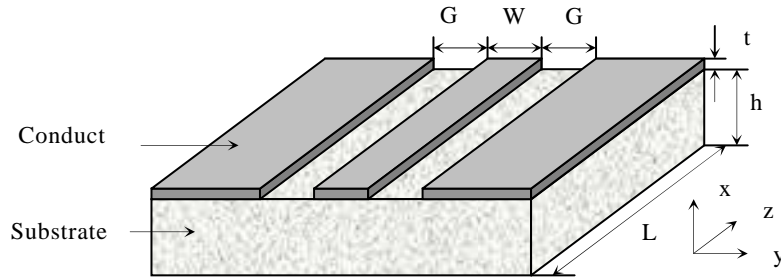


Figure 1.10 Conventional CPW on dielectric substrate: W-center conductor width, G-slot width, h-substrate height, t-conductor thickness, L-physical length.

The CPWs can be usually classified as conventional CPW and conductor backed CPW. For the conventional CPW, the ground planes are extended semi-infinitely on either side. However, in a practical conventional CPW the ground planes are extended finitely. For the conductor-backed CPW, a ground plane is added at the bottom surface of the substrate. A conductor backed CPW is shown in Figure 1.12.

1.3.1 Conventional CPW

For the conventional CPWs, the closed-form expressions of the effective dielectric constant and characteristic impedance with zero conductor thickness can be derived by using conformal-mapping methods [7], which are shown below

$$\epsilon_{eff} = 1 + \frac{\epsilon_r - 1}{2} \cdot \frac{K(k')}{K(k)} \cdot \frac{K(k_1)}{K(k_1')} \quad (1.111)$$

$$Z_0 = \frac{30\pi}{\sqrt{\epsilon_{eff}}} \cdot \frac{K(k')}{K(k)} \quad (1.112)$$

K represents the complete integral of the first kind, its values can be obtained by an integral or tabulated table. The corresponding $K(k)/K(k')$ values can be calculated by equations giving below:

$$\frac{K(k)}{K(k')} = \begin{cases} \frac{\pi}{\ln\left(\frac{2(1+\sqrt{k'})}{1-\sqrt{k'}}\right)}, & 0 \leq k \leq 0.707 \\ \frac{\ln\left(\frac{2(1+\sqrt{k'})}{1-\sqrt{k'}}\right)}{\pi}, & 0.707 \leq k \leq 1 \end{cases} \quad (1.113)$$

1.3.1.1 CPW has infinite-width ground planes

$$k = W / (W + 2G) \quad (1.114)$$

$$k' = \sqrt{1 - k^2} \quad (1.115)$$

$$k_1 = \frac{\sinh(\pi W / 4h)}{\sinh(\pi(W + 2G) / 4h)} \quad (1.116)$$

$$k_1' = \sqrt{1 - k_1^2} \quad (1.117)$$

1.3.1.2 CPW has finite-width ground planes (width S)

$$k = \frac{W}{(W + 2G)} \sqrt{\frac{1 - (W + 2G)^2 / (W + 2G + 2S)^2}{1 - W^2 / (W + 2G + 2S)^2}} \quad (1.118)$$

$$k' = \sqrt{1 - k^2} \quad (1.119)$$

$$k_1' = \sqrt{1 - k_1^2} \quad (1.120)$$

$$k_1 = \frac{\sinh(\pi W / 4h)}{\sinh(\pi(W + 2G) / 4h)} \cdot \sqrt{\frac{1 - \sinh^2(\pi(W + 2G) / 4h) / \sinh^2(\pi(W + 2G + 2S) / 4h)}{1 - \sinh^2(\pi W / 4h) / \sinh^2(\pi(W + 2G + 2S) / 4h)}} \quad (1.121)$$

1.3.1.3 Consideration of conductor thickness t

When the conductor thickness t is considered, the effective width of center conductor increases and the effective slot width decrease. The corresponding effective dielectric constant and characteristic impedance can be derived by formulas given below:

$$\epsilon_{eff}(t) = \epsilon_{eff} - \frac{0.7(\epsilon_{eff} - 1) \frac{t}{G}}{\frac{K(k')}{K(k)} + 0.7 \frac{t}{G}} \quad (1.122)$$

$$Z_0 = \frac{30\pi}{\sqrt{\epsilon_{eff}(t)}} \cdot \frac{K(k_e')}{K(k_e)} \quad (1.123)$$

where

$$k_e = \frac{S_e}{W_e + 2G_e} \quad (1.124)$$

$$k_e' = \sqrt{1 - k_e^2} \quad (1.125)$$

$$W_e = W + \Delta \quad (1.126)$$

$$G_e = G - \Delta \quad (1.127)$$

$$\Delta = \frac{1.25t}{\pi} \left[1 + \ln \left(\frac{8\pi a}{t} \right) \right] \quad (1.128)$$

1.3.1.4 Attenuation constant

The conductor attenuation constant and the dielectric attenuation constant for the conventional CPW with conductor thickness t can be evaluated from:

$$\alpha_c = \frac{4.88 \times 10^4}{\pi} R_s \epsilon_{eff} Z_0 P \frac{W+G}{G^2} \times \left\{ \frac{\frac{1.25t}{\pi} \ln \left(\frac{4\pi W}{t} \right) + 1 + \frac{1.25t}{\pi W}}{\left[2 + \frac{W}{G} - \frac{1.25t}{\pi G} \left(1 + \ln \frac{4\pi W}{t} \right) \right]^2} \right\} \text{ (dB/m)} \quad (1.129)$$

where

$$P = \begin{cases} \frac{k}{(1-k')(k')^{3/2}} \left[\frac{K(k)}{K(k')} \right]^2, & 0 \leq k \leq 0.707 \\ \frac{1}{(1-k)\sqrt{k}}, & 0.707 \leq k \leq 1 \end{cases} \quad (1.130)$$

$R_s = \sqrt{\omega \mu_0 / 2\delta}$ is the surface resistivity of the conductor
 δ is the conductivity

$$\alpha_d = \frac{27.3 \epsilon_r (\epsilon_{eff} - 1) \tan \delta}{\sqrt{\epsilon_{eff}} (\epsilon_r - 1) \lambda_0} \text{ (dB/m)} \quad (1.131)$$

λ_0 is the free space wave length

These equations are valid for

$$t \ll W, \quad h \ll G$$

For a conventional CPW with thin dielectric, the radiation lose is [8]

$$\alpha_r = \frac{\pi}{Q_r \lambda_g} \quad (1.132)$$

λ_g is the guided wave length,

$$\lambda_g = \frac{c}{f \sqrt{\epsilon_{eff}}} = \frac{\lambda_0}{\sqrt{\epsilon_{eff}}} \quad (1.133)$$

$$Q_r = \frac{K(k)K(k')}{\psi(\epsilon_r, h, k_0, G) \psi_{sc} \psi_{oc}} \quad (1.134)$$

$$\psi(\epsilon_r, h, k_0, G) = \frac{(\epsilon_r - 1) \left[1 + \frac{(\epsilon_r - 1)^2 (k_0 h)^2}{2} \right] \cdot (k_0 h) (k_0 b)^2 \left[1 + \frac{(\epsilon_r - 1)^2 (k_0 h)^2}{4} \right]}{\sqrt{\epsilon_{eff}} \left[1 + (\epsilon_r - 1)^2 (k_0 h)^2 \right]} \quad (1.135)$$

$$\psi_{sc} = \frac{5\pi}{8} \frac{1 + (1 - \frac{\pi^2}{8}) [1 + \frac{(\epsilon_r - 1)^2 (k_0 h)^2}{4}]}{3\epsilon_{eff}} \cdot \frac{1 + \frac{(\epsilon_r - 1)^2 (k_0 h)^2}{4}}{\epsilon_{eff}} \quad (1.136)$$

$$\psi_{oc} = \frac{\pi}{8} \frac{3 + (1 - \frac{\pi^2}{8}) [1 + \frac{(\epsilon_r - 1)^2 (k_0 h)^2}{4}]}{\epsilon_{eff}} \quad (1.137)$$

1.3.2 Conductor backed CPWs

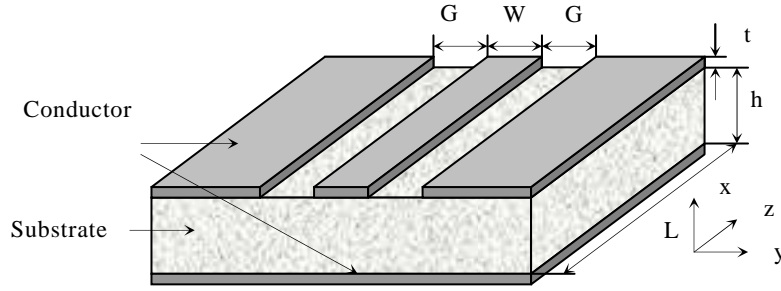


Figure 1.11 Conductor backed CPW on dielectric substrate: W -center conductor width, G -slot width, h -substrate height, t -conductor thickness, L -physical length.

For the conductor backed CPWs, the effective dielectric constant and characteristic impedance can be derived from equations given below

$$\epsilon_{eff} = \frac{1 + \epsilon_r \cdot \frac{K(k')}{K(k)} \cdot \frac{K(k_1)}{K(k_1')}}{1 + \frac{K(k')}{K(k)} \cdot \frac{K(k_1)}{K(k_1')}} \quad (1.138)$$

$$Z_0 = \frac{60\pi}{\sqrt{\epsilon_{eff}}} \cdot \frac{1}{\frac{K(k)}{K(k')} + \frac{K(k_1)}{K(k_1')}}} \quad (1.139)$$

where

$$k = W / (W + 2G) \quad (1.140)$$

$$k' = \sqrt{1 - k^2} \quad (1.141)$$

$$k_1 = \frac{\tanh(\pi W / 4h)}{\tanh(\pi(W + 2G) / 4h)} \quad (1.142)$$

$$k_1' = \sqrt{1 - k_1^2} \quad (1.143)$$

1.4 Magnetic materials

In a 4th century BC book “the Devil Valley Master (鬼谷子)”, magnetic materials have been described as: “The lodestone makes iron come or it attracts it” [30]. In 380 BC, Plato wrote “stone which Euripides calls a magnet”. The stones mentioned above are actually magnetite (Fe_3O_4) [2]. One of four great inventions of ancient China-Compass was also produced by magnetic materials. In 1600, Gilbert published the scientific studies text *De Magnete*. In 1820, Oersted found the quantitative measurements of magnetic materials: an electric current could create a magnetic field. In 1846, Faraday studied systematically the attraction and repulsion of magnetic materials: diamagnetic which are repelled by an increased flux density, paramagnetic which are attracted.

The ferromagnetic which has a strong magnetic force is added to form the three basic classes of magnetic response. The magnetic response to an applied magnetic field \vec{H} (amperes/m-SI units) attributes to the magnetic properties of materials. The microscopic response of material is given by magnetization \vec{M} . The magnetic induction \vec{B} (Tesla or Wb/m^2 -SI units) is the sum of \vec{H} and \vec{M} .

In a vacuum,

$$\vec{M} = 0$$

$$\vec{B} = \mu_0 \vec{H}$$

$$\mu_0 = 4\pi \times 10^{-7} \text{ H / m}^2$$

In the past, cgs units were widely used by scientists working in magnetic materials. In cgs units, \vec{B} unit is in gauss, \vec{H} in oersteds, and \vec{M} in emu/cm³.

The constitutive relation in cgs units is

$$\vec{B} = \vec{H} + 4\pi\vec{M}$$

The conversion between cgs and SI units

$$1 \text{ A / m} = 4\pi 10^{-3} \text{ Oe} \quad \text{Magnetic field } \vec{H}$$

$$1 \text{ A / m} = 10^{-3} \text{ emu / cm}^3 \quad \text{Magnetization } \vec{M}$$

$$1 \text{ T} = 10^4 \text{ G} \quad \text{Induction } \vec{B}$$

The magnetic response of all materials is mainly due to the magnetic moment of individual electrons, which directly connected to the spin. The basic families of magnetic materials have a highly linear response

$$\vec{M} = \chi \vec{H},$$

where χ is the magnetic susceptibility.

Diamagnetism : $\chi < 0$.

Paramagnetism : $\chi > 0$ changes with applied field

Ferromagnetism : large positive χ changes with applied field

Antiferromagnetism : small positive χ

Ferrimagnetism: χ

The properties of these types of magnetic materials will be introduced in this chapter.

1.4.1 Diamagnetism

The induced moment of diamagnetism is opposite to the applied field \vec{H} , the diamagnetism materials are repulsive with applied field. The magnetic susceptibility χ is negative; it's temperature independent and normally small. χ can be given by the Langevin theory [31]

$$\chi = -\mu_0 N Z e^2 / 6m \langle r^2 \rangle$$

where N is the number of atoms per unit volume, Z is the number of electrons of each atom, e is the charge of an electron, m is the mass of an electron, $\langle r^2 \rangle$ is the mean square distance of the electrons from the nucleus [29].

The magnetic susceptibility of several materials is shown in Table 1.2.

Material	χ
Vacuum	0
Water	$-1.2e^{-5}$
Carbon (graphite)	$-1.6e^{-5}$
Carbon (diamond)	$-2.1e^{-5}$
Copper	$-1.0e^{-5}$
Bi	$-16.6e^{-5}$
Silver	$-2.6e^{-5}$
Superconductors	$-10e^5$

Table 1.2 the magnetic susceptibility of materials

1.4.2 Paramagnetism

The induced moment of paramagnetic material is in the same direction of the applied field \vec{H} . the properties of this material is case by some unpaired electrons and the realignment of the electron paths due to the external magnetic field.

The magnetic susceptibility χ of paramagnetism is small and positive.

$$\chi = Nm^2 / 3k_B T$$

where N is the density of dipoles, which aligned by applied field,

m is the moment of each dipole,

k_B is the Boltzmann constant,

T is the absolute temperature.

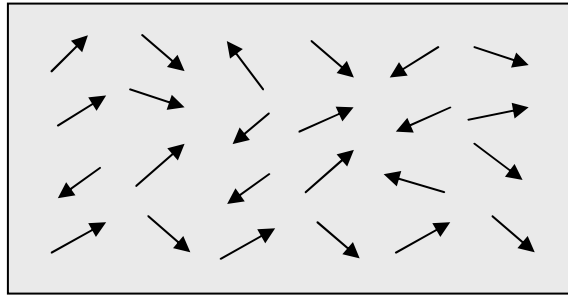


Figure 1.12 Paramagnetism

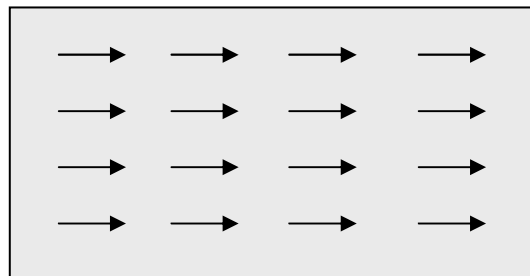
Material	χ
Sodium	$0.72 e^{-5}$
Magnesium	$1.2e^{-5}$
Lithium	$1.4e^{-5}$
Aluminium	$2.2e^{-5}$
Cesium	$5.1e^{-5}$
Tungsten	$6.8e^{-5}$

Table 1.3 The magnetic susceptibility of materials

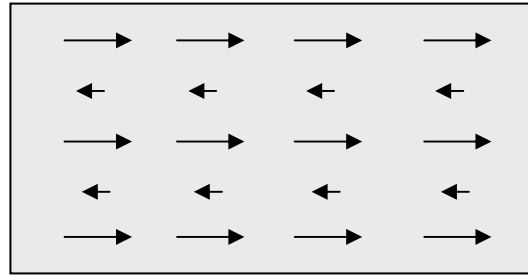
1.4.3 Ferromagnetism and Ferrimagnetism

In ferromagnetism, the magnetic moments of electrons couple together, the all magnetic moments of material can point in the same direction, giving a very strong magnetic effect. The properties of ferromagnetic materials are characterized by the Curie temperature T_c , the saturation magnetization M_s , the coercive field H_c , and the magnetic anisotropy energy K .

In ferrimagnetism, the opposing magnetic moments of electrons are unequal, a spontaneous magnetization exists. The all magnetic moments of material don't point in the same direction, giving a strong magnetic effect (weaker than ferromagnetism).



(a)



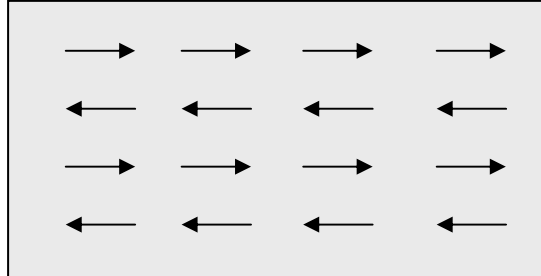
(b)

Figure 1.13 (a) Ferromagnetism and (b) Ferrimagnetism

Material	Curie temperature (K)
Fe	1043
Co	1388
Ni	627
Fe ₂ O ₃	948
FeOFe ₂ O ₃	858
NiFe ₂ O ₄	858
Y ₃ Fe ₅ O ₁₂	553
BaFe ₁₂ O ₁₉	723

Table 1.4 The magnetic susceptibility of materials

1.4.4 Antiferromagnetism

**Figure 1.14** Antiferromagnetism

In ferromagnetism, the magnetic moments of electrons point in opposite directions of electrons align in a regular pattern with neighbouring spins, giving a smaller magnetic effect than ferromagnetism.

1.4.5 Ferrites

Ferrites are ferrimagnetic oxides made of oxygen anions around metal divalent or trivalent cations [26], the attractive property of ferrite can be adjusted by changing its composition. For example, if a divalent iron cation is replaced by a divalent composition, a mixed ferrite with completely different properties can

be obtained. The substitution of a trivalent iron cation also makes a ferrite whose property can be adjusted. Ferrite materials are highly resistive; the electromagnetic wave can penetrate and interact with the ferrites. The ferrite resistivity varies between 10 and 10e8 ohms/cm. The relative dielectric permittivity of ferrite is almost constant at microwave frequencies. Dielectric losses result from both trivalent and divalent iron cations. The relative permeability governs the interaction between the wave and the ferrite. For improving the stability of ferrites, the ferrites should have a high Curie temperature and low magnetostriction constant. To have a low loss, the ferrite should have a low coercivity. To get a high saturation magnetization, an intense magnetic field is needed to saturate the ferrites, which leads to a high gyro-magnetic anisotropy. The properties of ferrites will be discussed in Chapter 3.

1.5 Metamaterials

1.5.1 Definition of metamaterials

Metamaterial was firstly defined by Rodger M. Walser in 1999 as “Macroscopic composites having a synthetic, three-dimensional, periodic cellular architecture designed to produce an optimized combination, not available in nature, of two or more responses to specific excitation” [27,28,32]. In the book of Caloz C., Itoh T., [17], the MTM is defined as artificial effectively homogeneous electromagnetic structures with unusual properties not readily available in nature. Actually, MTM is a macroscopic composite of periodic or non-periodic structure, whose function is determined by both the cellular architecture and the chemical composition [16].

In the past 10 years, MTMs, left-handed materials (LHM) [33-38], negative-refractive index materials (NIM) [39-49], double negative materials [50-53], backward-wave materials [54], Veselago medium, and negative phase velocity medium [55-57] have been regarded as the same terms. It should be noted that, they actually represent different meanings. According to the previous definition, LHM is a MTM, however, MTM has much broader range than LHM [16].

The MTM is regarded as an effective medium; the structural average cell size should be smaller than a quarter of guided wavelength λ_g [16,17]. The MTM properties are characterized by the constitutive parameters: the electric permittivity ε and the magnetic permeability μ . The refractive index n can be calculated by: $n = \sqrt{\varepsilon_r \mu_r}$, where ε_r and μ_r are the relative permittivity and permeability related to the free space permittivity and permeability, $\varepsilon_r = \varepsilon / \varepsilon_0 = \varepsilon / 8.854 \times 10^{-12}$, $\mu_r = \mu / \mu_0 = \mu / 4\pi \times 10^{-7}$.

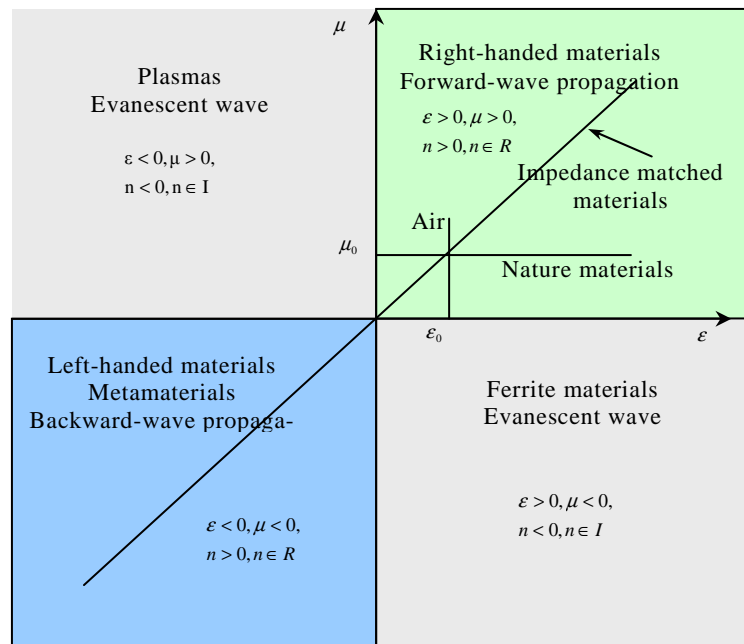


Figure 1.15 Permittivity (ϵ)-permeability (μ) and refractive index (n) diagram.
R-purely real, I-purely imaginary

Figure 1.15 illustrates all materials properties in the $\epsilon - \mu$ domain [16]. The first quadrant ($\epsilon > 0$ and $\mu > 0$) represents right-handed materials (RHM), which supports a forward propagating wave. In RHM, the electric field \vec{E} , the magnetic field \vec{H} , and the wave vector \vec{k} form a right-handed system. In nature, most materials have the permeability μ_0 and permittivity larger than ϵ_0 . The second quadrant ($\epsilon < 0$ and $\mu > 0$) is electric plasma, which supports evanescent waves. The third quadrant, with simultaneously negative permittivity and permeability ($\epsilon < 0$ and $\mu < 0$), denotes the left-handed materials (LHM), which supports a backward propagating waves. In LHM, the electric field E , the magnetic field H , and the wave vector k form a left-handed system, it has anti-parallel phase and group velocities. The fourth quadrant ($\epsilon > 0$ and $\mu < 0$) is magnetic plasma, which supports evanescent waves.

The point $\mu = -\mu_0$ and $\epsilon = -\epsilon_0$ represents the anti-air in LHM region, which produces a perfect lens; the point $\mu = 0$ and $\epsilon = 0$ represents the nihility, which yields a perfect tunnelling effect; the line $\mu = \epsilon$ in both RHM and LHM regions represents impedance-matching materials, which have perfect impedance matching with air. The vicinity of $\mu = 0$ is called as μ -near zero material, and the vicinity of $\epsilon = 0$ is called as ϵ -near zero material.

1.5.2 History of metamaterials

Metamaterials were first known as left-handed materials or negative-refractive index materials. The earliest negative refraction was assumed by Mandelshtam in Moscow University [58]. Then the theory of backwave-wave media was investigated by Malyuzhinets and Sivukhin in 1950s [60, 61]. The backward-wave structures were applied to design the microwave tubes in 1960s [62, 63, 64], and the negative refraction was also discovered in periodical media [65].

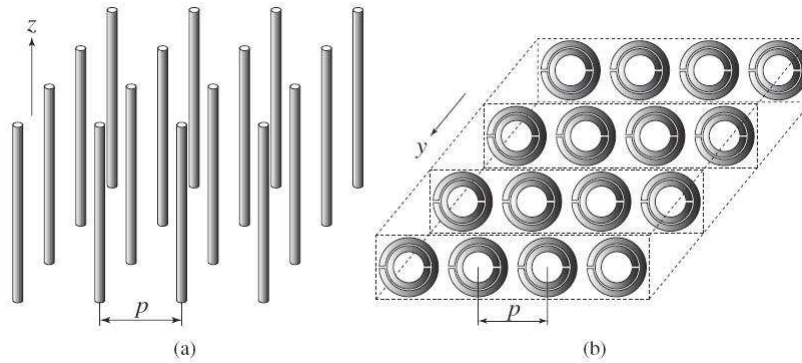


Figure 1.16 Metamaterial discovered by Pendry, (a) electric plasma with negatively permittivity, (b) magnetic plasma with negative permeability [17]

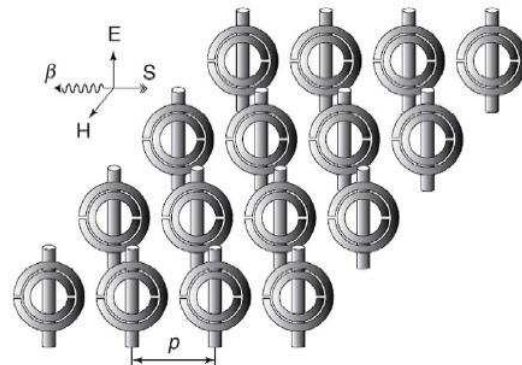


Figure 1.17 Metamaterial introduced by Smith based on SRRs and wires with negatively permittivity and negative permeability [17]

The left-handed materials were proposed by Veselago in 1968, who made a systematic analysis of electromagnetic behaviours in materials with negative permittivity and permeability, and named the term of LHM [66]. Besides the negative refraction and backward-wave propagation, Veselago also anticipated their unique electromagnetic features like reversed of Snell's Law, the Doppler effect and backward Cerenkov radiation. Veselago showed that the electric field, magnetic field, and wavevector of an electromagnetic wave in an LHM form a LH triad. LHMs support electromagnetic waves with antiparallel group and phase velocities, known as backward waves [67]. Consequently, while energy travels away from the source, wavefronts travel backward toward

the source, the phenomenon in LHM is associated with negative index of refraction. However, due to the non-existence in nature and lack of experimental verification, LHM did not occur until 30 years later by Pendry and Smith [68-70].

The artificially electric plasma using the wire medium with negative permittivity was first realized by Pendry in 1996 [68]. Then the artificially magnetic plasma with negative permeability was discovered by Pendry in 1999 [69], the split-ring resonators (SRR) are used to achieve the magnetic response. The first artificial LHM was obtained by Smith et al. in 2001 by combining the wires and SRRs [70], the negative refraction phenomenon was verified. The LHM based on the wires and SRRs is resonant structure, it has several drawbacks such as narrow bandwidth, high lossy, and highly dispersive.

For the engineering applications, in order to overcome the weaknesses of resonant approach based LH MTMs, the transmission-line (TL) approach of LHM was presented by three groups (Eleftheriades, Oliner, and Caloz-Itoh) in 2002 [38, 46, 71-74]. It is well known that a conventional TL is composed of distributed series inductance and shunt capacitance, which is equivalent to a one-dimensional right-handed material. As a dual model of the conventional TL, a new TL consists of series capacitance and shunt inductance supports backward waves and hence can represent LHM. The distributed components were used to realize the left-handed (LH) TL. A general composite right/left-handed (CRLH) TL model has been proposed to represent RHM and LHM [17]. Based on the CRLH structures, a lot of microwave components and antennas have been proposed [17]. The transmission-line approach will be discussed detailedly in Section 4.2.1.

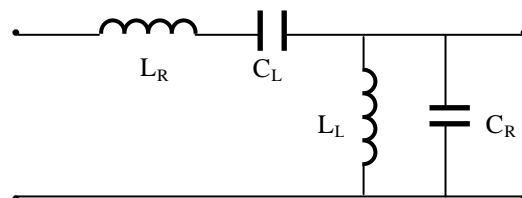


Figure 1.18 Equivalent circuit of the CRLH TL

The gradient refractive index medium which bends electromagnetic waves was realized in 2005 [75], and the optical transformation was proposed in 2006[76-77]; which can be used to make invisible cloaks, and to control the propagation of electromagnetic waves. From then on, MTM has a much broader meaning than LHM, which do not require the negative permeability and/or negative permittivity, and hence open a completely new area [16], which inspired the creation of new devices in the microwave and millimetre field.

1.5.3 Applications of metamaterials

The unique properties of MTMs have allowed novel components to be developed. The components that have been constructed are based directly on the relevant MTM concepts. For CRLH TL MTMs, novel microwave applications like guided wave application and radiated wave application can be realized by using the unique features of MTMs [17], they exhibit novel performance compared with similar classical devices.

1.5.3.1 Guided wave applications

For guided wave applications, the electromagnetic energy remains confined in the metal and dielectric media constituting the components [17]. The CRLH TLs can be used to replace the RH TLs of conventional branch-line couplers, several novel dual-band couplers were proposed by Caloz, Itoh et al. [17,78-79], as shown in Figure 1.19, these concepts can be applied to the microwave component like phase shifters, matching networks, baluns, etc. [80].

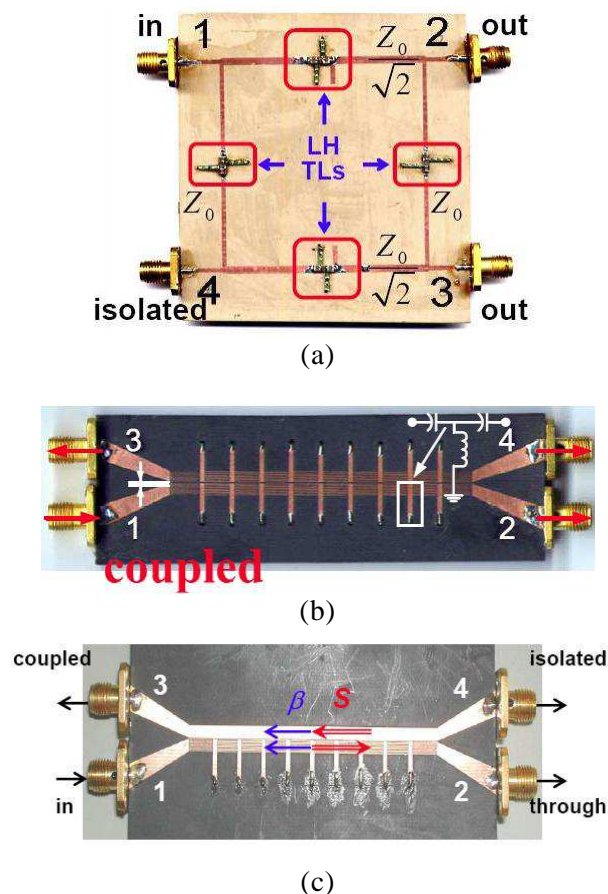


Figure 1.19 Novel CRLH couplers: (a) Dual-band branch line coupler [17], (b) Symmetric coupled-line coupler [78], (c) Asymmetric coupled-line coupler [79]

Another guided wave application of CRLH MTM is zeroth order resonator (ZOR); the unique property of a CRLH is that a β of zero can be obtained at a non-zero frequency [17], a prototype is shown in Figure 1.20. The ZOR has some novel characteristics, such as zeroth-order resonances, which is very interesting for dual band and size-independent resonators. Other applications have been developed include novel components for filters, true-time delay lines, modulators, and power dividers.

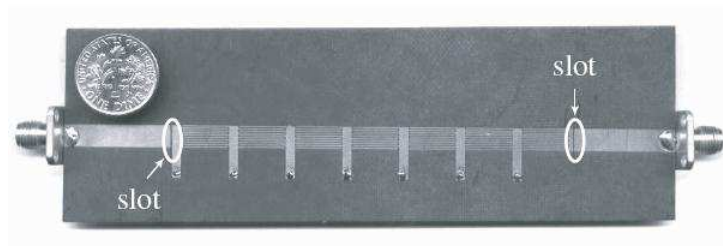


Figure 1.20 Prototype of 7-unit cell zeroth order resonator [17]

The physical working principles of these devices is mainly based on the engineering of the propagation constant β or the phase $\phi = -\beta \cdot d$.

1.5.3.2 Radiated wave application

When a MTM structure is open to free space and supports a leaky-wave mode, it radiates and works as an antenna. Due to the new propagation properties of CRLH structure, unique radiation effects can be obtained.

The CRLH leaky-wave antenna (LWA) was proposed by Liu and Grbic [81-83]. The LWA radiates by virtue of a propagating leaky wave supported by the guiding structure. One of the main problems of conventional periodic LWA is the open stopband that occurs when the beam is scanned to broadside. Such LWA suffer from serious beam degradation at broadside because of this stopband effect. The CRLH MTM is the first structure that overcomes the stopband problem and thus opens up a variety of new applications.

Another radiated wave application of CRLH MTM is ZOR antenna, the resonance is independent of physical length of ZOR, and the antenna's size is determined by the loadings of unit cells. One prototype of microstrip-based ZOR antenna consists of series interdigital capacitor and shunt meander line inductor is shown in Figure 1.22 .

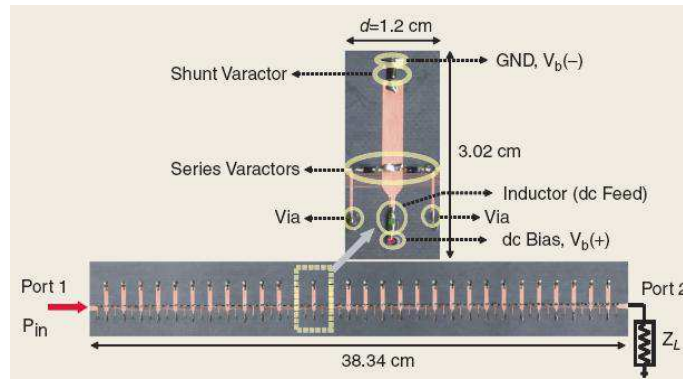


Figure 1.21 Prototype of 30-unit cell LWA [83]

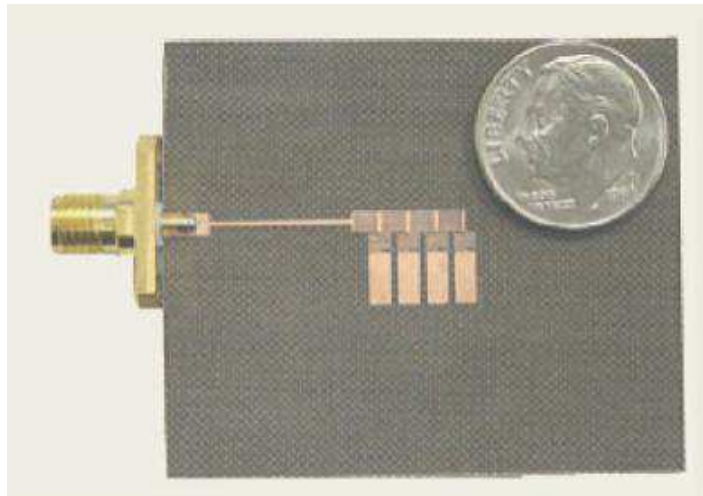


Figure 1.22 Prototype of 4-unit cell zeroth order resonator antenna

1.5.3.3 Other applications of interest

Other novel applications of CRLH MTM include novel planar antenna structures, bandwidth enhancement of small antennas, superlensing (DNG materials, impedance surfaces), and the squeezing and tunneling of guided waves. Other applications at optical frequencies include plasmonic effects such as plasmonic superlensing and the directive beaming of light and enhanced transmission through subwavelength apertures.

Note that the publications of CRLH MTM applications with anisotropy substrate (ferrite) are much less than applications with isotropic substrate (alumina, FR4, Teflon). Yet several microwave components with ferrite substrate were proposed by Abdalla and Tsutsumi [84-91]. They presented the nonreciprocal left-handed coplanar waveguide over ferrite substrate with only shunt inductive load [84], the left-handed coplanar waveguide coupler on ferrite substrate [85], the tunable left handed zeroth-order resonator on ferrite substrate [86], the tunable left handed ferrite transformer [87], the ferrite tunable meta-

material phase shifter [88], the left-handed characteristics of ferrite microstrip line magnetized to wave propagation [89], the nonreciprocal phase-shift composite right/left handed transmission lines and their application to leaky wave antennas [90], and the nonreciprocal left-handed transmission characteristics of microstriplines on ferrite substrate [91], which indicated CRLH MTMs with anisotropy substrate (ferrite) are also very interesting.

Also, some non linear active CRLH components like phase shifter and leaky-wave antenna were proposed by Caloz and Kong [92-98], the capacitors in aforementioned CRLH can be replaced by varactors with bias network. The varactor diodes were used as tunable elements like variable series and shunt capacitors, the capacitance of the varactor diodes can be controlled by the applied reverse voltage of bias network. Many novel properties can be obtained by the varactors, for example ultra-wideband, multi-band (dual/tri-band -controllable beam) operation, zeroth-order high efficiency, which is very importante in modern communication systems.

1.5.3.4 Example of the zeroth-order resonator

We decided to study an example and we simulated a zeroth-order resonator. The CRLH MTM supports an infinite-wavelength wave at a finite and non-zero frequency, the unbalanced CRLH TL has 2 frequencies where $\beta = 0$ [17, 86], a zeroth-order resonator (ZOR) using CRLH technology with infinite-wavelength wave is studied in this section. The layouts of the CRLH ZOR are shown in Figure 1.23 and Figure 1.24; the ZORs are composed of interdigital capacitors and shunt stub inductors embedded in the CPW. The centre conductor width W is 1.4 mm, gap width S 0.9 mm, shunt inductor width W_1 0.1mm, shunt inductor length L_1 2 mm, shunt inductor gap width S_1 0.65mm, CRLH ZOR unit length L is 3mm.

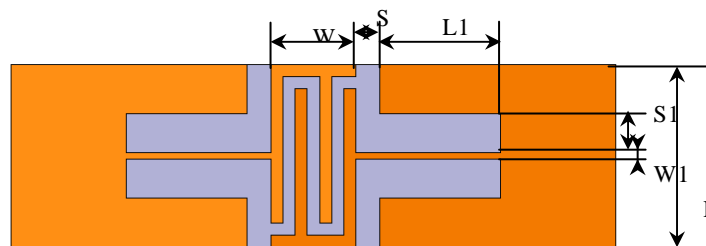


Figure 1.23 Unit cell of CRLH ZOR on CPW

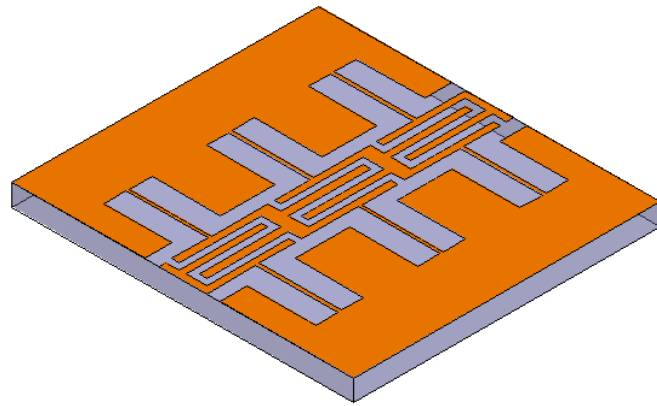


Figure 1.24 3-unit CRLH ZOR on CPW

S parameters

The full-wave simulation results of ZORs are carried out, the simulated S parameters of the 1-unit CRLH ZOR and the 3-unit CRLH ZOR are shown Figure 1.25 and Figure 1.26, it's indicated that, the 1-unit ZOR is a band pass structure at about 4.5 GHz, where S_{11} is about -23 dB and S_{21} is about -0.5 dB; the band pass frequency of the 3-unit ZOR is about 4.4 GHz, where S_{11} is about -14 dB and S_{21} is about -2 dB.

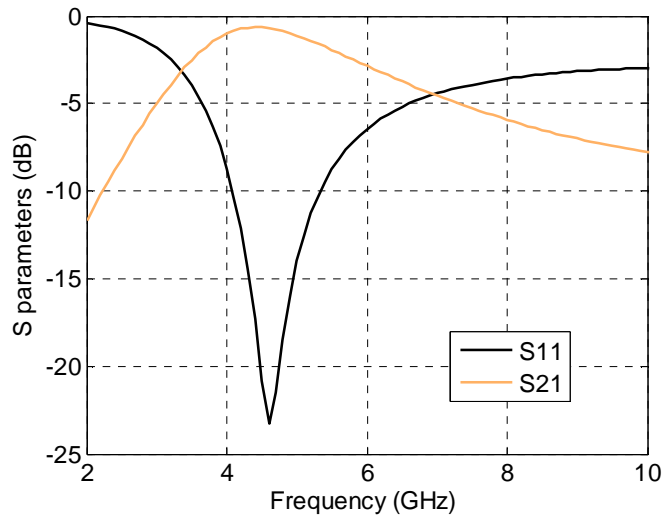


Figure 1.25 S parameter of 1-unit CRLH ZOR on CPW

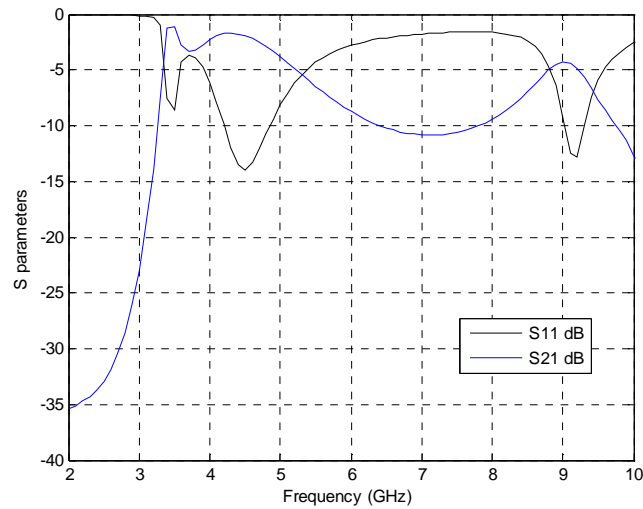


Figure 1.26 S parameter of 3-unit CRLH ZOR on CPW

Propagation constants

The calculated propagation constants from S parameters of the 1-unit CRLH ZOR and the 3-unit CRLH ZOR are shown Figure 1.27 and Figure 1.28. For the 2 ZORs, $\beta = 0$ at 5.5 GHz and 7.5 GHz, we get a left-hand frequency band from 3.1 GHz to 5.5 GHz, a right-hand frequency band from 7.5 GHz to 10 GHz, and a stopband from 5.5 GHz to 7.5 GHz.

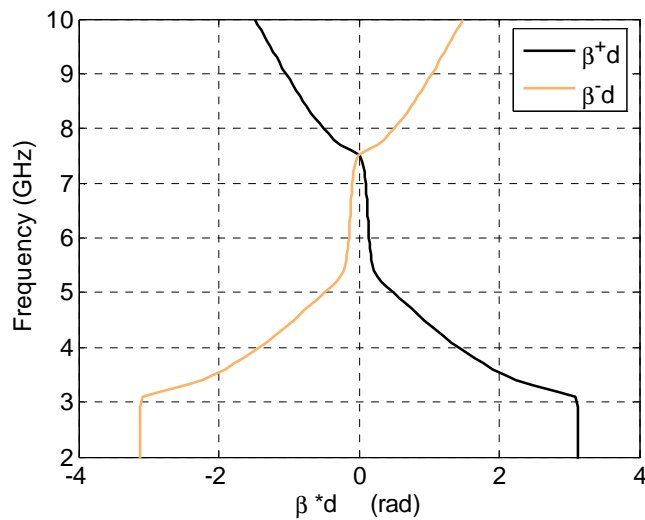


Figure 1.27 Propagation constants of 1-unit CRLH ZOR on CPW

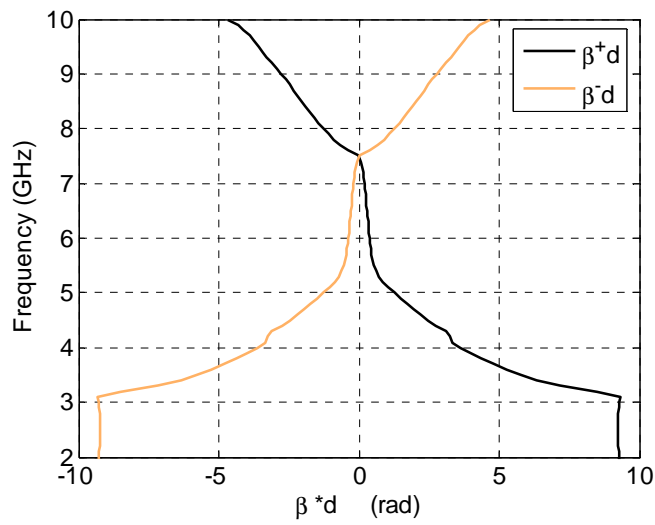


Figure 1.28 Propagation constants of 3-unit CRLH ZOR on CPW

Electric field distributions

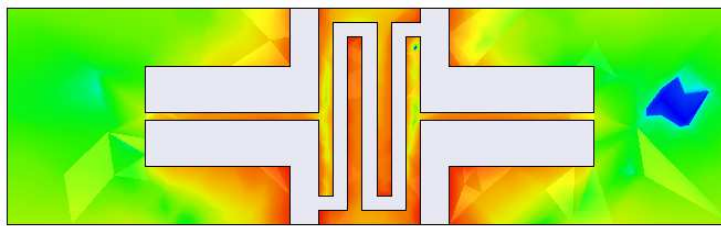


Figure 1.29 Electric field distributions of 1-unit CRLH ZOR at 5.5 GHz

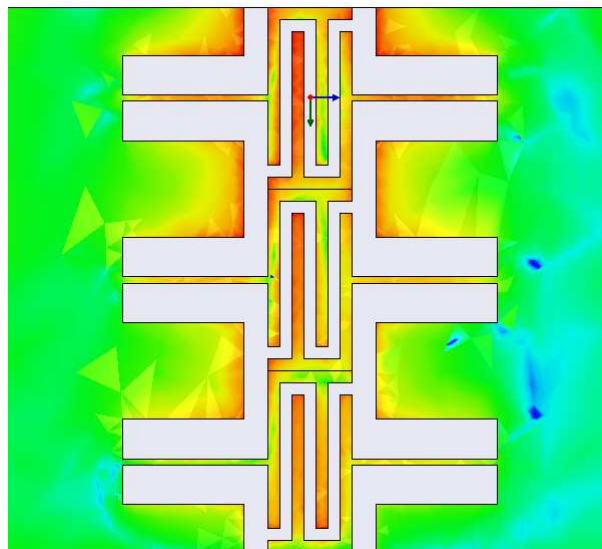


Figure 1.30 Electric field distributions of 3-unit CRLH ZOR at 5.5 GHz

The simulated electric field distributions of ZORs are shown in Figure 1.29 and Figure 1.30. The voltages at every node of the 2 structures are almost identical, which indicated that the structure has the infinite-wavelength.

1.6 Conclusions

The TL theory, CPW, magnetic materials and MTMs are introduced in this chapter. The properties of reciprocal TL, the non reciprocal TL, and the TL network analysis are studied in Section 1.2. The conventional CPW with infinite-width ground planes and with finite ground planes are presented in Section 1.3, the conductor backed CPW is also illustrated in this Section. The magnetic materials are introduced in Section 1.4. The definition, history and applications of metamaterials of MTM are presented in Section 1.5.

1.7 Bibliography

- [1] **DAVID M. P.** « Microwave engineering », third edition, John Wiley & Sons, 2004, 720 p.
- [2] **CHANG K.** « Encyclopedia of RF and microwave engineering », 6-volume set, 1 edition, Wiley-Interscience, 2005, 5832 p.
- [3] **ROBERT. E. Collin.** « Foundations for microwave engineering », second edition, Wiley-IEEE Press, 2000, 944 p.
- [4] **EOIN C., SVERRE L.** « Millimeter-wave integrated circuits », Boston, Springer, 2005, 288 p.
- [5] **ESKELINEN H., ESKELINEN P.** « Microwave component mechanics », Artech house, 2003, 392 p.
- [6] **Wen C.P.** Coplanar waveguide: A surface strip transmission line suitable for nonreciprocal gyromagnetic device applications. IEEE Trans. Microwave Theory Tech., 1969, vol. 17, No. 12, pp. 1087-1090.
- [7] **Rainne N. Simons.** « Coplanar waveguide circuits components and systems », John Wiley & Sons, 2001, 464 p.
- [8] **Brian C. Wadell.** « Transmission line design handbook », Artech house, 1991, 500 p.
- [9] **KINAYMAN N., AKSUN M.I.** « Modern microwave circuits », Artech house, 2005, 624 p.
- [10] **GUPTA K.C.** « Microstrip lines and slotlines », second edition, Artech house, 1996, 560 p.
- [11] **SHIH Y.C., ITOH T.** Analysis of conductor-backed coplanar waveguide, Electronics letters, Vol. 18, No. 12, 1993, pp. 538-540.
- [12] **ZHOU T., LE BERRE M., BENEVENT E., et al.** Coplanar waveguides with or without Barium Ferrite Thin Films,

- Microwave and optical technology letters, Vol. 52, No. 9, 2010, pp. 2007-2010.
- [13] **SPORKMANN T.** The evolution of coplanar MMICs over the past 30 Years, Microwave journal, Vol. 41, No. 7, 1998, pp. 96-111.
- [14] **GHINOE G., NALDI C.** Parameters of coplanar waveguides with lower ground plane, Electron. letters, Vol. 19, No. 18, 1983, pp. 734-735.
- [15] **NGUYEN C.** « Analysis methods for RF, microwave, millimeter-wave planar transmission line structures », John Wiley & Sons, 2000, 240 p.
- [16] **CUI T.J., DAVID S., LIU R.P.** « Metamaterials: theory, design and applications », Springer, 2009, 392 p.
- [17] **CALOZ C., ITOH T.** « Electromagnetic metamaterials: transmission line theory and microwave applications », Wiley-IEEE Press, 2005, 376 p.
- [18] **ELEFThERIADES G. V., BALMAIN K. G.** « Negative refraction metamaterials: fundamental principles and applications », Wiley-IEEE Press, 2005, 440 p.
- [19] **ENGHETA N., ZIOLKOWSKI R. W.** « Electromagnetic metamaterials: physics and engineering explorations », Wiley-IEEE Press, 2006, 440 p.
- [20] **MARQUES R., MARTIN F., SOROLLA M.** « Metamaterials with negative parameters: theory, design and microwave applications », Wiley-Interscience, 2008, 315 p.
- [21] **MUNK B. A.** « Metamaterials critique and alternatives », Wiley-Interscience, 2009, 189 p.
- [22] **ZOUHDI S., SIHVOLA A., VINOGRADOV A. P.** « Metamaterials and plasmonics: fundamentals, modelling, applications », Springer, 2008, 306 p.

- [23] **Tellegen B.D.II.** The grrator, a new network element, Philips res. rept., vol.3, 1948, pp.81-101.
- [24] **CHAMBERS L.G.** Propagation in a gyrational medium, Quart. Jour. mech. appl. math., Vol.9, no.3, 1956, pp. 360-370.
- [25] **LINDELL I. V., VALTONEN M. E., SIHVOLA A.H.** Theory of nonreciprocal and nonsymmetric uniform transmission lines, IEEE Trans. Microwave theory tech., vol.42, No. 2, 1994. pp. 291-297.
- [26] **WHITAKER J. C.** « The RF transmission systems handbook », CRC Press, 2002, 504 p.
- [27] **WEIGLHOFER W. S., LAKHTAKIA A.** « Introduction to complex mediums for optics and electromagnetics », SPIE Press, Bellingham, 2003, 776 p.
- [28] **ENGHETA N., ZIOLKOWSKI R. W.** « Metamaterials: physics and engineering aspects », John Wiley & Sons Inc, 2006, 440 p.
- [29] **KITTEL C.** « Introduction to solid state physics », 6th edition. John Wiley & Sons, 2004, 704 p.
- [30] Four Great Inventions. Available at :
<http://en.wikipedia.org/wiki/Four_Great_Inventions>
- [31] **KITTEL C.** « Introduction to Solid State Physics », sixth edition, John Wiley & Sons, 2004, 704 p.
- [32] Metamaterials: What are they? What are they good for?
<http://adsabs.harvard.edu/abs/2000APS..MAR.Z5001W>
- [33] **DAVID R. S., NORMAN K.** Negative refractive index in left-handed materials, Phys. rev. lett., Vol. 85, 2000, pp. 2933-2936.

- [34] **GARCIA N., NIETO-VESPERINAS M.** Left-handed materials do not make a perfect lens, *Phys. rev. lett.*, Vol. 88, No.20, 2002, 20743 [4 pages].
- [35] **CHEN H.S., RAN L.X., HUANGFU J.T., et al.** Left-handed materials composed of only S-shaped resonators, *Phys. rev. E*, Vol. 70, 2004, 057605 [4 pages].
- [36] **MARKOS P., SOUKOULIS C.** Numerical studies of left-handed materials and arrays of split ring resonators, *Phys. rev. E*, Vol. 65, 2002, 036622 [8 pages].
- [37] **CALOZ C., CHANG C.-C., ITOH T.** Full-wave verification of the fundamental properties of left-handed materials in waveguide configurations, *Journal of applied physics*, Vol. 90, No.11, 2001, pp. 5483-5486.
- [38] **CALOZ C., ITOH T.** Application of the transmission line theory of left-handed (LH) materials to the realization of a microstrip "LH line", *IEEE antennas and propagation society international symposium*, Vol. 2, 2002, pp. 412-415.
- [39] **VESELAGO V., BRAGINSKY L., SHKLOVER V., et al.** Negative refractive index materials, *Journal of computational and theoretical nanoscience*, Vol. 3, No. 2, 2006, pp. 189-218.
- [40] **SMITH D. R., PENDRY J. B., WILTSHIRE M. C. K.** Metamaterials and negative refractive index, *Science*, Vol. 305, No. 5685, 2004, pp. 788-792.
- [41] **RAMAKRISHNA S. A.** Physics of negative refractive index materials, *Reports on progress in physics*, Vol. 68, No. 2, 2005, pp.449-521.
- [42] **SHELBY R. A., SMITH D. R., SHULTZ S.** Experimental verification of a negative index of refraction, *Science*, Vol. 292, No. 5514, 2001, pp. 77-79.

- [43] **SOUKOULIS C. M., LINDEN S., WEGENER M.** Negative refractive index at optical wavelengths, *Science*, Vol. 315, No. 5808, 2007, pp. 47-49.
- [44] **SMITH D. R., SCHURIG D., ROSENBLUTH M., et al.** Limitations on subdiffraction imaging with a negative refractive index slab, *Appl. phys. lett.*, Vol. 82, 2003, pp.1506-1508.
- [45] **FOTEINOPOULOU S., ECONOMOU E. N., SOUKOULIS C. M.** Refraction in media with a negative refractive index, *Phys. rev. lett.*, Vol. 90, No. 10, 2003, 107402 [4 pages].
- [46] **ELEFThERIADES G.V., IYERA.K., KREMER P.C. EDWARD S., et al.** Planar negative refractive index media using periodically L-C loaded transmission lines. *IEEE Transactions on microwave theory and techniques*, Vol. 50, No. 12, 2002, pp. 2702-2712.
- [47] **PENDRY J. B.** Negative refraction makes a perfect lens, *Phys. rev. lett.*, Vol. 85, No. 18, 2000, pp. 3966-3969.
- [48] **LI J.S., ZHOU L., CHAN C. T., SHENG P.** Photonic band gap from a stack of positive and negative index materials, *Phys. rev. lett.*, Vol. 90, No. 8, 2003, 083901 [4 pages]
- [49] **SHADRIVOV I.V., SUKHORUKOV A.A., KIVSHAR Y.S.** Guided modes in negative-refractive-index waveguides, *Phys. rev. E.*, Vol. 67, No. 5, 2003, 057602 [4 pages].
- [50] **ZIOLKOWSKI R.W.** Design, fabrication, and testing of double negative metamaterials, *IEEE Transactions on antennas and propagation*, Vol.51, 2003, No.7, pp.1516-1529.
- [51] **ZIOLKOWSKI R.W., KIPPLE A.D.** Application of double negative materials to increase the power radiated by electrically small antennas, *IEEE transactions on antennas and propagation*, Vol 51, No. 10, 2003, pp.2626-2640.

- [52] **Holloway C.L., Kuester, E.F., Baker-Jarvis J., et al.** Double negative (DNG) composite medium composed of magnetodielectric spherical particles embedded in a matrix, IEEE Transactions on antennas and propagation, Vol. 51, No.10,2003, pp. 2596-2603.
- [53] **NADER E., ZIOLKOWSKI R.W.** A positive future for double-negative metamaterials, IEEE Transactions on microwave theory and techniques, Vol. 53, No. 4, 2005, pp. 1535-1556.
- [54] **JYLHAL L., KOLMAKOV I., MASLOVSKI S., TRETYAKOV S.** Modeling of isotropic backward-wave materials composed of resonant spheres, J. Appl. Phys., Vol 99, 2006, 043102 [7 pages].
- [55] **LAKHTAKIA A., MCCALL M. W., WEIGLHOFFER W. S.** Brief overview of recent developments on negative phase-velocity mediums (alias left-handed materials), AEU-International journal of electronics and communications, Vol. 56, No. 6, 2002, pp. 407-410.
- [56] **MACKAY TOM G., LAKHTAKIA A.** Plane waves with negative phase velocity in Faraday chiral mediums, Phys. Rev. E, Vol. 69, 2004, 026602 [9 pages].
- [57] **WEIGLHOFFER W.S., LAKHTAKIA A.** « Introduction to complex mediums for optics and electromagnetics », SPIE publications, 2003, 776 p.
- [58] **MANDLSHTAM L.** Group velocity in a crystal lattice, Zhurnal Eksperimentalnoii Teoreticheskoi Fiziki, Vol. 15, 1945, pp. 476-478.
- [60] **MALYUZHINETS G.D.** A note on the radiation principle. Zhurnal Technicheskoi Fiziki, Vol. 21, 1951, pp. 940-942.
- [61] **SIVUKHIN D.V.** The energy of electromagnetic waves in dispersive media, Opt. Spektrosk, Vol. 3, 1957, pp. 308-312.

- [62] **HUTTER R.G.E.** Beam and wave electronics in microwave tubes, Van Nostrand Reinhold, Princeton, 1960, pp. 220-230.
- [63] **ALTMAN J.L.** « Microwave circuits », Van Nostrand Reinhold, Princeton, 1964, 304 p.
- [64] **SILIN R.A. SAZONOV V.P.** Slow-wave structures, Moscow, Soviet Radio , 1966.
- [65] **SILIN, R.A.** Waveguiding properties of two-dimensional periodic slow-wave systems, Voprosy Radioelektroniki. Elektronika, Vol. 4, 1959, pp. 11-33.
- [66] **VESELAGO V.G.** The electrodynamics of substances with simultaneously negative values of ϵ and μ , Soviet Physics Uspekhi, Vol. 10,1968, pp. 509-514.
- [67] **BAENA J.D., MARQUES R., MEDINA F., et al.** Artificial magnetic metamaterial design by using spiral resonators, Phys. Rev. B, Vol. 69, 2004, 014402.
- [68] **PENDRY J.B., HOLDEN A.J., STEWART W.J., et al.** Extremely low frequency plasmons in metallic mesostructures, Phys. Rev. Lett., 1996, Vol. 76, pp 4773-4776.
- [69] **PENDRY J.B., HOLDEN A.J., ROBBINS D.J., et al.** Magnetism from conductors and enhanced nonlinear phenomena, IEEE Trans. Micro. Theory Tech., Vol. 47, 1999, pp. 2075-2084.
- [70] **SHELBY R.A., SMITH D.R., SCHULTZ S.** Experimental verification of a negative index of refraction, Science, Vol. 292, 2001, pp. 77-79.
- [71] **IYER A.K., ELEFTHERIADES G.V.** Negative refractive index metamaterials supporting 2-D waves, IEEE-MTT-S 2, 2002, pp. 412-415.

- [72] **OLINER A.A.** A periodic-structure negative-refractive-index medium without resonant elements, *IEEE-AP-S Digest*, 2002, p. 41.
- [73] **IYER A.K., KREMER P.C., ELEFThERIADES G.V.** Experimental and theoretical verification of focusing in a large, periodically loaded transmission line negative refractive index metamaterial, *Opt. Express*, Vol.11, No. 7, 2003, pp. 696-708.
- [74] **CALoz C., ITOH T.** Transmission line approach of left-handed (LH) structures and microstriprealization of a low-loss broadband LH filter, *IEEE Trans. Antennas Propagat.*, Vol. 52, 2004, pp. 1159-1166.
- [75] **SMITH D.R., MOCK J.J., STARR A.F., et al.** Gradient index metamaterials, *Phys. Rev. E*, Vol. 71, 2005, 036609.
- [76] **PENDRY J.B., SCHURIG D., SMITH D.R.** Controlling electromagnetic fields, *Science*, Vol. 312, 2006, pp. 1780-1782.
- [77] **LEONHARDT U.** Optical conformal mapping. *Science*, Vol. 312, 2006, pp. 1777-1780.
- [78] **CALoz C., ITOH T.** A novel mixed conventional microstrip and composite right/left-handed backward-wave directional coupler with broadband and tight coupling characteristics,” *IEEE Microwave Wireless Compon. Lett.*, Vol. 14, 2004, pp. 31-33.
- [79] **CALoz C., SANADA A., ITOH T.** A novel composite right/lefthanded coupled-line directional coupler with arbitrary coupling level and broad bandwidth, *IEEE Trans. Microwave Theory Tech.*, Vol. 52, 2004, pp. 980-992.
- [80] **LIN I., DEVINCENTIS M., CALoz C., et al.** Arbitrary dual-band components using composite right/left-handed transmission lines, *IEEE Trans. Microwave Theory Tech.*, Vol. 52, 2004, pp. 1142-1149.

- [81] **LIU L., CALOZ C., ITOH T.** Dominant mode leaky-wave antenna with backfire-to-endfire scanning capability, *Electron. Lett.*, Vol. 38, 2002, pp. 1414-1416.
- [82] **GRBIC A., ELEFThERIADES G. V.** A backward-wave antenna based on negative refractive index L-C networks, *Proc. IEEE Int. Symp. Antennas Propagation.*, Vol. 4. 2002, pp. 340-343.
- [83] **SUNGJOON L., CALOZ C., ITOH T.** Metamaterial-based electronically controlled transmission-line structure as a novel leaky-wave antenna with tunable radiation angle and beamwidth, *IEEE Transactions on Microwave Theory and Techniques*, Vol. 53, No. 1, 2005, pp. 161-173.
- [84] **ABDALLA M. A., HU Z.** Nonreciprocal left handed coplanar waveguide over ferrite substrate with only shunt inductive load, *Microwave and Optical Technology Letters*, Vol.49, No. 11, 2007, pp. 2810-2814.
- [85] **ABDALLA M. A., HU Z.** On the study of left-handed coplanar waveguide coupler on ferrite substrate, *Progress In Electromagnetics Research Letters*, Vol. 1, 2008, pp. 69-75.
- [86] **ABDALLA M. A., HU Z.** Design and Analysis of Tunable Left Handed Zeroth-Order Resonator on Ferrite Substrate, *IEEE Transactions on Magnetics*, Vol. 44, No.11, 2008, pp.3095-3098
- [87] **ABDALLA M. A., HU Z.** Compact Tunable Left Handed Ferrite Transformer, *Journal of Infrared, Millimeter and Terahertz Waves*, Vol. 30, No. 8, 2009, pp. 813-825.
- [88] **ABDALLA M. A., HU Z.** Ferrite tunable metamaterial phase shifter, *IEEE Antennas and Propagation Society International Symposium (APSURSI)*, 2010 No. 11-17, 2010, pp. 1-4
- [89] **TSUTSUMI M., OKUBO K.** Left-Handed Characteristics of Ferrite Microstrip Line Magnetized to Wave Propagation, *IEEE Transactions on Magnetics*, Vol. 45, No. 10, 2009, pp. 4207-4210.

- [90] **UEDA T., HORIKAWA K., AKIYAMA M., et al.** Non-reciprocal Phase-Shift Composite Right/Left Handed Transmission Lines and Their Application to Leaky Wave Antennas, *IEEE Transactions on Antennas and Propagation*, Vol. 57, No. 7, 2009, pp. 1995-2005.
- [91] **UEDA T., TSUTSUMI M.** Nonreciprocal left-handed transmission characteristics of microstriplines on ferrite substrate, *IET Microwaves, Antennas & Propagation*, Vol. 1, No. 2, 2007, pp. 349-354.
- [92] **CALOZ C., LIN I-H., ITOH T.** Characteristics and potential applications of nonlinear left-handed transmission lines, *Microwave and Optical Technology Letters*, Vol. 40, No. 6, 2004, pp. 471-473.
- [93] **LIM S., CALOZ C., ITOH T.** Electronically scanned composite right/left handed microstrip leaky-wave antenna, *IEEE Microwave and Wireless Components Letters*, Vol. 14, No.6, 2004, pp. 277-279.
- [94] **KIM H., KOZYREV A.B., KARBASSI A., et al.** Linear tunable phase shifter using a left-handed transmission line, *IEEE Microwave and Wireless Components Letters*, Vol. 15, No. 5, 2005, pp. 366-368.
- [95] **KUYLENSTIERNA D., VOROBIEV A., LINNER P., et al.** Composite right/left handed transmission line phase shifter using ferroelectric varactors, *IEEE Microwave and Wireless Components Letters*, Vol. 16, No. 4, 2006, pp. 167-169.
- [96] **CHEN H., WU B-I., RAN L. X., et al.** Controllable left-handed metamaterial and its application to a steerable antenna, *Applied Physics Letters*, Vol. 89, No. 5, 2006, pp. 053509-053509-3.
- [97] **WANG D., RAN L., CHEN H., et al.** Active left-handed material collaborated with microwave varactors, *Applied Physics Letters*, Vol. 91, No. 16, pp. 164101-164101-3.

- [98] **CALOZ C., ITOH T., RENNINGS A.** CRLH metamaterial leaky-wave and resonant antennas, *IEEE Antennas and Propagation Magazine*, Vol. 50, No. 5, 2008, pp. 25–39.

2 Conventional coplanar components on alumina

2.1 Introduction

As a coplanar transmission line, coplanar waveguide (CPW) offers several attractive features, such as uniplanar construction, easy integration, simple fabrication, low dispersion, size reduction without limit and radiation loss reduction [1-4], it is very widely used in microwave and millimetre wave components [5-6]. In our work, interdigital capacitors [7-13], gap capacitors [7-8], and shunt inductors [8, 14-17], will be integrated in CPW to build composite right/left-handed transmission lines, or to make other microwave and millimetre components. It is really necessary to study first the properties of CPW components: in particular the equivalent circuit, the S parameters, the propagation constant. For series capacitors and shunt inductors, we show in the coming sections how to extract their values.

2.2 Fabrication of coplanar components on alumina

The CPW components are processed using standard lift-off and the metal evaporation techniques.

2.2.1 Photolithography

The photolithography technique is used in the fabrication of CPW components. It's used to selectively remove parts of conductor on the substrate. UV light is used to transfer the geometric pattern of CPW from a mask made out of chromium and glass to a light-sensitive photoresist (TI 35 ES) deposited on the substrate. The photoresist which is a negative photoresist (the exposed parts of the resist remain after exposition and development) is then developed with chemical (AZ 726 MIF) to engrave pattern into photoresist on substrate. The metal is deposited on the photoresist. During the lift-off, the resist is removed in acetone, and the pattern is transferred to the metal layer. The processes are shown in Figure 2.1.

Here are the photolithography technique parameters:

Coating with photoresist TI 35 ES: thickness 2.5 μm

Pre-bake: temperature 110 °C and time 2 minutes

Insulation for exposing pattern with mask: 20 seconds (140mJ/cm²)

Rest 10 minutes

Reverse bake: temperature 130°C and time 2 minutes.

Flood insulation (without mask): 55 seconds (385 mJ/cm^2)
 Development with chemical AZ 726 MIF: 30 seconds
 Lift-off using acetone to remove the resist

2.2.2 Vacuum deposition / evaporation

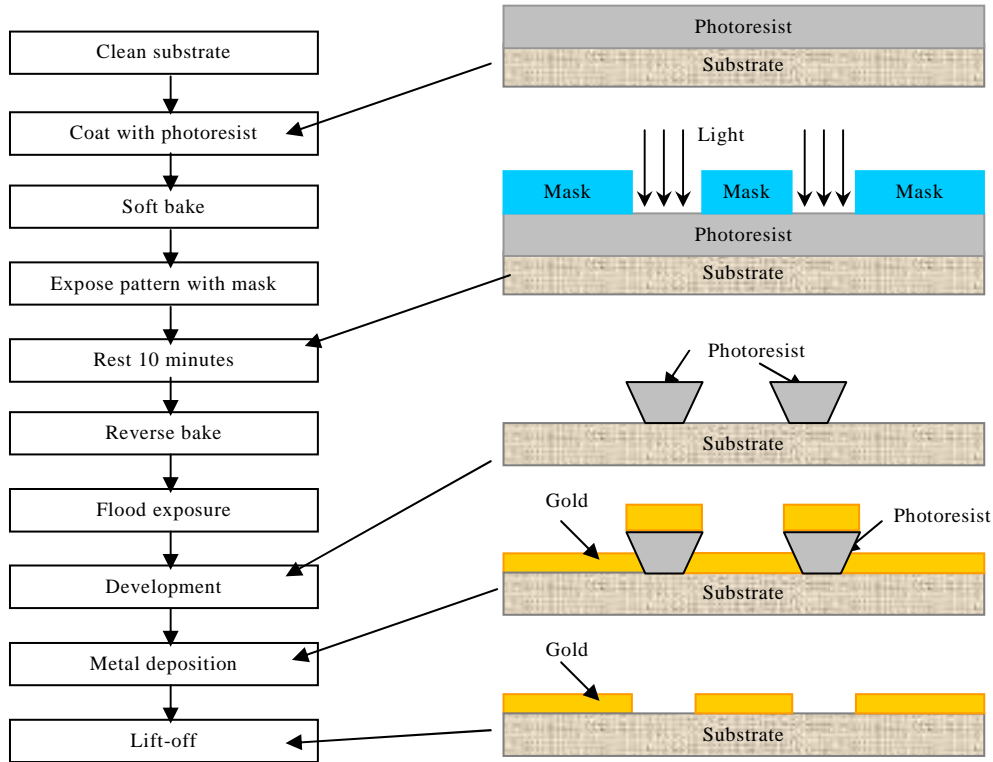


Figure 2.1 Process of photolithography

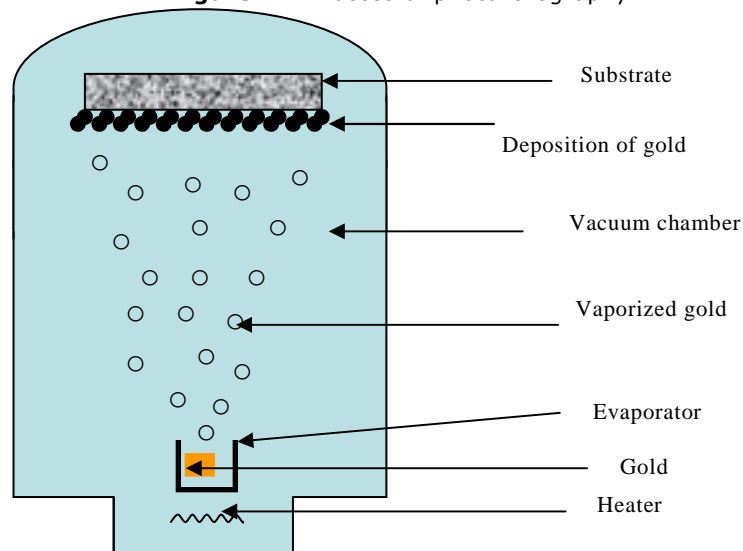


Figure 2.2 Vacuum deposition / evaporation

The evaporation processes is used to deposit a thin metal film on the substrate. In our case, gold is evaporated in a vacuum; it travels directly to the target substrate. The evaporation set-up is shown in Figure 2.2.

The thickness of gold layer reaches at the highest $1\ \mu\text{m}$ to $1.5\ \mu\text{m}$ (less than the thickness of photoresist which reaches $2.5\ \mu\text{m}$). There is approximately a factor 3 between the thickness of resist and that of the deposited metal layer.

In NANOLYON [18], we can fabricate a sample with dimension as small as $5\ \mu\text{m}$. The top-views of some prototypes are show in Figure 2.3. The pictures were took by a microscope ZEISS in the clean room of NANOLYON.

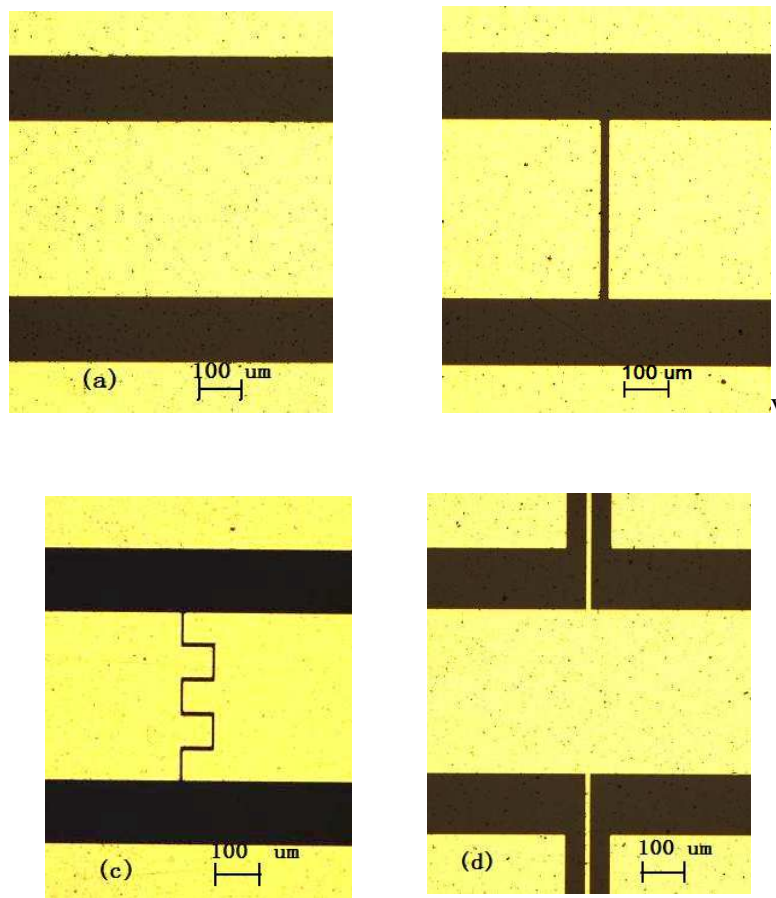


Figure 2.3 Top-view of CPW components: (a) CPW, (b) gap capacitor (gap of $20\ \mu\text{m}$), (c) interdigital capacitor (gap of $10\ \mu\text{m}$), (d) shunt inductor (width of $10\ \mu\text{m}$)

2.3 Simulation and modelling

2.3.1 Finite element simulation

Simulations were performed with the software COMSOL Multiphysics, which is an engineering, design, and finite element analysis software environment for the modeling and simulation of microwave components [19]. In the framework of this PhD thesis, this software is used for the first time at INL to simulate such high frequency transmission lines and devices. The steps in the simulation process are shown below:

- Defining the geometry

The defined geometry of a CPW in COMSOL is shown in Figure 2.4; the dimensions of the CPW should be defined in this step. The CPW has a symmetry plane perpendicular to the x axis and it's a magnetic symmetric structure. For saving simulation time, we just need to draw a half of CPW, the plane of symmetry / mirror plane is defined as a perfect magnetic conductor (PMC), the corresponding characteristic impedance of the lumped ports is set to 100Ω .

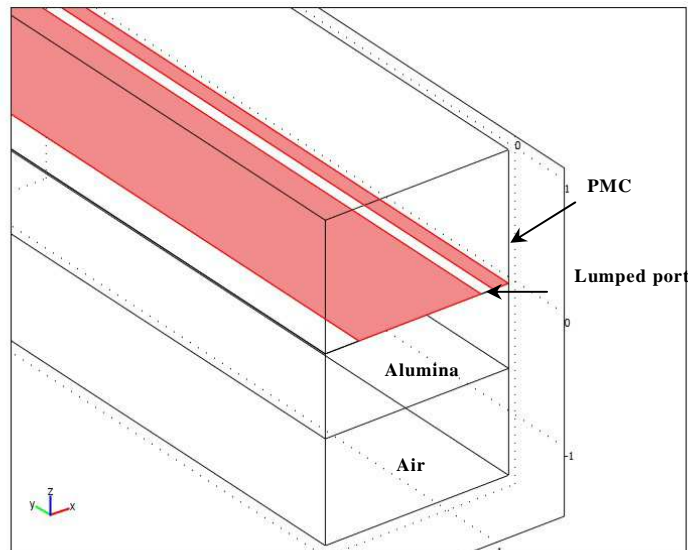


Figure 2.4 Geometry of CPW in COMSOL

- Meshing

The well meshed CPW in COMSOL is shown in Figure 2.5. For the 'Free mesh parameters – Global', we chose 'Coarser' as 'Predefined mesh sizes'. To get a precise mesh sizes, we can also chose 'Normal / Fine / Finer'.....which leads to much smaller mesh sizes, and much higher number of degree of freedom (DOF). For the 'Free mesh parameters – Boundary', we chose 'Triangle' as 'Boundary mesh parameters – Method'. Then we mesh the transverse section / surfaces of CPW.

After the transverse surfaces of the CPW have being meshed, we do ‘Swept mesh parameters’. We chose ‘Coarser’ as ‘Predefined mesh sizes’; define the ‘Number of element layers’ as 5; define the ‘Sweep direction’, we select the meshed transverse surfaces as ‘source faces’, the un-meshed transverse surfaces at the other end of CPW as ‘target faces’. The longest sample we modelled was 1 cm long.

Notice that, for a computer with 4x3.0 GHz core with 8 GB memories, the maximum DOF that the computer can deal with is about 200000 - 300000, for a computer with 8x2.33 GHz core (E5345) and 16 GB memories, the maximum number of DOF that the computer can deal with is about 300000 – 500000. So, every time we mesh, we have to check the number of DOF, otherwise, the simulation may abort if memory is lacking.

To reduce the number of DOF, we use several methods to reduce the number of DOF: the length of CPW which connected to the inter-digital capacitor and the gap capacitors is decreased to 100 μm , the length of CPW connected to the shunt capacitor is defined as 500 μm .

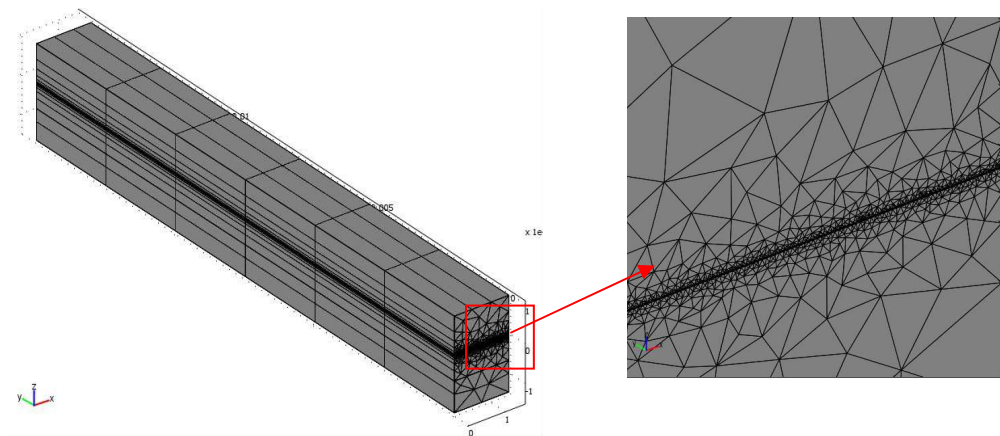


Figure 2.5 Meshed CPW in COMSOL and zoom in

- *Specifying the physics*

At this step, the subdomain settings and boundary settings are defined. We define the subdomain air / alumina (epsilon 9.8) / conductor (gold / copper), we define the outer boundaries as ‘matched boundary’; the inner boundaries as ‘continuity’; the plane of symmetry / mirror plane as perfect magnetic conductor (PMC); the 2 ports as ‘lumped port’ with ‘external cable impedance’ 100 Ω . Each time, only 1 of the 2 lumped ports can be defined as ‘voltage generator at this port’). For saving simulation time, the perfect electric conductor (PEC) can usually be used to replace the conductor layer (The PEC has no thickness whereas the conductor has a thickness, and thus more mesh sizes).

- Solving

The solver parameters are defined in this step. We chose the ‘Harmonic propagation’ of ‘electromagnetic wave’ as ‘Analysis types’; chose the ‘Solver’: ‘Parametric’; define the ‘parameter names’ as ‘freq’ and ‘Parameter values’ as ‘lin-space(1e9, 20e9, 39)’, chose ‘Direct (UMFPACK)’ as ‘Linear system solver’, define the ‘Application scalar variables’ ‘nu_rfw’ as ‘freq’. Then we solve the simulation model. For a model with number of DOF 100000, the solving time is normally about 1-2 hours, for a model with number of DOF 150000, the solving time is about 3-5 hours, for a model with number of DOF 300000, the solving time is more than 8 hours. The solving time depends of the computer processor and the amount of memory.

- Visualizing simulated results

After the simulation has being done, the simulated results can be visualized. In the menu bar of ‘Postprocessing’, we can select ‘Global variables plot, where we can find the ‘Quantities to plot’, such as the S parameters, which will be shown in the coming section.

2.3.2 Modelling

2.3.2.1 Analytical modelling of CPW

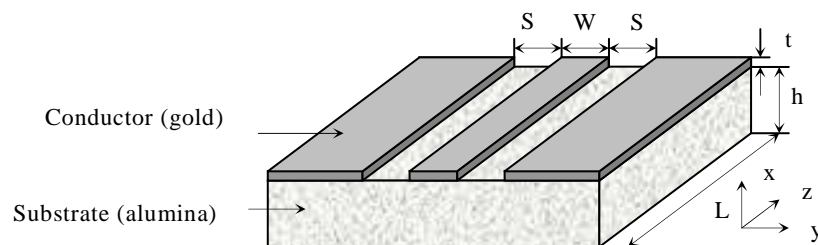


Figure 2.6 Geometry of CPW

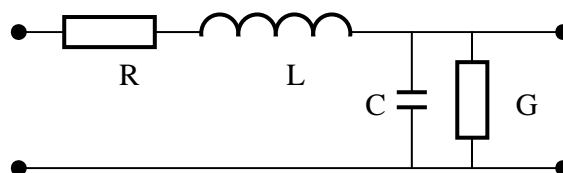


Figure 2.7 Equivalent circuit of CPW (elements defined per length)

A CPW on substrate alumina is shown in Figure 2.6, as CPW supports a quasi-TEM propagation mode. if the 2 following conditions are fulfilled

$$f \leq \frac{1}{10} \frac{1}{\sqrt{\mu_0 \epsilon_0 \epsilon_r}} \times \frac{1}{W + 2S}$$

$$h > 2(W + 2S)$$

An equivalent circuit model of CPW (Figure 2.7) was proposed by Heinrich[3]. Series resistance R, series inductance L, shunt capacitance C, and shunt conductance G can be extracted from the corresponding full-wave results [4]. It is found that the variation of shunt capacitance C with frequency remains negligible, while series resistance R and series inductance L exhibit evident frequency dependence. The dimensions of 3 CPWs on alumina ($\epsilon_r=9.8$) implemented in platform NANOLYON are reported in table 2.1.

Sample	W (μm)	G (μm)	h (μm)	t (μm)	L (mm)
CPW1	250	100	635	1	15
CPW2	72	40	635	1	15
CPW3	400	150	635X3	1	10

Table 2.1 Geometrical dimensions of CPWs on substrate alumina

The four elements R, L, C, and G depend on:

- For R and L, the transverse dimensions of CPW, the frequency, the conductivity of conductor and the frequency band. The R and L of CPW1, CPW2 and CPW3 are shown in Figure 2.8 and 2.9 respectively;
- For C, the dimensions of CPW and the substrate permittivity; the capacitance C of CPW1, CPW2 and CPW3 are 156 pF/m and 140 pF/m, respectively;
- For G, the dimensions of CPW, the frequency, the permittivity of substrate and the substrate loss tangent. Shunt admittance G of CPW1, CPW2 and CPW3 is shown in Figure 2.10.

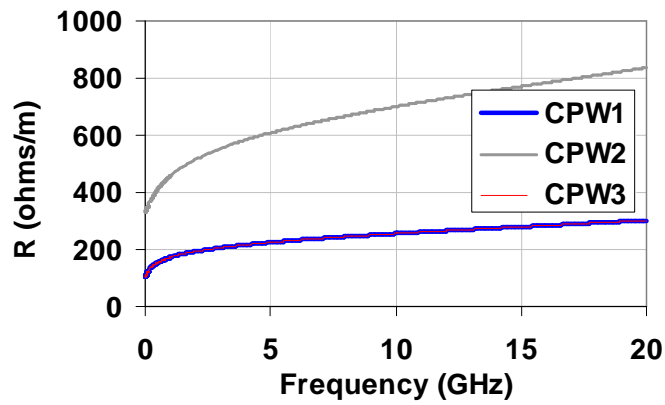


Figure 2.8 Series resistances of CPWs

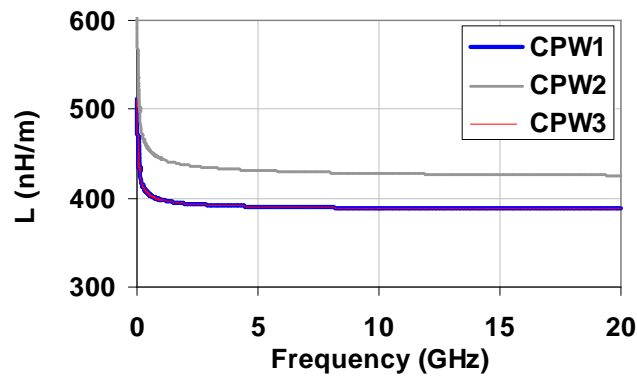


Figure 2.9 Series inductances L of CPWs

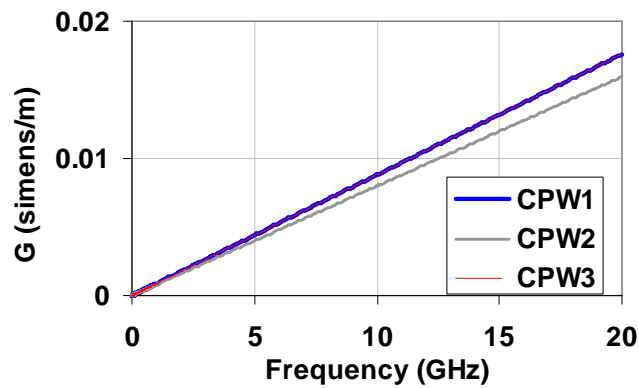


Figure 2.10 Shunt admittances G of CPWs

Three frequency bands are considered from DC to high frequency domain where the skin effect is accounted for.

The propagation constant γ_p and the characteristic impedance Z_c of CPW can be given by the previous calculated R, L, C, and G values

$$\gamma_p = \sqrt{(R + jL\omega)(G + jC\omega)} \quad (2.1)$$

$$Z_c = \sqrt{(R + jL\omega)/(G + jC\omega)} \quad (2.2)$$

The S parameters can be obtained by the calculated γ_p and Z_c . Here, the characteristic impedance Z_0 of feed port is 50 ohms, the reflection coefficient Γ and the transmission coefficient T can be calculated

$$\Gamma = (Z_c - Z_0)/(Z_c + Z_0) \quad (2.3)$$

$$T = e^{-\gamma_p L} \quad (2.4)$$

For reciprocal components,

$$S_{11} = S_{22} = \Gamma(1 - T^2)/(1 - \Gamma^2 T^2) \quad (2.5)$$

$$S_{12} = S_{21} = T(1 - \Gamma^2)/(1 - \Gamma^2 T^2) \quad (2.6)$$

The analytical results will be compared with the measured results and 3D electromagnetic simulations, as will be shown in Section 2.4.1.

2.3.2.2 Analytical modelling of gap capacitor

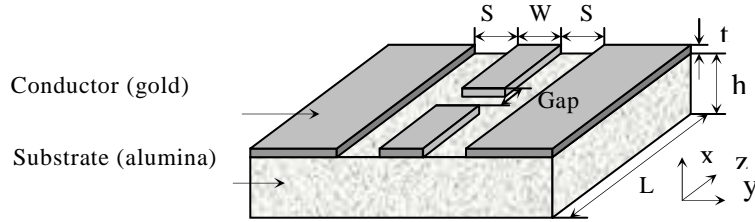


Figure 2.11 Geometry of CPW gap capacitor on alumina

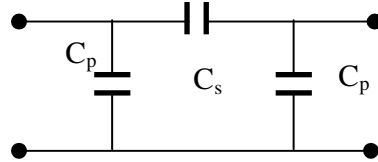


Figure 2.12 Equivalent circuit of CPW gap capacitor.

A CPW gap capacitor on alumina is shown in Figure 2.11, and its equivalent circuit is shown in Figure 2.12. For an infinitely thick substrate, using the quasi-static conformal mapping method, the closed form analytical equations for the equivalent C_s and C_p were developed by Gevorgian and N. Did [7-8]

$$C_p = 4\epsilon_0\epsilon_{eff} \left[\frac{K(k_3)}{K(k_3')} K(k) \frac{W}{2} - \frac{K(k)}{K(k')} L_m \right] \quad (2.7)$$

$$C_s = 2\epsilon_0\epsilon_{eff} \left[\frac{K(k_2)}{K(k_2')} - \frac{K(k_3)}{K(k_3')} \right] K(k) \frac{W}{2} \quad (2.8)$$

where

$$k = W / (W + 2S) \quad (2.9)$$

$$k_1 = \left[\frac{e^{\pi T} - 2}{e^{\pi T} + 2} \right]^2 \quad (2.10)$$

$$k_2 = sn \left[\frac{L_m}{L_m + (Gap / 2)} K(k_1), k_1 \right] \quad (2.11)$$

$$k_3 = k_1 k_2 \quad (2.12)$$

$$T = \frac{L_m + (Gap / 2)}{(W / 2) K(k')} \quad (2.13)$$

$$k' = \sqrt{1 - k^2} \quad (2.14)$$

$$k_i' = \sqrt{1 - k_i^2} \quad (i = 1, 2, 3) \quad (2.15)$$

$$L_m = (W * K(k') - Gap) / 2 \quad (2.16)$$

K represents the complete integral of the first kind, its values can be obtained by an integral or tabulated table, sn represents the Jacobian elliptic integral. It is indicated in [8] that, for gap smaller than 95 μm , the results given by equations (2.7) and (2.8) agree well with full-wave analysis results. The full wave method always give good results, its only drawback is that it takes a long time. In the coming section, the capacitance C of the gap capacitor denotes the C_s

2.3.2.3 Analytical modelling of interdigital capacitor (sample numbers 1,2,8,11)

The interdigital capacitor (IDC) is widely used in microwave and millimetre wave components. It enables to realize higher capacitances than gap capacitors. The first CPW IDC on microstrip line was demonstrated by Alley in 1970 [9]. CPW interdigital capacitor was introduced by M. Naghed and I. Wolff in 1990 [10]. 3D static finite difference method (FDM) was used to characterize the CPW interdigital capacitor. An equivalent circuit of 3 capacitors can be used to model the CPW IDC.

A CPW interdigital capacitor on alumina is shown in Figure 2.13, and its equivalent circuit with 3 capacitors is shown in Figure 2.14. For sake of simplicity, we keep the denotations of reference [13]. For a infinitely thick substrate, using the quasi-static conformal mapping method, the closed form analytical equations for the equivalent C_S and C_P were developed by Gevorgian and N. Did [7-8]

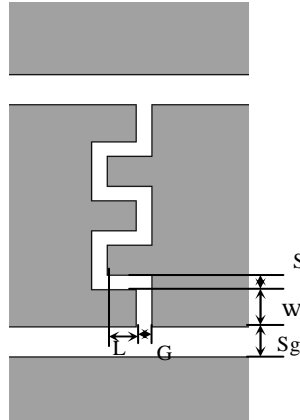


Figure 2.13 Top view of CPW interdigital capacitor, W – finger width, S – spacing between fingers, G – gap width at the end of one finger, L – overlap length between 2 fingers, S_g – CPW slot width.

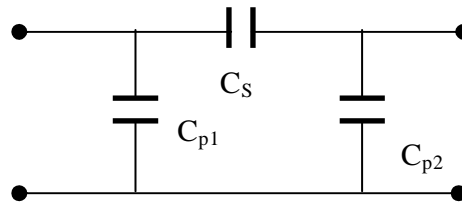


Figure 2.14 Equivalent circuit of CPW interdigital capacitor.

In order to take into account the metallization thickness t , the effective width is introduced by S. Gevorgian [12]

$$W_{eff} = W + \frac{t}{\pi} \left[1 + \ln \left(\frac{4\pi W}{t} \right) \right] \quad (2.17)$$

The capacitance C_s is the most important element for CPW IDC, it can be obtained by conformal mapping method, as presented in [12-13]. For a IDC with N fingers, the closed-form expression of C_s is

$$C_s = C_3 + C_N + C_{end} \quad (2.18)$$

Where C_3 is the capacitance of the three-finger part, C_N is the capacitance of remained $N-3$ fingers, and C_{end} is the capacitance of the open ends at the end of fingers [13].

$$C_3 = 4\epsilon_0\epsilon_e \frac{K(k_1)}{K(k_1')} L \quad (2.19)$$

$$\epsilon_e = 1 + \frac{K(k_1')}{K(k_1)} \frac{K(k_2)}{K(k_2')} \left(\frac{\epsilon_r - 1}{2} \right) \quad (2.20)$$

$$k_1 = \frac{W}{W+2S} \sqrt{\frac{1 - \left[\frac{W+2S}{3W+2S}\right]^2}{1 - \left[\frac{W}{3W+2S}\right]^2}} \quad (2.21)$$

$$k_2 = \frac{\sinh\left(\frac{\pi W}{4h}\right)}{\sinh\left(\frac{\pi(W+2S)}{4h}\right)} \sqrt{\frac{\sinh^2\left(\frac{\pi(3W+2S)}{4h}\right) - \sinh^2\left(\frac{\pi(W+2S)}{4h}\right)}{\sinh^2\left(\frac{\pi(3W+2S)}{4h}\right) - \sinh^2\left(\frac{\pi W}{4h}\right)}} \quad (2.22)$$

$$k_1' = \sqrt{1 - k_1^2} \quad (2.23)$$

$$k_2' = \sqrt{1 - k_2^2} \quad (2.24)$$

where $K(k)$ is the complete elliptic integral of the first kind. The ratio $K(k)/K(k')$ can be evaluated using Hilberg's approximate expressions.

$$\frac{K(k)}{K(k')} = \begin{cases} \frac{\pi}{\ln\left(\frac{2(1+\sqrt{k'})}{1-\sqrt{k'}}\right)}, & 0 \leq k \leq 0.707 \\ \frac{\ln\left(\frac{2(1+\sqrt{k'})}{1-\sqrt{k'}}\right)}{\pi}, & 0.707 \leq k \leq 1 \end{cases} \quad (2.25)$$

C_N can be evaluated by the following formulas [13]

$$C_N = (N-3)\epsilon_0\epsilon_N \frac{K(k_3)}{K(k_3')} L \quad (2.26)$$

$$\epsilon_N = 1 + \frac{K(k_3')}{K(k_3)} \frac{K(k_4)}{K(k_4')} \left(\frac{\epsilon_r - 1}{2}\right) \quad (2.27)$$

$$k_3 = \frac{W}{W+S} \quad (2.28)$$

$$k_4 = \frac{\sinh\left(\frac{\pi W}{4h}\right)}{\sinh\left(\frac{\pi(W+S)}{4h}\right)} \sqrt{\frac{\cosh^2\left(\frac{\pi(W+S)}{4h}\right) - \sinh^2\left(\frac{\pi(W+S)}{4h}\right)}{\cosh^2\left(\frac{\pi W}{4h}\right) - \sinh^2\left(\frac{\pi(W+S)}{4h}\right)}} \quad (2.29)$$

C_{end} is given in [8].

There are no expressions available for the shunt capacitance between the IDC and ground (C_{p1} and C_{p2}), S_g is usually chosen to be large enough to

reduce the shunt capacitance, that's also the case for us, so the C_{p1} and C_{p2} are neglected. In the coming sections, the C of an IDC denotes the C_s .

2.3.2.4 Analytical modelling of shunt inductor (sample numbers 3,19)

An inductor is a passive two-port component used to store energy; the inductor is characterized by the inductance measured in Henry. The inductor plays an important role in microwave and millimetre wave components. The CPW shunt inductor provides several attractive alternatives to conventional micro-strip lines: lower radiation loss, high compactness, without via to the ground, and easy fabrication. A CPW shunt inductor on alumina is shown in Figure 2.15, and its equivalent circuit is shown in Figure 2.16. The equivalent circuit has been analyzed by using a method of space domain integral equation (SDIE) in [8, 14-15].

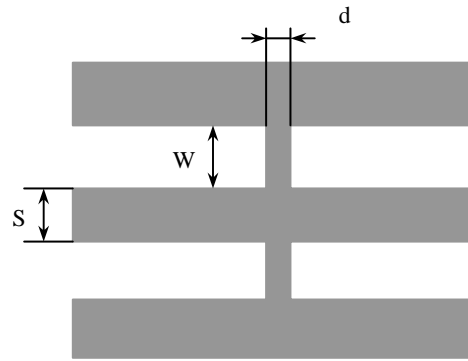


Figure 2.15 Top view of CPW shunt inductor

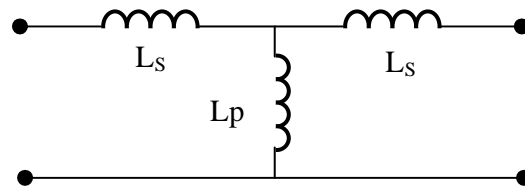


Figure 2.16 Equivalent circuit of CPW shunt inductor

There are 2 expressions for evaluating the shunt inductance L_p , the first one is to use the classical formula given by Everard in [16],

$$L_p = W \left[\ln \left(\frac{2\pi W}{d} \right) - 1 + \frac{d}{\pi W} \right] \quad (2.30)$$

The other expression is given by Getsinger in [17]:

$$L_p = W \left[\ln \left(\frac{1 + \sqrt{1 + R^2}}{R} \right) + R - \sqrt{1 + R^2} \right] \quad (2.31)$$

where $R = d/4W$, the unit of W is cm and that of L_p is nH.

In the 2 formulas, the shunt inductance is independent of permeability and permittivity.

The approximate expression for the series inductance L_s was derived in [8]. Note that L_s increases with d .

2.3.2.5 Calculation of capacitance and inductance from S parameters.

The ABCD of the capacitance and inductance can be calculated by S parameters [5], which are either measured or simulated.

$$A = \frac{(1 + S_{11})(1 - S_{22}) + S_{12}S_{21}}{2S_{21}} \quad (2.32)$$

$$B = \frac{(1 + S_{11})(1 + S_{22}) - S_{12}S_{21}}{2S_{21}} \times Z_C \quad (2.33)$$

$$C = \frac{(1 - S_{11})(1 - S_{22}) - S_{12}S_{21}}{2S_{12} \cdot Z_C} \quad (2.34)$$

$$D = \frac{(1 - S_{11})(1 + S_{22}) + S_{12}S_{21}}{2S_{12}} \quad (2.35)$$

Where Z_C is the characteristic impedance of feed line.

The ABCD matrix for series impedance and shunt impedance are given in Section 1.2.3, we deduce from that the ABCD matrix of the equivalent circuit of capacitance

$$\begin{bmatrix} A & B \\ C & D \end{bmatrix} = \begin{bmatrix} 1 & 0 \\ j\omega C_p & 1 \end{bmatrix} \begin{bmatrix} 1 & \frac{1}{j\omega C_s} \\ 0 & 1 \end{bmatrix} \begin{bmatrix} 1 & 0 \\ j\omega C_p & 1 \end{bmatrix} = \begin{bmatrix} 1 + \frac{C_p}{C_s} & \frac{1}{j\omega C_s} \\ 2j\omega C_p + \frac{j\omega C_p^2}{C_s} & 1 + \frac{C_p}{C_s} \end{bmatrix} \quad (2.36)$$

$$A = 1 + \frac{C_p}{C_s} \quad (2.37)$$

$$B = \frac{1}{j\omega C_s} \quad (2.38)$$

The capacitance can be extracted by ABCD parameters by using formulas giving below

$$C_s = \frac{1}{j\omega B} \quad (2.39)$$

$$C_p = (A - 1)C_s \quad (2.40)$$

Note that the S parameters used to extract capacitance values are the ones with the reference plane shifted according to the method which will be presented in Section 2.4. The extracted capacitance values using the measured and simulated S parameters will be shown in Section 2.4. For inductance, the ABCD matrix of the equivalent circuit

$$\begin{bmatrix} A & B \\ C & D \end{bmatrix} = \begin{bmatrix} 1 & j\omega L_s \\ 0 & 1 \end{bmatrix} \begin{bmatrix} 1 & 0 \\ \frac{1}{j\omega L_p} & 1 \end{bmatrix} \begin{bmatrix} 1 & j\omega L_s \\ 0 & 1 \end{bmatrix} = \begin{bmatrix} 1 + \frac{L_s}{L_p} & j2\omega L_s + \frac{j\omega L_s^2}{L_p} \\ \frac{1}{j\omega L_p} & 1 + \frac{L_s}{L_p} \end{bmatrix} \quad (2.41)$$

$$A = 1 + \frac{L_s}{L_p} \quad (2.42)$$

$$C = \frac{1}{j\omega L_p} \quad (2.43)$$

The inductance can be extracted from ABCD parameters by using the formulas giving below. For the normalized network:

$$L_p = \frac{1}{j\omega C} \quad (2.44)$$

$$L_s = (A - 1)L_p \quad (2.45)$$

We choose a reference plane quite close to the inductors ($\approx 50 \mu m$), so that the influence of L_s can be negligible.

2.4 Results of coplanar components on alumina

2.4.1 CPW on substrate alumina

A CPW prototype on substrate alumina is shown in Figure 2.17, in our design, for matching the size of cascade probe GSC 500 [20], W+2G should be smaller than 1000 μm . According to Equation 1.122, to get a characteristic impedance Z_0 50 ohms (impedance of coaxial feed line), we can properly adjust centre conductor width W and slot width G of CPW.

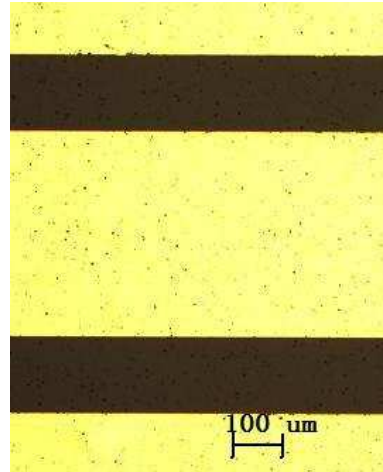


Figure 2.17 Top view of CPW prototype on alumina

2.4.1.1 *S* parameters

The analytical results will be compared with the experimental results and 3D electromagnetic simulations, as will be shown in the following sections.

The measurements are performed with a 65GHz vector network analyzer (Anritsu A37397) and a probing system with a SOLT calibration. The transmission coefficients (S_{21} and S_{12}) and the reflection coefficients (S_{11} and S_{22}) are measured. The analytical and simulated results are also given for comparison.

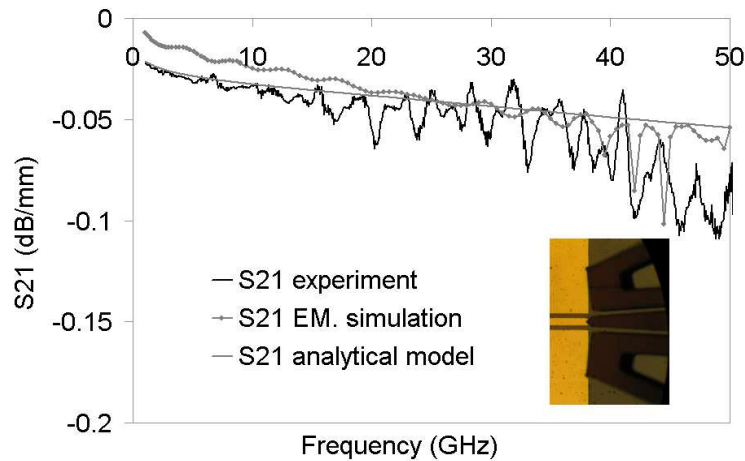


Figure 2.18 Transmission coefficients S_{21} of CPW1

For CPW1, the S_{21} results are presented in Figure 2.18 whereas the S_{11} results are presented in Figure 2.19. For CPW2, the S_{21} results are presented in Figure 2.20 whereas the S_{11} results are presented in Figure 2.21. The characteristic dimensional resonances can be seen in Figure 2.19 and 2.21, since they occur when $k\lambda_g = 2L$, λ_g being the guided wavelength. Here we don't indicate

the S parameters of CPW3, that is because the S parameters of CPW3 is pretty the same as that of CPW1.

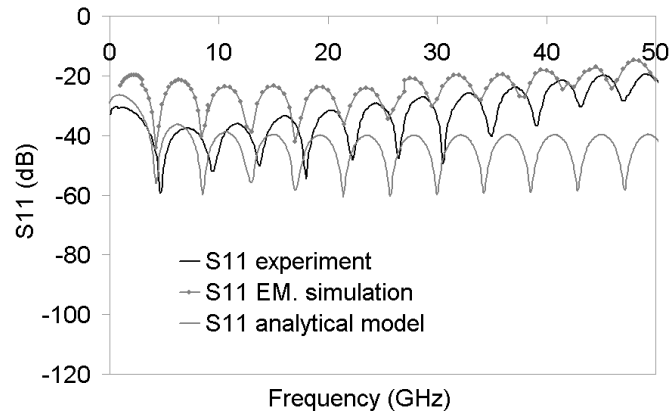


Figure 2.19 Reflection coefficients S_{11} of CPW1

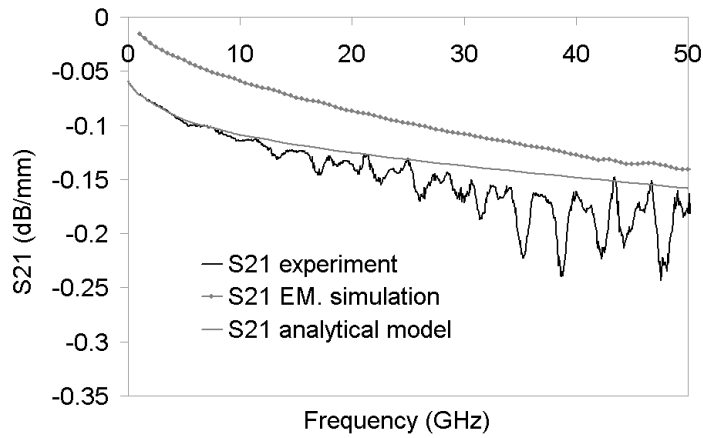


Figure 2.20 Transmission coefficients S_{21} of CPW2

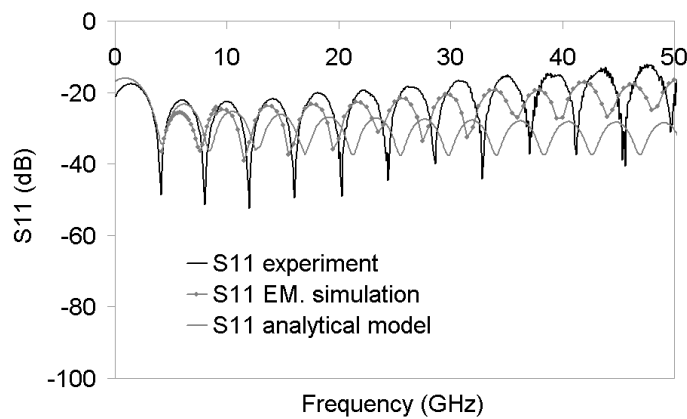


Figure 2.21 Reflection coefficients S_{11} of CPW2

2.4.1.2 Propagation constant

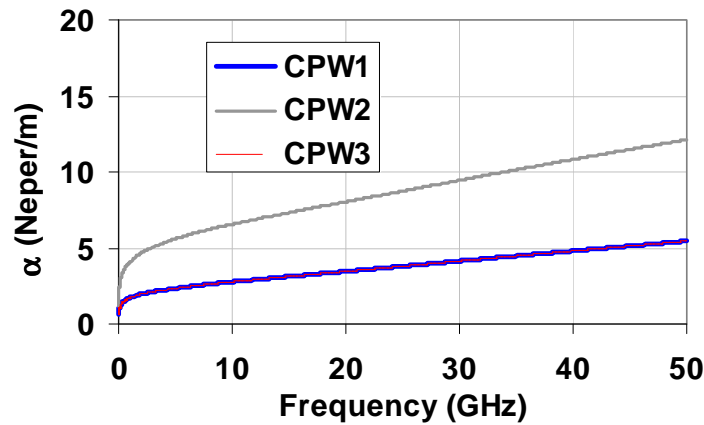


Figure 2.22 Attenuation constants of CPWs

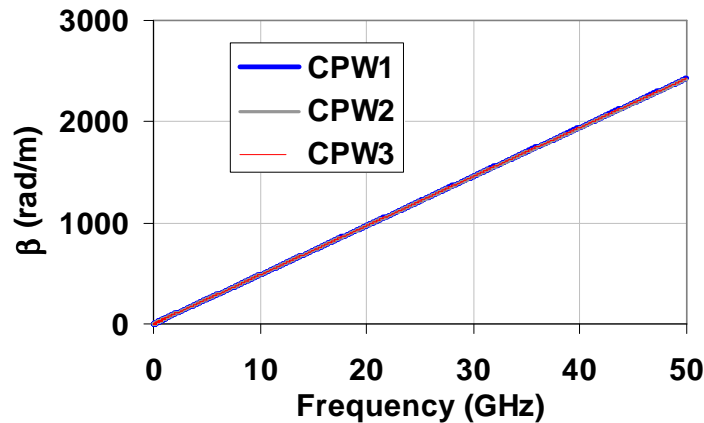


Figure 2.23 Phase constants β of CPWs

To get more insight into the wave propagation on CPWs, the terms of the propagation constants γ , α attenuation constant and β phase constant are shown in Figure 2.22 and Figure 2.23 respectively. The attenuation of CPW2 is higher than CPW1. This is essentially due to the fact that the centre conductor width of CPW1 is about 4 times greater than that of CPW2. The attenuation constant has a direct effect on the transmission coefficient, and consequently, the transmission parameters of CPW1 are better than those of CPW2. The phase constants of CPW1 and CPW2 are the same, so does the phase velocity $V_\varphi = \omega/\beta$ for both types of CPWs that reaches $1.28 \cdot 10^8$ (m/s).

2.4.1.3 Shift in reference planes

The S parameters fully characterize the amplitudes of incident and reflected travelling waves a and b of the CPW transmission line, the phase reference planes can be specified for each port of CPW [5-6].

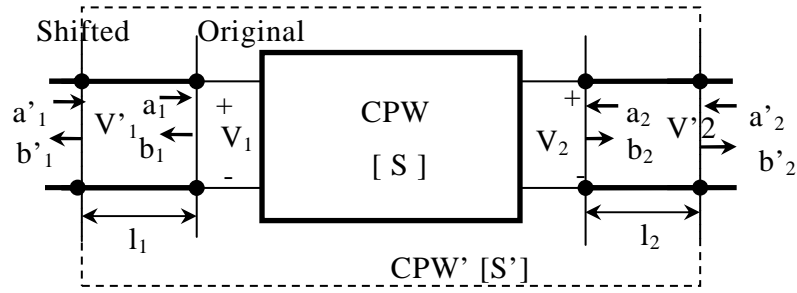


Figure 2.24 The network with shifted reference plane

Consider a 2-port CPW as shown in Figure 2.24, the original terminal and the shifted planes are arbitrary set along the CPW TL connected to the ports.

The S parameters matrix for the CPW with original terminals is denoted by $[S]$,

$$\begin{bmatrix} b_1 \\ b_2 \end{bmatrix} = \begin{bmatrix} S_{11} & S_{12} \\ S_{21} & S_{22} \end{bmatrix} \begin{bmatrix} a_1 \\ a_2 \end{bmatrix} \quad (2.46)$$

And the S parameters matrix for the CPW with reference plane shifted is denoted by $[S']$,

$$\begin{bmatrix} b'_1 \\ b'_2 \end{bmatrix} = \begin{bmatrix} S'_{11} & S'_{12} \\ S'_{21} & S'_{22} \end{bmatrix} \begin{bmatrix} a'_1 \\ a'_2 \end{bmatrix} \quad (2.47)$$

For lossless TL, the incident and reflected waves can be written as:

$$a'_1 = e^{j\beta l_1} a_1 \quad (2.48)$$

$$b'_1 = e^{-j\beta l_1} b_1 \quad (2.49)$$

$$a'_2 = e^{j\beta l_2} a_2 \quad (2.50)$$

$$b'_2 = e^{-j\beta l_2} b_2 \quad (2.51)$$

The matrix form of the above equations is given by:

$$\begin{bmatrix} b'_1 \\ b'_2 \end{bmatrix} = \begin{bmatrix} e^{-j\beta l_1} & 0 \\ 0 & e^{-j\beta l_2} \end{bmatrix} \begin{bmatrix} b_1 \\ b_2 \end{bmatrix} \quad (2.52)$$

$$\begin{bmatrix} a_1 \\ a_2 \end{bmatrix} = \begin{bmatrix} e^{-j\beta l_1} & 0 \\ 0 & e^{-j\beta l_2} \end{bmatrix} \begin{bmatrix} a'_1 \\ a'_2 \end{bmatrix} \quad (2.53)$$

By substituting Equation 2.46 to the above equations, we obtain:

$$\begin{aligned} \begin{bmatrix} b'_1 \\ b'_2 \end{bmatrix} &= \begin{bmatrix} e^{-j\beta l_1} & 0 \\ 0 & e^{-j\beta l_2} \end{bmatrix} \begin{bmatrix} S_{11} & S_{12} \\ S_{21} & S_{22} \end{bmatrix} \begin{bmatrix} a_1 \\ a_2 \end{bmatrix} \\ &= \begin{bmatrix} e^{-j\beta l_1} & 0 \\ 0 & e^{-j\beta l_2} \end{bmatrix} \begin{bmatrix} S_{11} & S_{12} \\ S_{21} & S_{22} \end{bmatrix} \begin{bmatrix} e^{-j\beta l_1} & 0 \\ 0 & e^{-j\beta l_2} \end{bmatrix} \begin{bmatrix} a'_1 \\ a'_2 \end{bmatrix} \end{aligned} \quad (2.54)$$

The comparison of Equation 2.54 with Equation 2.47, leads to:

$$[S'] = \begin{bmatrix} S_{11}e^{-2j\beta l_1} & S_{12}e^{-j\beta(l_1+l_2)} \\ S_{21}e^{-j\beta(l_1+l_2)} & S_{22}e^{-2j\beta l_2} \end{bmatrix} \quad (2.55)$$

If the CPW is replaced by a microwave network like a capacitor or an inductor, a shift in the reference plane is performed using Equation 2.55, in order to extract the values of capacitor or inductor.

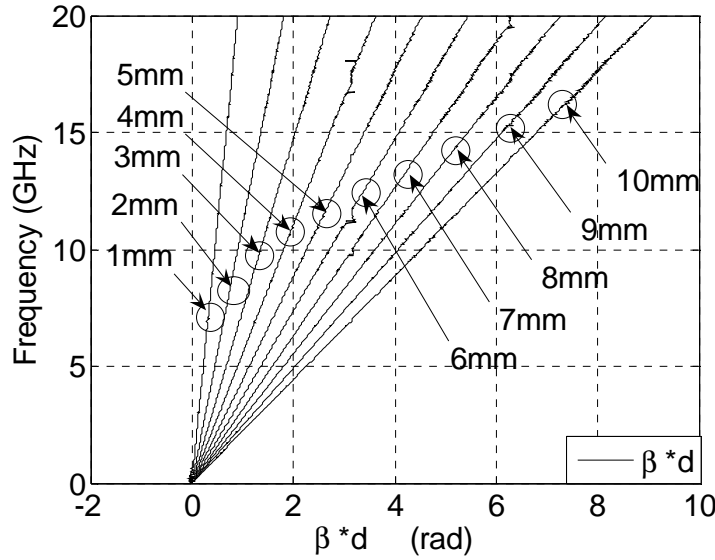


Figure 2.25 Phase shift $\beta*d$ of CPWs with length from 1 mm to 10 mm
(Calculated from measured S parameters)

As we know that the phase velocity of the CPW

$$V_p = \omega / \beta = 2\pi * f / \beta, \quad (2.17)$$

$$\beta * d = (2\pi * f / V_p) * d \quad (2.18)$$

One example of the usage of the method of change in reference planes is shown in Figure 2.25, the dimensions of the CPW is: centre conductor width $400 \mu\text{m}$, gap width $150 \mu\text{m}$, length 10mm . The lines in the figure other than length $10 \mu\text{m}$ are calculated by the method of change in reference planes. These results agree well with the $\beta*d$ predicted by Equation 2.18, which improve that, if we could get the $\beta*d$ of a CPW, we can get the $\beta*d$ of any this kind of CPW with length changes.

2.4.2 Coplanar gap capacitor (sample 18-10 μm 22-30 μm 23-6 μm 24-20 μm)

A capacitor is a passive two-port component used to store energy; the capacitor is characterized by the capacitance measured in farads. The capacitor plays an important role in microwave and millimetre wave components. In our work, 2 types of series capacitors, gap capacitor and interdigital capacitors are used to build a composite right/left-handed transmission lines. The properties of single capacitors embedded in CPW will be studied in this section.

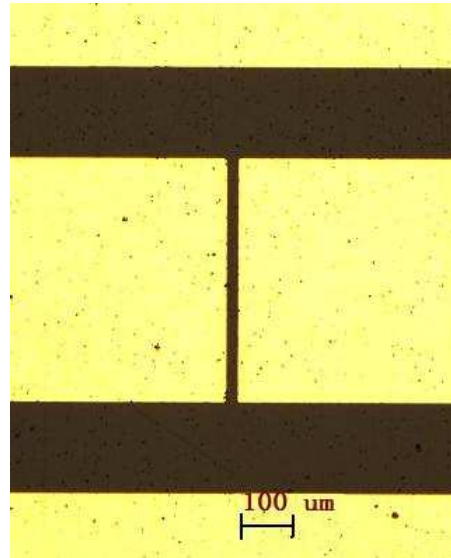


Figure 2.26 Top view of a CPW gap capacitor prototype on alumina

In our work, CPW gap capacitors with gap 10 μm , 20 μm and 30 μm are designed, the capacitors dimensions are shown in table 2.2.

Sample	Gap (μm)	W (μm)	G (μm)	h (μm)	t (μm)	Lrf(mm)
Capacitor 1 (18)	10	400	150	635x3	1	4.995
Capacitor 2 (24)	20	400	150	635x3	1	4.99
Capacitor 3 (22)	30	400	150	635x3	1	4.985

Table 2.2 Geometrical dimension of CPW gap capacitors on substrate alumina, Lrf is shifted length of each reference plane, the total length of sample is 10mm.

2.4.2.1 Measured and simulated S parameters

Three gap capacitors with gap 10 μm , 20 μm , and 30 μm were implemented; the measured and 3D full wave simulation S parameters are given in figures 2.27 to 2.28. Figure 2.27 depicts the measured and simulated S parameters of gap capacitors, whereas Figure 2.28 shows a zoom of measured S_{21} parameters.

The gap capacitor works obviously as a high pass microwave network, as only high frequency signal can propagate through the gap capacitor. The S_{21} parameter decreases when the gap increases between $10\ \mu\text{m}$ to $30\ \mu\text{m}$. For example, the S_{21} parameter decreases from $-16.5\ \text{dB}$ to $-19.8\ \text{dB}$ at $4\ \text{GHz}$.

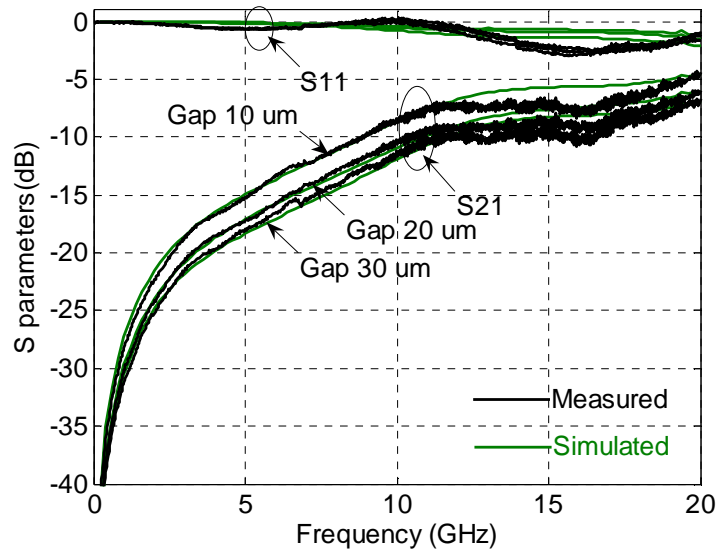


Figure 2.27 Measured and simulated S parameters of gap capacitors, gap width $10\ \mu\text{m}$, $20\ \mu\text{m}$ and $30\ \mu\text{m}$

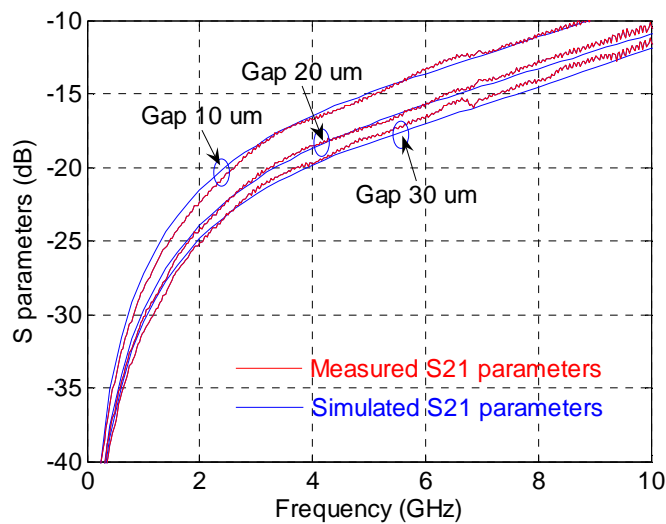


Figure 2.28 Zoom of measured and simulated S_{21} parameters of gap capacitors, gap width $10\ \mu\text{m}$, $20\ \mu\text{m}$ and $30\ \mu\text{m}$

2.4.2.2 Values of capacitors

The capacitance can be extracted from ABCD parameters by using the formulas given in Section 2.3.

Note that the S parameters used to extract capacitance values should take into account the change in reference plane. The shift in reference plane is implemented according to the method mentioned in Section 2.4.1.3. The extracted capacitance values, using the measured and simulated S parameters, are shown in Figure 2.29.

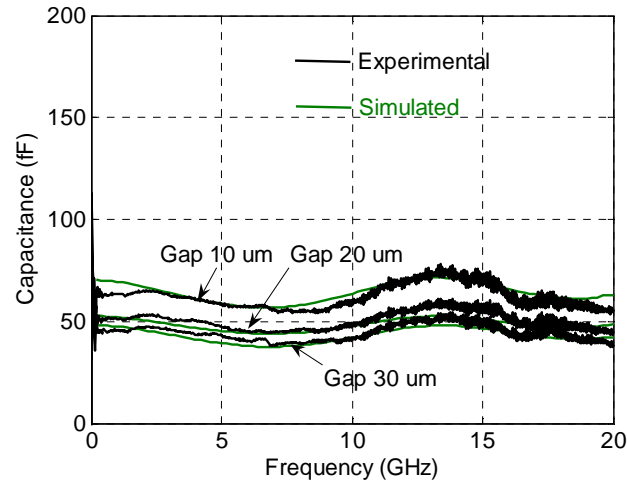


Figure 2.29 Experimental and simulated capacitance values, gap width 10 μm , 20 μm and 30 μm

The capacitances values that calculated by measured S parameters and simulated S parameters agree well. It is shown that the capacitance values decrease when the gap increases. For a gap increases from 10 μm to 30 μm , the simulated capacitance decrease from 62 fF to 46 fF, the experimental capacitance decrease from 60 fF to 45 fF. We find that the analytical results of C_S are almost twice those extracted from experimental and simulated results. In [8] N.dib also gets a high discrepancy between experimental and analytical results.

Sample	Gap (μm)	Capacitance simulated (fF)	Capacitance experimental (fF)	Capacitance analytical (fF)
Capacitor 1 (18)	10	62	60	106
Capacitor 2 (24)	20	52	50	90
Capacitor 3 (22)	30	46	45	80

Table 2.3 Extracted capacitances values (averaged over the frequency range)

2.4.3 Coplanar interdigital capacitor (sample 8,11)

A CPW interdigital capacitor prototype on alumina is shown in Figure 2.30.

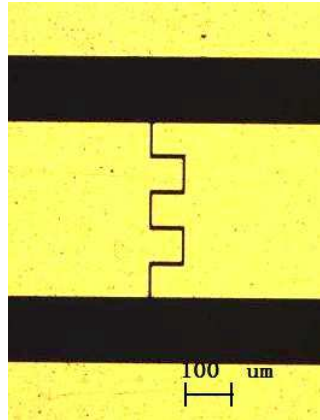


Figure 2.30 Top view of CPW interdigital capacitor prototype on alumina (gap width $10\ \mu\text{m}$). In our work, 2 types of CPW interdigital capacitors were designed.

Sample	S (μm)	L (μm)	W (μm)	Sg (μm)	G (μm)	Lrf (mm)
Capacitor 1 (8)	10	65	72	150	10	4.96
Capacitor 2 (11)	10	90	72	150	10	4.95

Table 2.4 Geometrical dimension of interdigital capacitors on substrate alumina. S, L, W, Sg, G are defined in Figure 2.13. Lrf is the shifted length of each reference plane. The total length of the sample is 10mm.

2.4.3.1 Measured and simulated S parameters

The measured and 3D full wave simulation S parameters of IDC 1 and IDC 2 are given in Figure 2.31 and a zoom is presented in Figure 2.32. The length of the components is about $100\ \mu\text{m}$ in COMSOL, which represents a shift in reference plane of 4.95 mm.

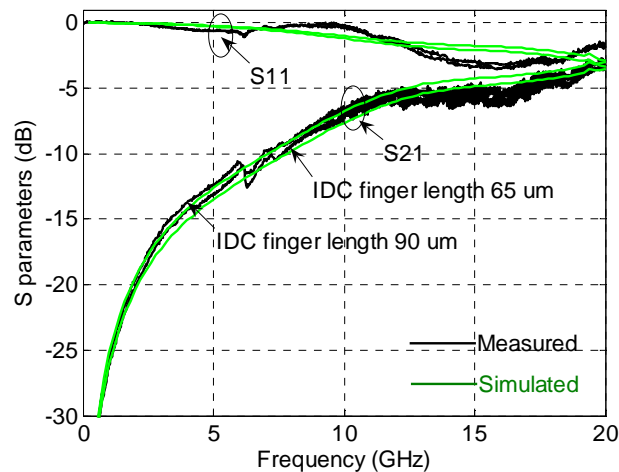


Figure 2.31 Measured and simulated S parameters of IDC, overlapped finger length $65\ \mu\text{m}$ and $90\ \mu\text{m}$

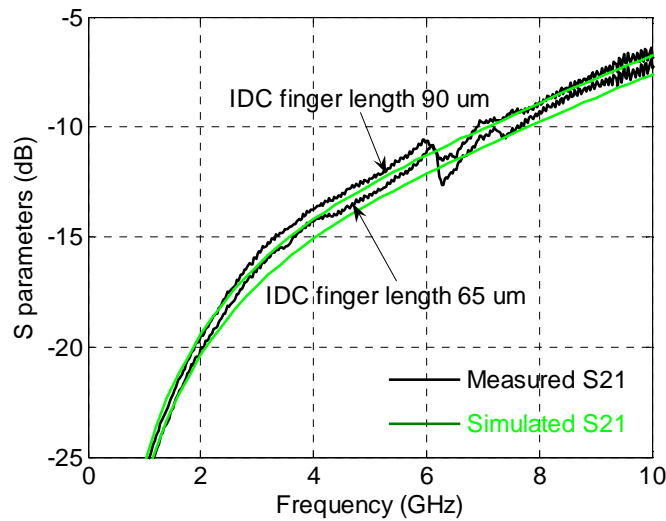


Figure 2.32 Zoom of measured and simulated S_{21} parameters of IDC, overlapped finger length 65 μm and 90 μm

As in the case of the gap capacitor, the series IDC work behaves as a high pass microwave network. At a given frequency, the S_{21} parameter increases with overlapped finger length. For a finger length increase from 65 μm to 90 μm , the S_{21} parameters increase from -13.8 dB to -14.3 dB at 4 GHz.

2.4.3.2 Values of capacitors

The capacitances are extracted by ABCD parameters by using formulas from 2.32 to 2.35 from Section 2.3.2.5.

Figure 2.33 indicates the experimental and simulated capacitance values of IDC, the capacitance values that calculated by measured S parameters and simulated S parameters agree well (up to 10 GHz). It is shown that the capacitance values increase with overlapped finger length increase. Comparing with CPW gap capacitor, the CPW IDC has a bigger capacitance value. With the same gap of 10 μm , a gap capacitor has a capacitance of 60 fF, whereas the IDC which is 80 fF which is expected.

For comparison, the CPW IDC analytical values are calculated with formulas presented in Section 2.3, the capacitance results are also indicated in Table 2.5, the experimental results agree with full wave results, but the analytical results is not as good as full wave simulation results. N.Dib also gets a high discrepancy between experimental and analytical results. In fabrication, the limit of dimension is about 5 μm . If the finger length increases, the equivalent circuit doesn't fit the condition of Figure 2.14; a series inductor should be added to the figure.

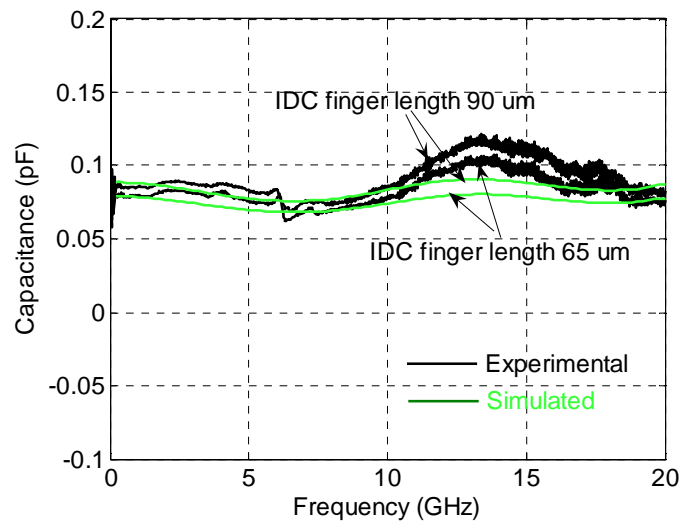


Figure 2.33 Experimental and simulated capacitance values of IDC, overlapped finger length 75 μm and 100 μm

Sample	L (μm)	Experimental (fF)	Simulated (fF)	Analytical (fF)
Capacitor1 (8)	65	≈ 78	≈ 82	≈ 60
Capacitor2 (11)	90	≈ 82	≈ 85	≈ 68

Table 2.5 Extracted capacitances values of IDC (averaged over the frequency range)

2.4.4 Coplanar shunt inductor

The properties of single CPW shunt inductor will be studied in this section.

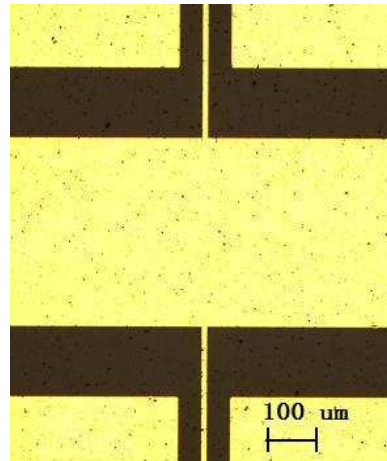


Figure 2.34 Top view of CPW shunt inductor prototype on alumina. The width of inductance is 10 μm , and the width between inductance and ground plane is 50 μm .

The CPW shunt inductor provides several attractive alternatives to conventional micro-strip lines lower radiation loss, high compactness, without via to the ground, and easy fabrication.

In our work, 2 inductors with different length are studied: one with length 1150 μm and the other with length 650 μm . The detail of dimensions and corresponding analytical results are shown in Table 2.6.

Sample	W (μm)	S (μm)	d (μm)	Lrf (mm)	Formula 2.30 (pH)	Formula 2.31 (pH)
Inductor 1 (19)	1150	400	10	4.94	640	670
Inductor 2 (3)	650	400	10	4.94	330	340

Table 2.6 Geometrical dimensions of CPW shunt inductors on alumina and analytical results. Lrf is the shifted length of each reference plane. The total length of the sample is 10.13 mm. The geometrical parameters are defined in Figure 2.15.

2.4.4.1 Measured and simulated S parameters

S parameters are given in figure 2.35 and 2.36, for a length of 1150 μm and 650 μm respectively. The CPW shunt inductor behaves like a high pass network, the S_{11} is quite close to 0 dB at lower frequencies, the S_{21} is smaller than -30dB at 1GHz, that is because the shunt inductor is connected in parallel between the centre conductor and the ground plane.

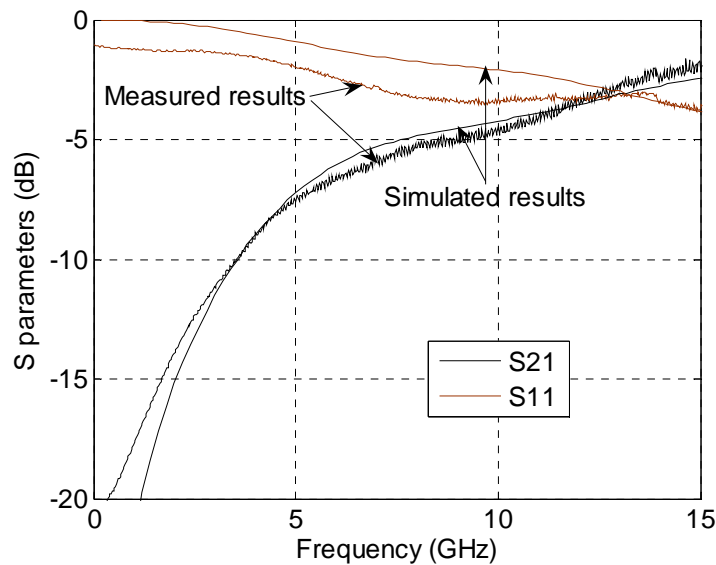


Figure 2.35 Measured and simulated S parameters of shunt inductor (length 1150 μm)

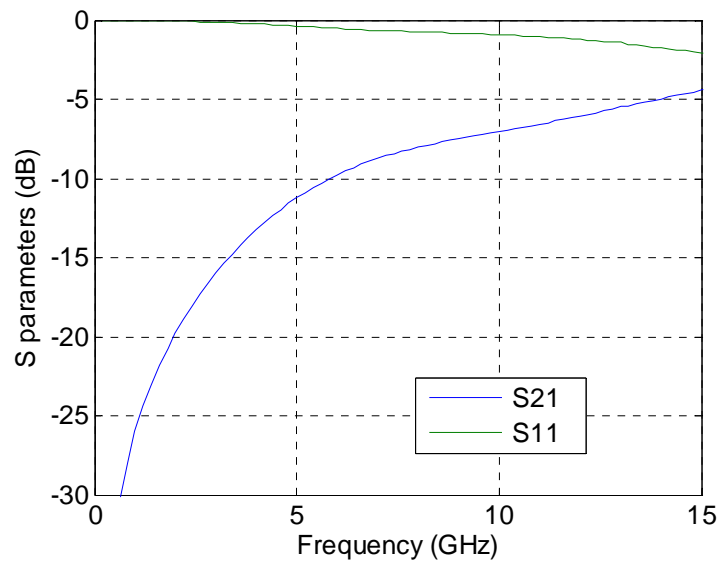


Figure 2.36 Simulated S parameters of shunt inductor (length 650 μm)

2.4.4.2 Values of inductors

The extracted inductance values L_p are shown in Figure 2.37 and Figure 2.38. We can see that the inductance values change with frequencies change. The inductances increase with inductor length. The inductances simulated are a little smaller than inductances experimental (about 0.05-0.1 nH). The experimental and simulated values of inductors are different from analytical results. In fact, in the analytical modelling, the equivalent circuit of inductor has just one shunt inductor, while in reality the equivalent circuit has also 2 shunt capacitors.

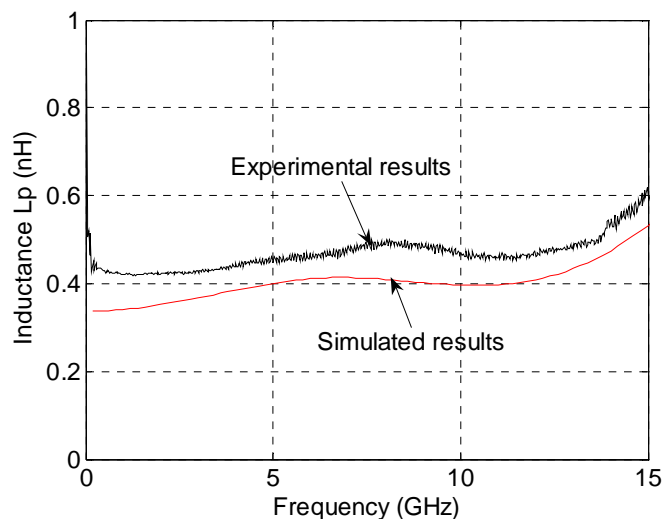


Figure 2.37 Experimental and simulated inductance of shunt inductor L_p (inductor 1),

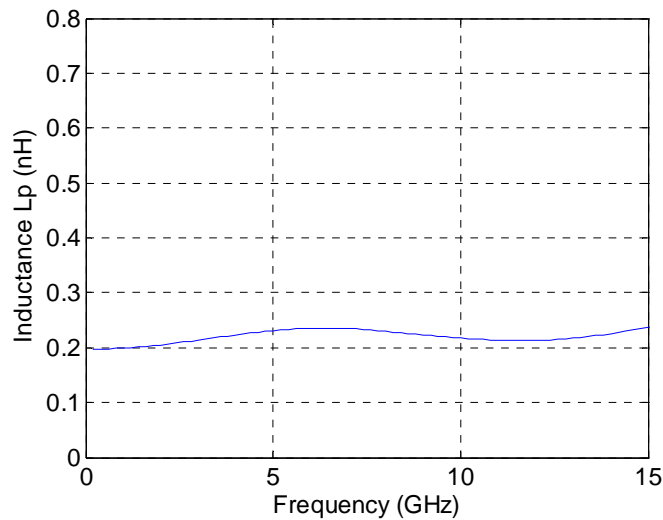
(length 1150 μm)

Figure 2.38 Simulated inductance of shunt inductor L_p (length 650 μm) (inductor 2)

2.5 Conclusion

In this chapter, CPW components on substrate alumina are designed and implemented. The fabrication processes in NANOLYON is presented in Section 2.2, the simulations in software COMSOL and the analytical modelling approaches in Matlab is studied in Section 2.3; then the measured and simulated S parameters, the corresponding propagation constants of CPW, and the extracted values of capacitance and inductance are given in Section 2.4. The measured, simulated and analytical S parameters are shown; the experimental, simulated, analytical values of capacitors and inductors are given. For the gap capacitors, the highest capacitance is obtained when the gap is 10 μm , and it reaches 60 fF. A slightly larger value of the capacitance is obtained for a 5 finger IDC that reaches 80 fF. The overlap length between 2 fingers is then 90 μm . Lastly, for the inductances, measured values of inductances of 200 and 400 pH can be measured for a length of 650 to 1150 μm respectively.

2.6 Bibliography

- [1] **SIMONS R.N.** « Coplanar waveguide circuits components and systems », John Wiley & Sons, 2001, 464p.
- [2] **NGUYEN C.** « Analysis methods for RF, microwave, millimeter-wave planar transmission line structures », New York, John Wiley & Sons, 2000, 240 p.
- [3] **HEINRICH W.** Quasi-TEM description of MMIC coplanar lines including conductor-loss effects. *IEEE Trans Microwave Theory Tech* Vol.41, 1993, pp. 45-52.
- [4] **HEINRICH W.** Full-wave analysis of conductor losses on MMIC Transmission Lines. *IEEE Trans Microwave Theory Tech*, Vol. 38, No. 10, 1990, pp. 1468-1472.
- [5] **POZAR D.M.** « Microwave engineering », third edition, John Wiley & Sons, 2004, 720 p.
- [6] **KINAYMAN N., AKSUN M.I.** « Modern Microwave Circuits », Norwood, Artech house, 2005, 624 p.
- [7] **GEVORGIAN S., DELENIV A., MARTINSSON T., et al.** CAD model of a gap in a coplanar waveguide. *International Journal of microwave and millimeter-wave computer-aided engineering*, Vol.6, No. 5, 1996, pp. 369-377.
- [8] **DIB N.I.** Comprehensive study of CAD models of several coplanar waveguide (CPW) discontinuities. *IEEE proceedings Microwaves, antennas and propagation*, Vol. 152, No. 2, 2005, pp. 69-76.
- [9] **ALLEY G.D.** Interdigital capacitors and their application to lumped-element microwave-integrated circuits. *IEEE Trans Microwave Theory Tech*, Vol. 18, No.12, 1970, pp. 1028-1033.
- [10] **NAGHED M., WOLFF I.** Equivalent capacitance of coplanar waveguide discontinuities and interdigital capacitors using a three-dimensional finite difference method. *IEEE*

- Trans Microwave Theory Tech, Vol. 38, No. 12, 1990, pp.1808-1815.
- [11] **KULKE R., POGATZKI P., KOTHER D., et al.** Enhancement of coplanar capacitor models and verification up to 67 GHz for (M)MIC circuit design, Proc. 24th European Microwave Conf. Dig., Vol. Cannes, France, 1994, pp 258-262.
- [12] **GEVORGIAN S.S., MARTINSSON T., LINNÉR P.L.J, et al.** CAD models for multilayered substrate interdigital capacitors. IEEE Trans Microwave Theory Tech, Vol. 44, No. 6, 1996, pp. 896-904.
- [13] **DIB N., ABABNEH J., OMAR A.** CAD modeling of coplanar waveguide interdigital capacitor. International journal of RF and microwave and millimeter-wave computer-aided engineering. Vol. 14, No.6, 2005, pp. 551-559.
- [14] **DIB N. I., PONCHAK G. E., KATEHI L. P. B.** A theoretical and experimental study of coplanar waveguide shunt stubs. IEEE Trans. Microwave Theory Tech., Vol. 41, No. 1, 1993, pp. 38-44.
- [15] **DIB N.I., GUPTA M., PONCHAK G. E., et al.** Characterization of asymmetric coplanar waveguide discontinuities. IEEE Trans. Microw. Theory Tech., Vol. 41, No. 9, 1993, pp. 1549-1558.
- [16] **EVERARD J.K.A, CHENG K.K.M.** High performance direct coupled bandpass filters on coplanar waveguide. IEEE Trans. Microw. Theory Tech., Vol. 41, No.9, 1993, pp. 1568-1573.
- [17] **GETSINGER W.** Circuit duals on planar transmission media. IEEE MTT-S Int. Microwave Symp. Digest, 1983, pp. 154-156.
- [18] NANOLYON. http://inl.ec-Lyon.fr/index.php?option=com_content&task=view&id=20&Itemid=43

- [19] COMSOL Multiphysics.
<http://www.comsol.com/products/multiphysics/>
- [20] Cascade prob. <http://www.cmicro.com/products/probes/rf-microwave/infinity-probe/infinity-probe>

3 Coplanar components on ferrite

3.1 Introduction

The first microwave ferrite device was produced in 1949, and the first coplanar waveguide with ferrite material was demonstrated in 1969 [1]. The development of this type of device was strongly related to the knowledge of spin interaction in ferrite materials [2-4]. The ferrite materials can be applied to many microwave components such as isolators [5], circulators [6], which are very important because there is no alternative semiconductor device that satisfies similar requirements. The behaviour of microwave wave ferrite devices is based on the gyromagnetic property of ferrite materials. Some effects of ferrite materials can be used to provide a nonreciprocal propagation of wave, such as ferromagnetic resonance, Faraday rotation, and field displacement. In this chapter, the properties of ferrites will be presented. CPW components on ferrites like CPW on ferrite BaM and ferrite YIG with applied field and without applied field, capacitors and inductors on ferrite YIG will be presented. We will then go over to the fabrication steps on massive ferrite (YIG) when it differs from those on alumina. After describing how to modelize, simulate the material, and calculate the propagation constant, we will give the results obtained for coplanar components on ferrite.

3.2 Ferrite material

A ferrite is a magnetic iron oxide compound made of oxygen ions and metal cations. Ferrite can be magnetically soft or hard materials. Among them we can distinguish spinel, garnet and hexaferrite according to their crystal lattice structure. The possibility of changing the composition to adjust their properties is one very attractive feature of ferrites. Ferrites with different compositions are given in Table 3.1.

Spinel	(Mg-Zn)Fe ₂ O ₄ , (Mn-Zn)Fe ₂ O ₄ , (Ni-Zn)Fe ₂ O ₄ , Li _{0.5} Fe _{2.5} O ₄ ,
Garnets	YIG: Y ₃ Fe ₅ O ₁₂ , substituted YIG (Ga, Al, Cr, In, Sc) and rare earth substituted YIG (La, Pr, Nd, Sm, Eu, Gd, Tb, Dy, Ho, Er, Yb, Lu)
Hexaferrite	M type: BaFe₁₂O₁₉ (BaM) and substituted (easy axis); Y, Z type (easy plane)

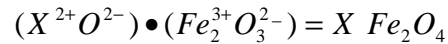
Table 3.1 Ferrites with different compositions

As a high resistivity material, the ferrite material is very suitable for millimeter wave components. Due to the high resistivity, a wave can indeed penetrate and interact with material. Their relative permittivity is almost constant at microwave frequencies and close to 15 for YIG materials. Their perme-

ability is the fundamental property as it governs interaction between the wave and the material. Low coercivity is necessary for low losses. High saturation magnetization means a high gyromagnetic and isotropy but also an intense field to saturate the material [7-10].

3.2.1 Spinel

Spinel ferrites are the first ferrite materials using in microwave components, their linewidths vary from 15 kA/m to 35 kA/m. Its chemical formula is

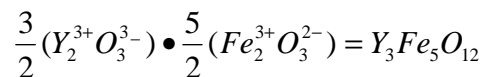


The Curie temperature of the nickel mixed ferrite is around $570^\circ C$, the saturation magnetization is around 320 mT. It is a lossy material, for it contains a relaxing Ni ion. A lower magnetization down to 140mT can be obtained by aluminium substitution for iron, and a higher saturation magnetization up to 480mT can be obtained by partial substitution of zinc for nickel.

The Curie temperature of the lithium mixed ferrite is around $645^\circ C$, the saturation magnetization is about 360mT. It has a low loss and narrow line width, for it lacks the divalent iron ions. A lower magnetization down to 230mT can be obtained by Ti substitution, and a higher saturation magnetization up to 500mT can be obtained by Zn substitution.

3.2.2 Garnet

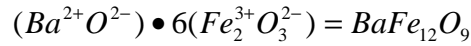
Yttrium iron Garnet (YIG) is a narrow line width ferrite (3kA/m). For it has a weak saturation magnetization (175mT-180mT), it can be easily saturated. It has low temperature stability for the Curie temperature is $286^\circ C$. Its chemical formula is



The saturation magnetization and the Curie temperature decrease by aluminium substitution of iron ions and the saturation magnetization also decreases by Gd substitution of Y ions. A narrow line width (0.8kA/m) can be obtained by In or Zn substitutions. The details of this soft ferrite will be studied in the coming section.

3.2.3 Hexaferrite

Hexaferrites have a hexagonal structure with a c-axis of symmetry. They have a crystalline structure which is essentially uniaxial of the M-type, its chemical formula is



They have a high saturation magnetization (480 mT) and a Curie high temperature $700^\circ C$. They also have a high magneto crystalline anisotropy, which results in an anisotropy field H_a (around 1400 kA/m) that has to be taken into account in the internal field.

3.3 Fabrication of coplanar components on YIG

The YIG substrate used in this work to process coplanar structures is commercial material from the TEMEX society (Y101). It consists of square substrates having the following dimensions: $50.8 \times 50.8 \text{ mm}^2$, with thickness of 1mm.

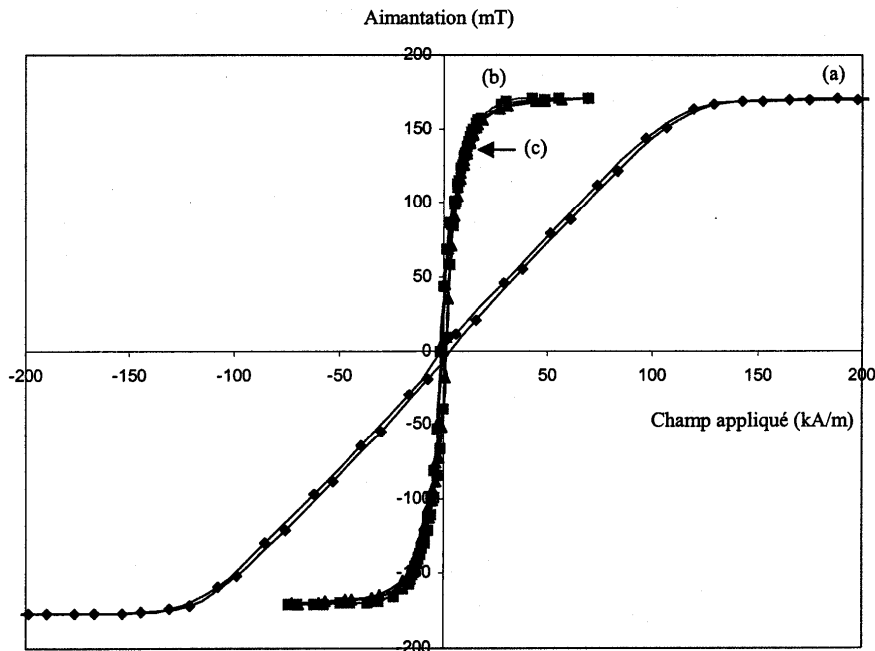


Figure 3.2 Example of magnetic hysteresis curves of YIG films on dielectric substrate deposited by magnetron sputtering at LT2C, (a) field applied out of the plane of the film, (b, c) field applied in the plane of the film

Its physical properties are: $\epsilon_r=15.4$, $\mu_0 M_s=180\text{mT}$, $\Delta H=1.6 \text{ kA/m}$ ($\pm 20\%$), conductivity of 0.01 S/m, Lande factor=2, $\tan\delta < 2.10^{-4}$, Curie temperature $280^\circ C$. Although the coercitivity is not given by TEMEX [10], we can assume that it is closed to the one of massive YIG that is around a few kA/m.

This sintered ceramic is very brittle and presents, as is, high roughness with a $R_a = 0.4 \mu\text{m}$, R_a being the arithmetic average of the absolute values with respect to the mean line of the profile. Moreover it's somewhat porous as testifies the random presence of some holes, a few μm deep. This high roughness proved to be hardly compatible with the technology to be implemented (generation of cracks and irregularities, that may generate electrical defects) and called for the introduction of an advanced-level polishing of the surface. We used the polisher MECAPOL P300.

1, Coarse polishing

Polishing is first a driving with emery paper P400 (grain size $35 \mu\text{m}$) and then with P1200 (grain size $15 \mu\text{m}$) until the scratches completely disappear. During polishing, the sample is refrigerated by water, the time for each polishing cycle is 15 minutes. The surface of the YIG substrate is checked regularly, and if some scratches are still present, the process goes on. This process usually takes 2 to 3 days.

2, Mirror polishing

The YIG substrate is polished using a diamond paste and felt disk (grain size $3 \mu\text{m}$ and $0.1 \mu\text{m}$) and an oil cooling. The time for each polishing cycle is 3 minutes. Between 2 cycles, the YIG film needs to be refrigerated by water, to avoid exceeding heating. The surface of the YIG substrate is checked using an optical microscope or a mechanical profilometer. This process also takes 2 to 3 days. A sketch of the polisher is shown in Figure 3.1.

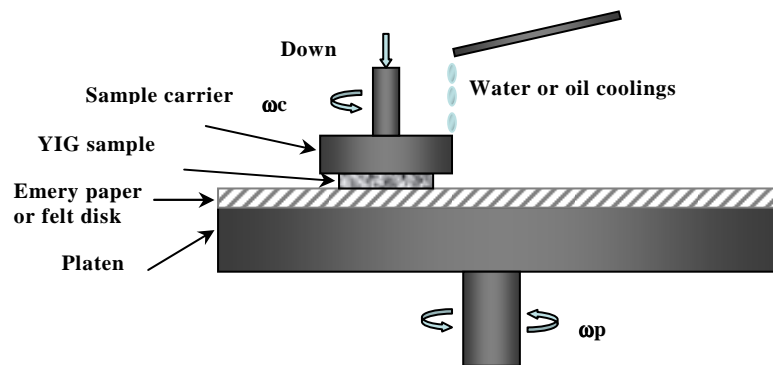


Figure 3.1 Working principle of the mechanical polisher (MECALPOL P300)

After polishing, we obtain for R_a : $R_a \approx 3\text{-}5 \text{ nm}$ which is comparable to the roughness of the alumina substrates and enables a reliable processing of the components.

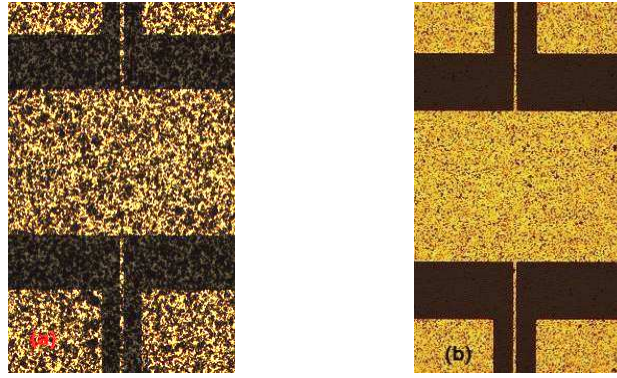


Figure 3.2 Comparison of coplanar structures processed on YIG substrate, (a) unpolished, (b) polished

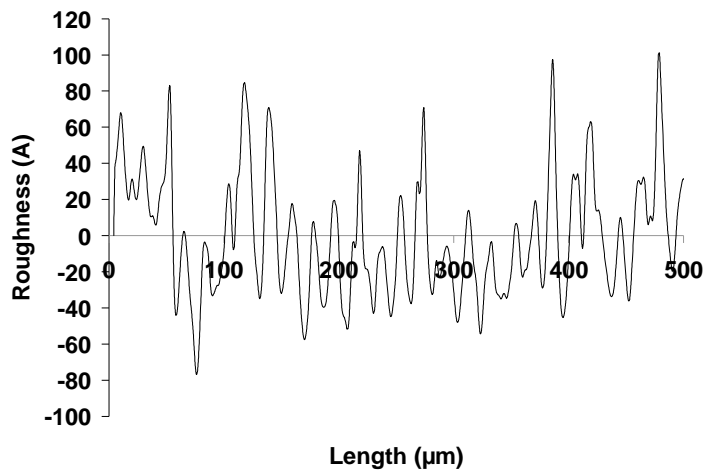


Figure 3.3 The surface roughness of the YIG substrate after polish

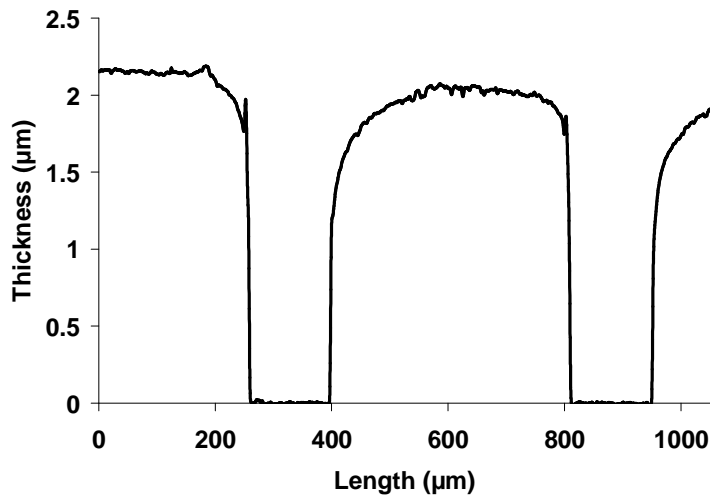


Figure 3.4 The measured thickness of conductor of a CPW (electrodeposited copper)

After the polishing has been done, the prototypes are processed in NANOLYON. The same photolithography technique and evaporation processes as indicated in Section 2.2 are used for fabrication.

After deposition of metal layer, the measured thickness of conductor is shown in Figure 3.4, the thickness of the conductor is about 2.1 μm . Some pictures of prototypes such as the shunt inductor, gap capacitors, a part of composite right/left-handed transmission are shown in Figure 3.5.

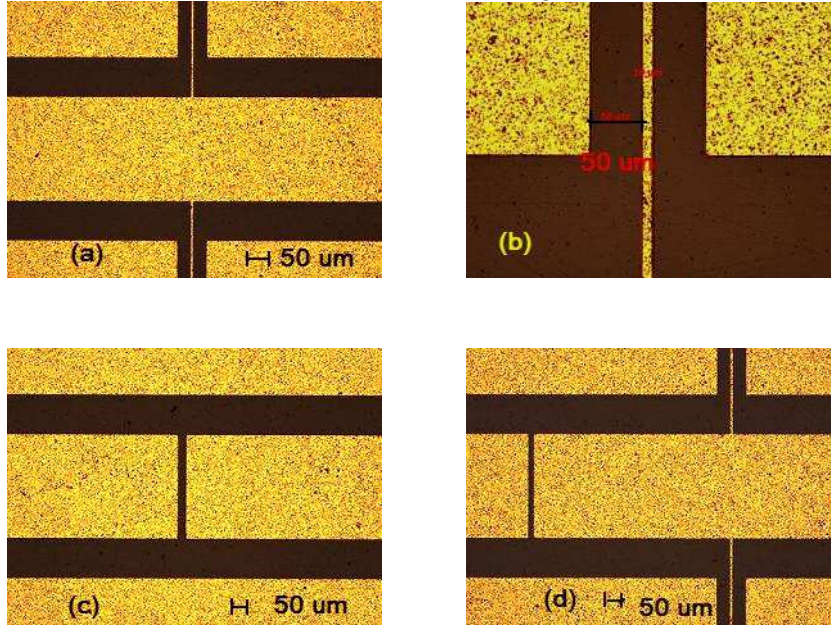


Figure 3.5 Optical micrographs of CPW components processed on YIG, (a) shunt inductor, (b) a part of shunt inductor, (c) gap capacitors, (d) a part of CRLH (gap capacitors and inductor)

3.4 Modelling and simulation

3.4.1 Modelling of ferrite material

For a homogeneous isotropic and linear magnetic medium, in the SI system (meter, kilogram, second, ampere), the response of a material immersed in an applied field \vec{H} , in terms of magnetization \vec{M} and magnetic induction \vec{B} is given by:

$$\chi \vec{H} = \vec{M} = \frac{d\vec{m}}{dV} \quad (3.1)$$

$$\vec{B} = \mu_0(\vec{H} + \vec{M}) = \mu_0 \vec{H}(1 + \chi) = \mu_0 \mu_r \vec{H} \quad (3.2)$$

where χ , dimensionless scalar, is the susceptibility, \vec{m} the sum of magnetic moments inside a given volume V . μ_r , dimensionless, represents the relative permeability and μ in (H/m) the absolute permeability ($\mu = \mu_0 \mu_r$). For nonmagnetic materials the relative permeability μ_r is one and χ vanishes. For anisotropic materials, the magnetization \vec{M} , the induction \vec{B} , and the applied field \vec{H} are not parallel, as a consequence the susceptibility χ and the permeability μ_r are become tensorial.

Note that in the CGS units (centimetre, gram, second) $\mu_0 = 1$ and

$$\vec{B} = \vec{H} + 4\pi\vec{M} \quad (3.3)$$

The conversion between CGS and SI units is shown in Table 3.2.

	Symbol	SI units	CGS units
Magnetic flux	ψ	1 Wb	10^8 Maxwell
Magnetic induction	\vec{B}	1 T = 1 Wb/m ²	10^4 Gauss
Magnetic field	\vec{H}	1 A/m	$4\pi \times 10^{-3}$ Oe
Magnetization	\vec{M}	1 Wb/m ²	2500 / π Gauss

Table 3.2 Conversion between CGS and SI units

3.4.1.1 Static magnetic field

When a static magnetic field \vec{H}_0 is applied to a ferrite material (epsilon 15.4), as shown in Figure 3.6b(a), its magnetic moments \vec{m} and the corresponding magnetization \vec{M} precess around the field axis with an angular velocity proportional to the magnitude of the applied field \vec{H}_0 [5]. This phenomenon is called Larmor's precession. Its gyromagnetic equation of motion, angular velocity, and gyromagnetic ratio are given below

$$\frac{d\vec{m}}{dt} = -\gamma\mu_0(\vec{m} \times \vec{H}_0) \quad (3.4)$$

$$\omega_0 = \gamma\mu_0 H_0 \quad (3.5)$$

$$\gamma = 176 \cdot 10^9 \text{ rad s}^{-1} \text{ T}^{-1} \quad (3.6)$$

or in term of frequency $\mu_0\gamma = 28\text{GHz}/T$

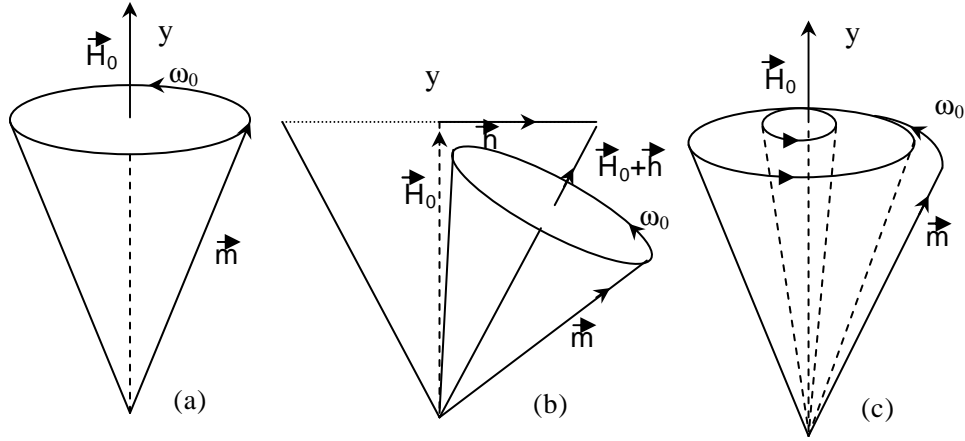


Figure 3.6 Precession of ferrite moments, (a) with a static applied field \vec{H}_0 , (b) with static field \vec{H}_0 and microwave applied field \vec{h} , (c) with losses

3.4.1.2 Static magnetic field with microwave field

When an additional microwave field \vec{h} , perpendicular to the static applied field \vec{H}_0 , is applied to the ferrite material, as shown in Figure 3.6(b), the magnetic moments m precess around the oscillating total field $\vec{H}_0 + \vec{h}$. When the angular velocity of the magnetic moments m and the frequency of microwave oscillation coincide, the microwave energy is transmitted to the ferrite material and absorbed: that is the gyroresonance phenomenon. Note that if losses are taken into account (Figure 3.6 (c)), the angle between m and \vec{H}_0 decreases until m and \vec{H}_0 are aligned.

Globally, according to Polder's model, for a saturated magnetic material, for a field \vec{H}_0 applied in the y-direction, if the losses are taking into account the relative permeability tensor can be written as:

$$\underline{\underline{\mu}}_r = \begin{bmatrix} \mu_r & 0 & j\kappa \\ 0 & 1 & 0 \\ -j\kappa & 0 & \mu_r \end{bmatrix} \quad (3.7)$$

where the elements of the permeability tensor are frequency – dependent complex quantities:

$$\mu_r = \mu' - j\mu'' = 1 + \frac{(\omega_0 + j\alpha\omega)\omega_M}{(\omega_0 + j\alpha\omega)^2 - \omega^2} \quad (3.8)$$

$$\kappa = \kappa' - j\kappa'' = \frac{\omega\omega_M}{(\omega_0 + j\alpha\omega)^2 - \omega^2} \quad (3.9)$$

$$\omega_M = \gamma\mu_0 M_S \quad (3.10)$$

M_S is the saturation magnetization of the ferrite material and α is damping factor. Note that the tensor elements depend on the static field \vec{H}_0 through ω_0 and on the saturation magnetization through ω_m .

As an illustration, real and imaginary parts of the elements of the permeability tensor of YIG as a function of a frequency for an applied field $\vec{H}_0 = 140$ kA/m is shown in Figure 3.7. These elements are given as a functions of the applied field \vec{H}_0 at 5 GHz in Figure 3.8. The damping factor is taken equal to 0.1, and the saturation magnetization equals to 180 mT. Note that comparable dependencies are obtained the permeability tensor of BaM.

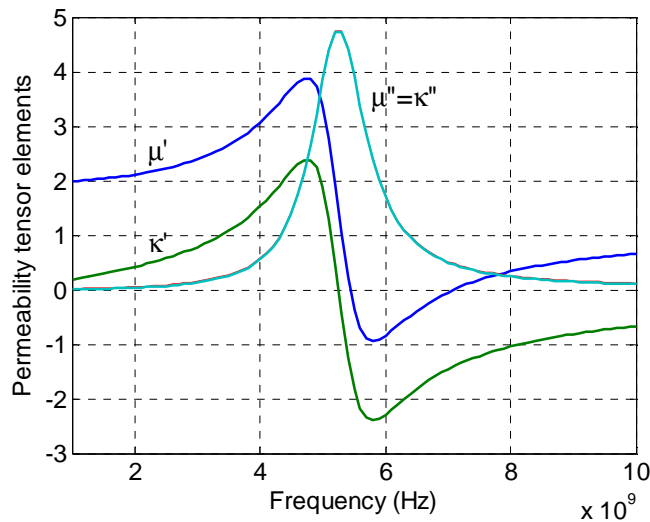


Figure 3.7 Real and imaginary parts of the elements of the permeability tensor for an applied field $\vec{H}_0 = 140$ kA/m as a function of the frequency for YIG

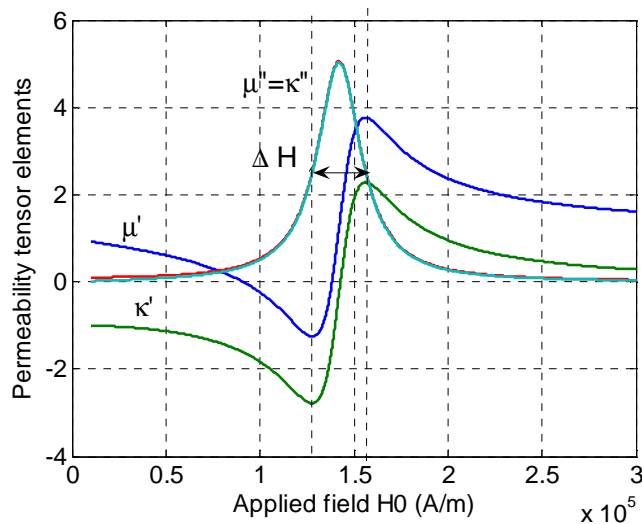


Figure 3.8 Real and imaginary parts of the elements of the permeability tensor at 5 GHz as a function of the applied static field \vec{H}_0 for YIG

3.4.1.3 Linewidth ΔH

The resonance loss is characterized by the width of the imaginary part of μ_r and κ . The linewidth at midheight (see Figure 3.8) depends on the damping factor α and operation frequency according to:

$$\gamma \mu_0 \Delta H = 2 \alpha \omega \quad (3.11)$$

ΔH increases for lossy materials.

3.4.1.4 Demagnetizing factors

All the previous definitions assume the magnetic material influenced by the internal magnetic field, which is experienced by the spin dipoles. In an infinite material, the internal field equals the applied field, but in a finite material, a discontinuity of the magnetic field exists at the boundary between materials having different permeabilities. For a material having an approximate ellipsoidal shape, the internal field \vec{H}_i can be expressed as

$$\vec{H}_i = \vec{H}_0 - \vec{N} \vec{M} \quad (3.12)$$

where

$$\vec{N} = \begin{pmatrix} N_x & 0 & 0 \\ 0 & N_y & 0 \\ 0 & 0 & N_z \end{pmatrix} \quad (3.13)$$

The demagnetizing factors N_x , N_y , and N_z are determined by the sample shape, as shown in Table 3.2, the sum of the terms are equal to 1: $N_x + N_y + N_z = 1$.

Sample shape	N_x	N_y	N_z	Sum
Sphere	1/3	1/3	1/3	1
Thin film (y-z plane)	1	0	0	1
Thin film (x-z plane)	0	1	0	1
Thin film (x-y plane)	0	0	1	1

Table 3.2 The demagnetizing factors as a function of the sample shape

The demagnetizing factors concern the static and the microwave field, the corresponding tensor elements are changed, and the resonance angular frequency is given by Kittel's equation for a applied field in y-direction:

$$\omega_r = \gamma \mu_0 H_i = \gamma \mu_0 \sqrt{[H_0 + H_a + (N_x - N_y)M][H_0 + H_a + (N_z - N_y)M]} \quad (3.14)$$

where H_a is the anisotropy field (for YIG $H_a = 0\text{T}$, for BaM $H_a = 1.7\text{T}$)

3.4.1.5 Nonreciprocal wave propagation

In a infinite medium, for a harmonic wave propagating along the direction z , Maxwell-Faraday and Maxwell-Ampere relationships if combined lead to the following differential equation fulfilled by both the electric field \vec{E} and magnetic field \vec{H} ,

$$\overrightarrow{\text{rot}}(\overrightarrow{\text{rot}}\vec{H}) = \omega^2 \mu_0 \varepsilon_0 \varepsilon_r \overline{\mu} \times \vec{E} \quad (3.15)$$

$$\overrightarrow{\text{rot}}(\overrightarrow{\text{rot}}\vec{E}) = \omega^2 \mu_0 \varepsilon_0 \varepsilon_r \overline{\mu} \times \vec{H} \quad (3.16)$$

And the propagation constant γ is given by:

$$\gamma = \alpha + j\beta = j \frac{\omega}{c} \sqrt{\varepsilon_e \mu_e} \quad (3.17)$$

where ε_e and μ_e are effective permittivity and permeability respectively.

Applied static field \vec{H}_0 parallel to the propagation direction

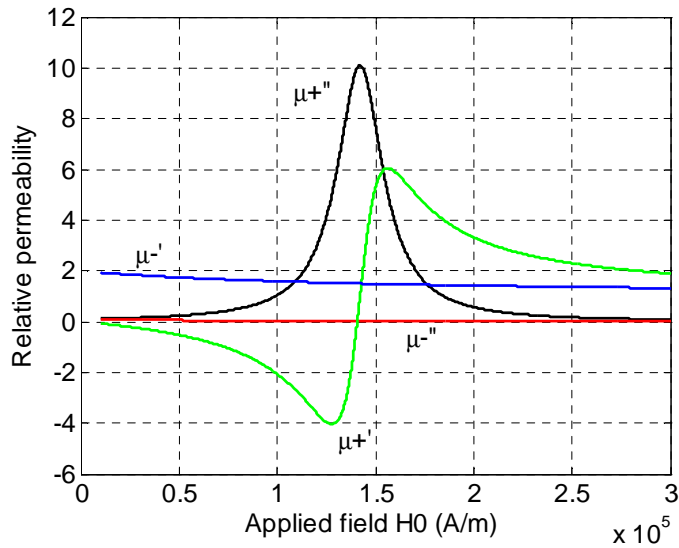


Figure 3.9 Effective permeability as a function of the applied static field \vec{H}_0 , (configuration of a field applied parallel to the direction of propagation)

In an infinite medium, if the applied field is parallel to the propagation direction, the effective permeability can take 2 values:

$$\mu_+ = \mu_r + \kappa \quad (3.18)$$

$$\mu_- = \mu_r - \kappa \quad (3.19)$$

depending if the polarization of the field is circular right or left. The dependence of their real and imaginary parts is shown in Figure 3.9.

The corresponding propagation constant of a plane wave is given by:

$$\gamma_+ = j \frac{\omega}{c} \sqrt{\epsilon_r \mu_+} = j \frac{\omega}{c} \sqrt{\epsilon_r (\mu_r + \kappa)} \quad (3.20)$$

$$\gamma_- = j \frac{\omega}{c} \sqrt{\epsilon_r \mu_-} = j \frac{\omega}{c} \sqrt{\epsilon_r (\mu_r - \kappa)} \quad (3.21)$$

The corresponding attenuation constant α and phase constant β are depicted in Figure 3.10 as a function of the applied static field \vec{H}_0 (as $\gamma = \alpha + j\beta$):

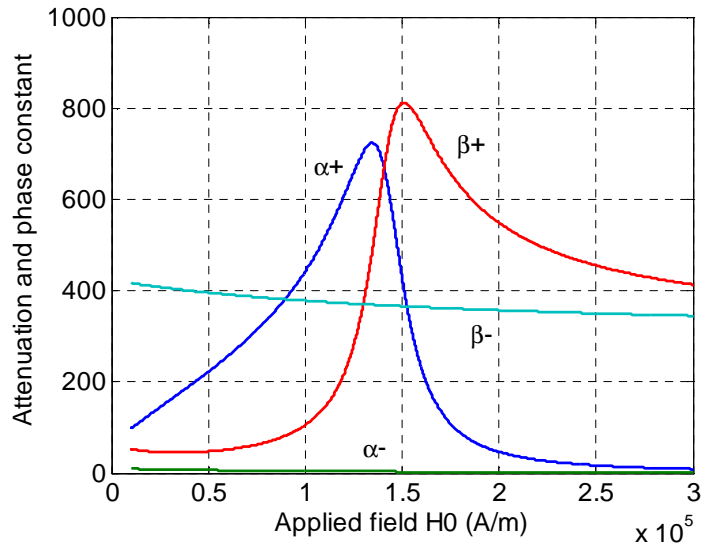


Figure 3.10 Nonreciprocal attenuation (Np/m) and phase constants (rad/m) as a function of the applied static field \vec{H}_0 , (configuration of a field applied parallel to the direction of propagation)

This configuration is implemented for the Faraday rotation, which induces the rotation of the polarization of a linearly polarized incident microwave field.

Applied static field \vec{H}_0 perpendicular to the propagation direction

If the applied field is perpendicular to the propagation direction, propagation occurs according to 2 effective permeability values:

$$\mu_+ = \frac{\mu_r^2 - \kappa^2}{\mu_r} \quad (3.23)$$

$$\mu_- = 1 \tag{3.24}$$

as shown in Figure 3.11.

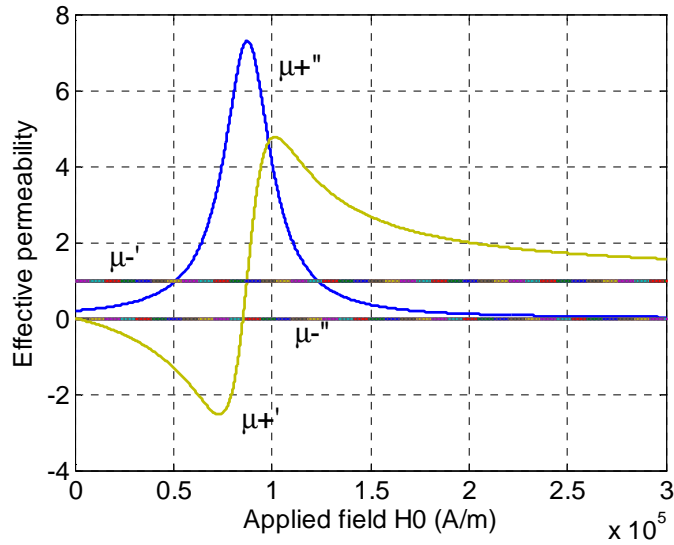


Figure 3.11 Effective permeability as a function of the applied static field \vec{H}_0 , (configuration of a field applied perpendicular to the direction of propagation)

The corresponding propagation constants of plane wave are shown in Figure 3.12

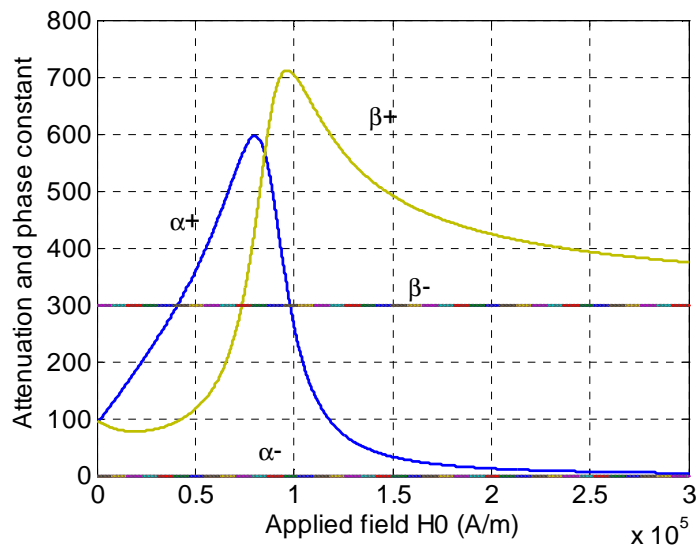


Figure 3.12 Nonreciprocal attenuation (Np/m) and phase constants (rad/m) as a function of the applied static field \vec{H}_0 , (configuration of a field applied perpendicular to the direction of propagation)

3.4.2 Finite element simulation

The same software COMSOL is used to make simulation, as shown in Section 2.3. The same steps in the modelling process are shown below:

- *Defining the geometry*: this step is identical to the one of Section 2.3
- *Meshing*: For the ‘Free mesh parameters – Global’, we chose ‘Coarser’ as ‘Predefined mesh sizes’. For the ‘Free mesh parameters – Boundary’, we chose ‘Triangle’ as ‘Boundary mesh parameters – Method’. Then we mesh the whole component.
- *Specifying the physics*: the same as indicated in Section 2.3 except that, the permittivity of subdomain YIG should be defined as 15.4, and the permeability tensor of YIG should be defined as in Equation 3.4 to Equation 3.14.
- *Solving*: the same as shown in Section 2.3
- *Visualizing simulated results*: the same as shown in Section 2.3

Several geometries of CPW components on YIG in COMSOL are shown in figures below.

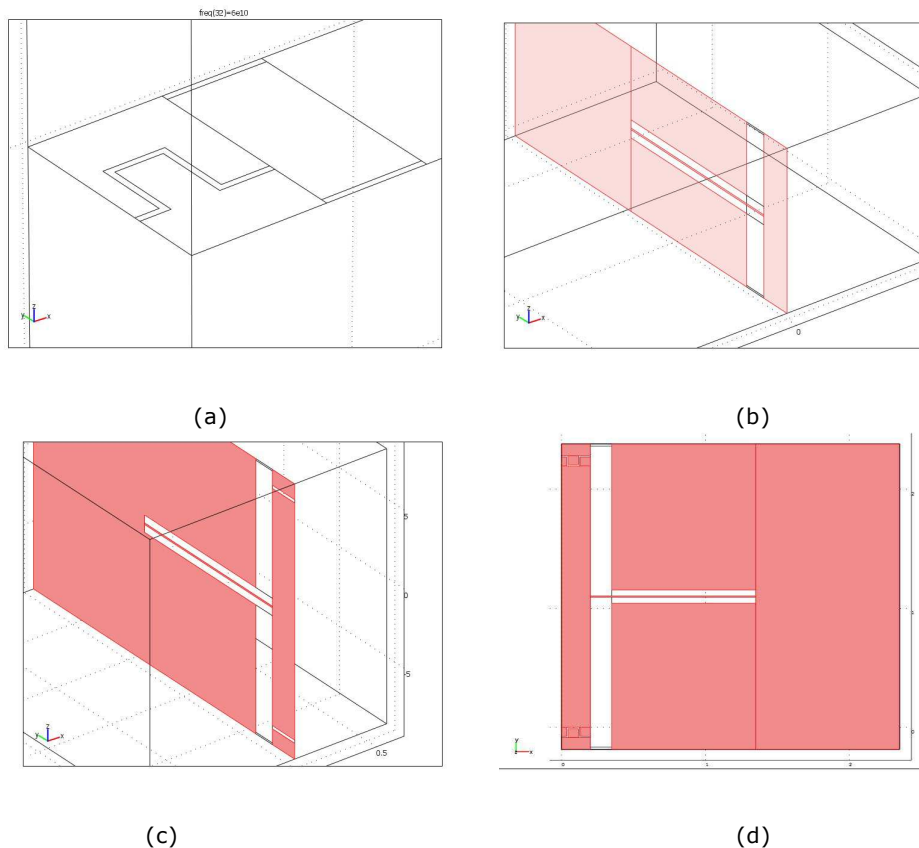


Figure 3.13 Geometries of components on YIG, (a) Interdigital capacitor, (b) Shunt inductor, (c) Composite right/left-handed transmission line with straight capacitor, (d) Composite right/left-handed transmission line with IDC

3.4.3 Calculation of propagation constant (reciprocal network)

The measured and simulated ABCD matrix and S matrix can be used to extract the propagation constant. The ABCD matrix and S matrix of the CPW are shown in Figure 3.14.

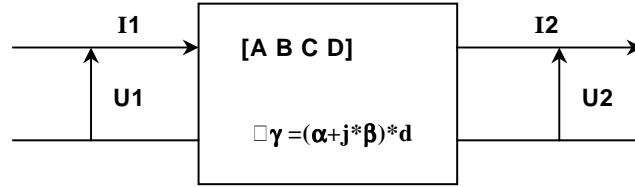


Figure 3.14 ABCD matrix and S matrix of a CPW

For a periodical network, the voltage and current relation between 2 ports can be written as [2]:

$$\begin{bmatrix} U1 \\ I1 \end{bmatrix} = \begin{bmatrix} e^{\gamma^*d} & 0 \\ 0 & e^{\gamma^*d} \end{bmatrix} \begin{bmatrix} U2 \\ I2 \end{bmatrix} = \begin{bmatrix} A & B \\ C & D \end{bmatrix} \begin{bmatrix} U2 \\ I2 \end{bmatrix} \quad (3.24)$$

For a lossless network ($\alpha=0$), γd is the phase delay due to a finite propagation time. The second equality can be expressed as:

$$\begin{bmatrix} e^{\gamma^*d} & 0 \\ 0 & e^{\gamma^*d} \end{bmatrix} \begin{bmatrix} U2 \\ I2 \end{bmatrix} - \begin{bmatrix} A & B \\ C & D \end{bmatrix} \begin{bmatrix} U2 \\ I2 \end{bmatrix} = 0 \quad (3.25)$$

That implies:

$$\begin{bmatrix} e^{\gamma^*d} & 0 \\ 0 & e^{\gamma^*d} \end{bmatrix} - \begin{bmatrix} A & B \\ C & D \end{bmatrix} = 0 \quad (3.26)$$

$$\begin{bmatrix} e^{\gamma^*d} - A & -B \\ C & e^{\gamma^*d} - D \end{bmatrix} = 0 \quad (3.27)$$

The determinant of the above matrix can be written as:

$$(e^{\gamma^*d} - A) \cdot (e^{\gamma^*d} - D) - B \cdot C = 0 \quad (3.28)$$

$$e^{2\gamma^*d} - (A + D) \cdot e^{\gamma^*d} + (A \cdot D - B \cdot C) = 0 \quad (3.29)$$

The solution of the above equation as a function of the ABCD parameter form is:

$$e^{\gamma^*d} = \frac{(A + D) \pm \sqrt{(A + D)^2 - 4(A \cdot D - B \cdot C)}}{2} \quad (3.30)$$

For a well matched network

$$A = \frac{1 - S_{22} + S_{11} - \Delta S}{2S_{21}} \quad (3.31)$$

$$B = \frac{1 + S_{22} + S_{11} + \Delta S}{2S_{21}} \times Z_c \quad (3.32)$$

$$C = \frac{1 - S_{22} - S_{11} + \Delta S}{2S_{21}Z_c} \quad (3.33)$$

$$D = \frac{1 + S_{22} - S_{11} - \Delta S}{2S_{21}} \quad (3.34)$$

Where

$$\Delta S = S_{11}S_{22} - S_{12}S_{21} \quad (3.35)$$

$$A \cdot D - B \cdot C = \frac{S_{12}}{S_{21}} \quad (3.36)$$

$$\frac{A + D}{2} = \frac{1 - \Delta S}{2S_{21}} \quad (3.37)$$

We can get the S parameters form of the solution of equation

$$e^{\gamma^*d} = \frac{1 - \Delta S}{2S_{21}} \pm \frac{\sqrt{\left(\frac{1 - \Delta S}{S_{21}}\right)^2 - 4\frac{S_{12}}{S_{21}}}}{2} \quad (3.38)$$

$$e^{\gamma^*d} = \frac{1 - \Delta S}{2S_{21}} \pm \sqrt{\left(\frac{1 - \Delta S}{2S_{21}}\right)^2 - \frac{4S_{12}}{4S_{21}}} \quad (3.39)$$

$$e^{\gamma^*d} = \frac{1 - \Delta S}{2S_{21}} \pm \frac{\sqrt{(1 - \Delta S)^2 - 4S_{12}S_{21}}}{2S_{21}} \quad (3.40)$$

$$e^{\gamma^*d} = \frac{(1 - \Delta S) \pm \sqrt{(1 - \Delta S)^2 - 4S_{12}S_{21}}}{2S_{21}} \quad (3.41)$$

$$e^{\gamma^*d} = [(1 - \Delta S) \pm \sqrt{(1 - \Delta S)^2 - 4S_{12}S_{21}}] / (2S_{21}) \quad (3.42)$$

$$\gamma^*d = \ln[[(1 - \Delta S) \pm \sqrt{(1 - \Delta S)^2 - 4S_{12}S_{21}}] / (2S_{21})] \quad (3.43)$$

3.5 Results of coplanar components on ferrite

As finite element simulations were implemented for the first at INL in the frame work of this Ph.D thesis, we simulated CPW patterned on 2 types of ferrite:

- First CPW patterned on a film of BaM: this study made a transition with the proceeding works.
- Then CPW patterned on a thick commercial YIG substrate (1mm).

These samples were realized in the frame work of the present study. YIG was preferred due to its gyroresonance frequency of a few GHz, much better adapted to our goals than that of BaM which is too high.

3.5.1 CPW on ferrite barium hexaferrite

As a kind of ferrite materials, the barium hexaferrite ($\text{BaFe}_{12}\text{O}_{19}$ or BaM) has a strong uniaxial anisotropy and a high gyroresonance frequency (50 GHz). It can operate without a permanent magnet and has potential applications in the field of microwave and millimetre-wave passive components. A CPW integrating a BaM film is shown in Figure 3.15. The BaM thin films considered here are deposited by radio frequency sputtering system as detailed in papers [11-12]. Their thicknesses can reach $20\ \mu\text{m}$. One method for ferrite thin film characterization in the microwave range has been proposed by D. Vincent [13-14].

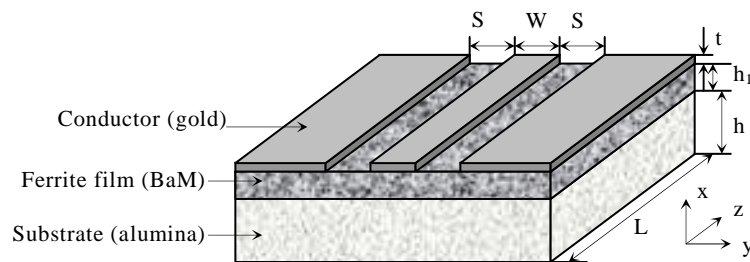


Figure 3.15 Geometry of CPW with integrated barium ferrite thin film (prototype).

$$W=72\ \mu\text{m}, S=40\ \mu\text{m}, h=635\ \mu\text{m}, h_1= 20\ \mu\text{m}.$$

In the following, such CPWs are studied and two different magnetic polarizations considered. First the H-polarizing field is out-of-the plane (x-direction), and then the H-polarizing field in the plane (y-direction) of the CPW. All measurements are done at the remanence, without external magnetic field.

3.5.1.1 Remanent field out of the plane of the CPW - filter

The experimental and simulated transmission coefficients of this CPW are shown in Figure 3.16. In this configuration, the transmission parameters S_{21} and S_{12} are equal as the device is reciprocal. The results obtained previously for a CPW directly on an alumina substrate are also reported, making the comparison easier. When reaching the gyromagnetic frequency (48 GHz), the signal is strongly absorbed by the ferrite material and a strong attenuation is observed ($S_{12} = 1.85\ \text{dB/mm}$).

The simulated results are quite close to the measured ones. The simulated results are obtained with the following magnetic film properties: saturation magnetization 0.48 T, ΔH 400kA/m, relative permittivity 14.2 and uniaxial anisotropy 1.7 T (1360 kA/m). In the whole frequency band, the losses of the CPW with ferrite film are slightly higher (0.1-0.2dB/mm) than the losses of the one without BaM film due to magnetic losses. Globally, a band-stop filter is achieved, which centre frequency is the gyro-resonance frequency and which bandwidth is directly linked to ΔH .

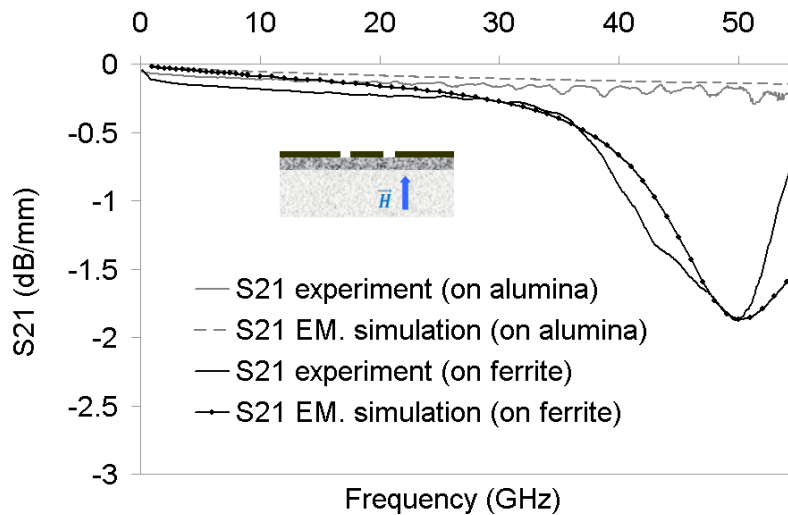


Figure 3.16 Transmission coefficients of CPW with integrated BaM thin film (remanent magnetization x-direction)

3.5.1.2 Remanent field in the plane of the CPW - isolator

A CPW with BaM thin film can also be used for developing nonreciprocal components, such as isolators and circulators which are among the important microwave components. With the same structure as the one presented in section 3.5.1.1, for studying the nonreciprocal properties of CPW with BaM thin film, the applied field is set in the film plane and perpendicular to the direction of propagation (y direction).

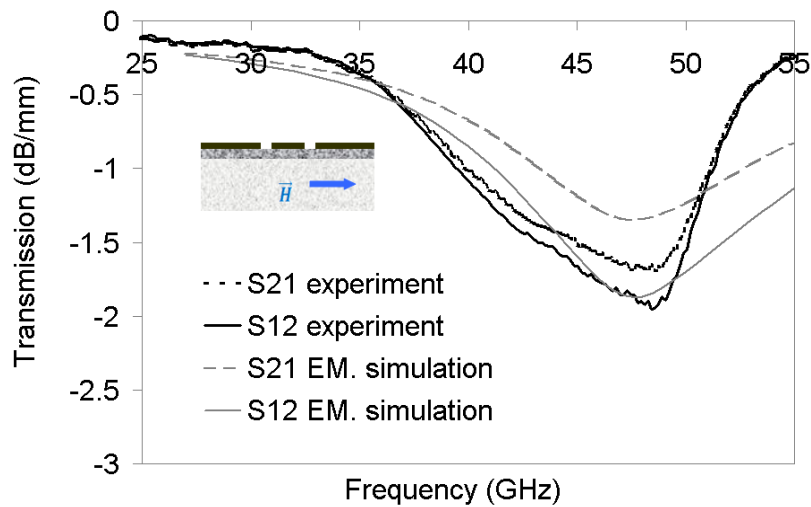


Figure 3.17 Transmission coefficients of CPW with integrated BaM thin film (remanent magnetization y-direction)

The experimental and simulated transmission coefficients of this CPW are plotted in Figure 3.17 and the influence of changing the direction of the applied field is observed. Approximately 1.6 dB/mm transmission parameter and 0.3 dB/mm nonreciprocal effects are achieved without external magnetic field. These results show that this structure could work as an isolator if the transmission parameters were improved.

3.5.2 CPW on ferrite YIG without applied field (sample 4, 17)

Yttrium iron Garnet (YIG) has a weak saturation magnetization (around 180mT), it can be easily saturated, it is used in microwave and millimetre wave like isolators, circulators, and filters [13-15], it can be used also in Faraday rotators and other magneto-optical applications. In our work, the properties of CPW on substrate YIG with or without applied field will be given; the non-reciprocity will also be studied. The transversal of CPW on substrate YIG is shown in Figure 3.18.

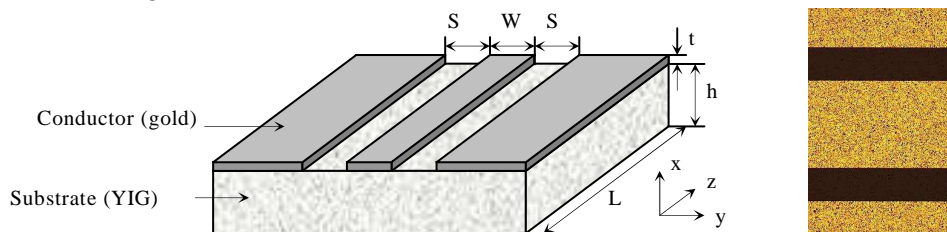


Figure 3.18 Geometry of CPW on YIG thin film (prototype).

$W=400 \mu\text{m}$, $S=150 \mu\text{m}$, $h=3*900 \mu\text{m}$, $t=1 \mu\text{m}$, $L=10 \text{mm}$

3.5.2.1 S parameters

The CPW on YIG without applied field is measured in NANOLYON and LT2C [19]. The measured and simulated S parameters are shown in Figure 3.19. Without any applied field, it's a reciprocal microwave component: S_{11} equals to S_{22} and S_{12} equals S_{21} . Still we observe a small gyroresonance around 1.4 GHz, which according equation 3.14, corresponds to a small magnetic field of about 32 mT (25.6 kA/m). As the sample was measured several times, the magnetization follows the hysteresis cycle and this field could originated from the remanent magnetization as well as from spin resonance. On the other hand, the simulated parameters are calculated assuming no applied field. So we do not observe any gyroresonance on the simulated curve.

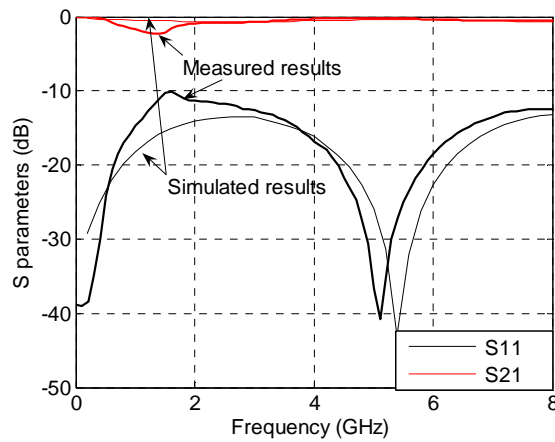


Figure 3.19 Measured S parameters of CPW on YIG without applied field

3.5.2.2 Propagation constant

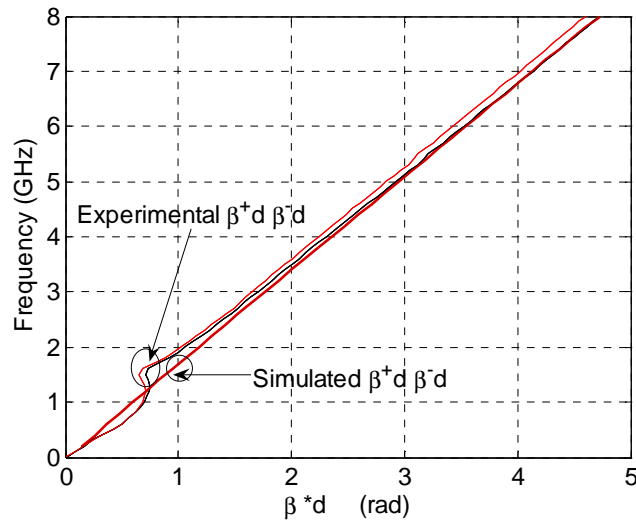


Figure 3.20 Experimental and simulated propagation constants of CPW on YIG without applied field

The calculation method presented in Section 3.4 is used to extract the propagation constants. The calculated propagation constants of CPW are shown in Figure 3.20 (α is neglected), the β in the forward and backward directions are almost the same as expected.

3.5.3 CPW on YIG with applied field in the plane

Now a static magnetic field is applied in the y -direction, see Figure 3.21. Its properties are described by R.Marques, I.V.Lindell and M.Horno [16-18]. The samples were measured with the applied field excited by electromagnet at LT2C, the measured centre applied field and border applied field are shown in Table 3.3.

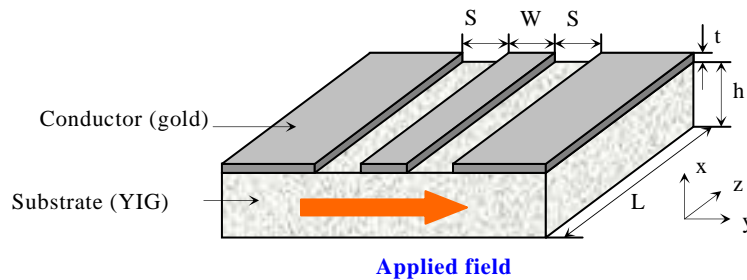


Figure 3.21 Orientation of the applied field for the CPW on YIG.

Center Applied Field (mT)	Border Applied Field (mT)	Center AF / Border AF
-215	-145	1.48
-216	-141	1.53
-192	-126	1.52
-170	-110	1.55
-67	-44	1.52
-44	-29	1.52
14.8	10.1	1.46
45.4	30.2	1.50
71	48	1.47
143	96	1.48
170	113	1.50
185	126	1.46
215	135	1.59

Table 3.3 The measured center applied field and border applied field. The border field is measured 1cm away from the center in the y-direction.

In the following, we will consider that the centre applied field is the field seen from the sample.

3.5.3.1 *S* parameters

To evaluate the non-reciprocity of CPW on YIG with applied field, we made a series of measurements. The measured *S* parameters with applied field are shown in Figure 3.22 and Figure 3.23. The gyromagnetic resonance frequency increases with the applied field: for an increase of the applied field from 46 mT to 166 mT, the gyromagnetic resonance frequency increases from 2 GHz to 6 GHz, which is expected from the Equation 3.14. The difference between S_{12} and S_{21} increases from 0.8 dB to 6 dB, which improve the nonreciprocity of CPW on YIG. This is related to the dependency of the elements of the permeability tensor on the applied field and frequency, see equations 3.7 to 3.10. The measured results and simulated *S* parameter of a CPW on YIG with an applied field of 140 kA/m are shown Figure 3.24 (YIG saturated), the simulated results show the gyroresonance peak and the nonreciprocity, however, with a small shift in the gyroresonance frequency.

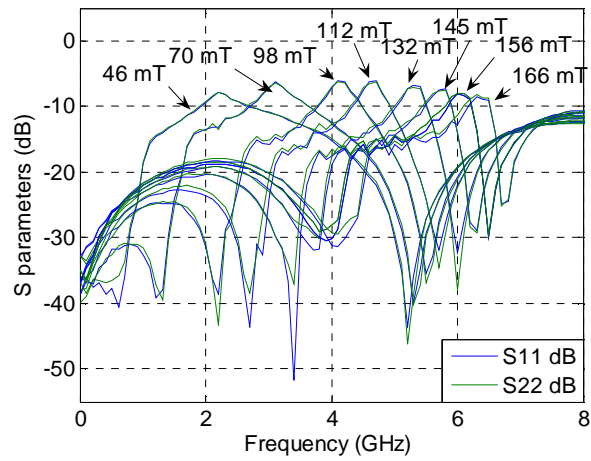


Figure 3.22 Measured S_{11} and S_{22} parameters of CPW on YIG with applied field

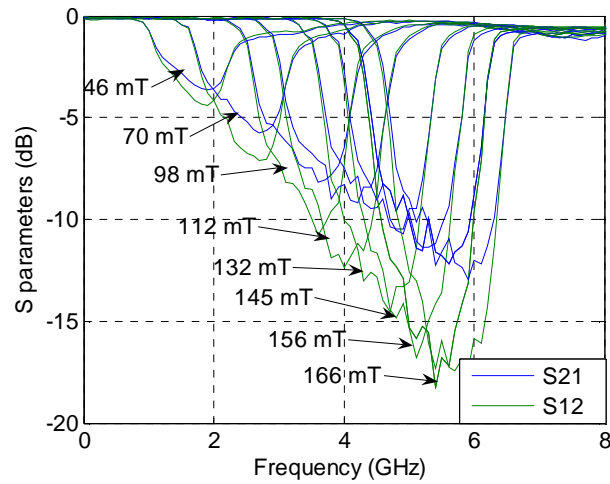


Figure 3.23 Measured S_{21} and S_{12} parameters of CPW on YIG with applied field

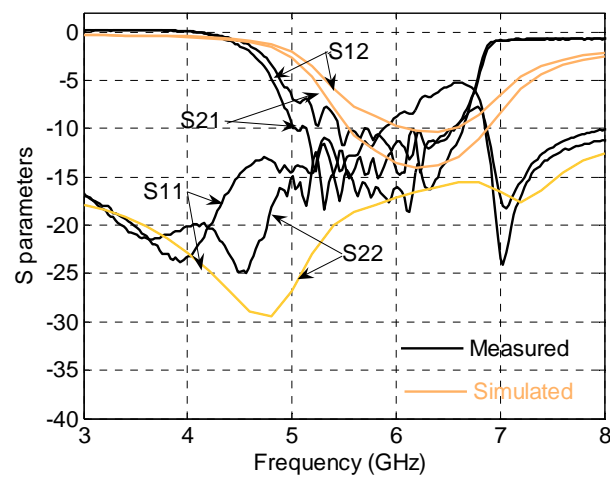


Figure 3.24 Comparison of measured and simulated S parameters, applied field 140KA/m, demagnetizing factor ($N_x=1/3$, $N_y=1/3, N_z=1/3$)

The relation between the applied field and the gyromagnetic resonance frequency, the applied field and the nonreciprocity are shown in Table 3.4.

Applied field (mT)	Gyromagnetic resonance frequency (GHz)	Nonreciprocity $S_{12} - S_{21}$ (dB)
46 mT	2.0	0.8
70 mT	2.7	1.5
98 mT	3.6	2.5
112 mT	4.0	3.5
132mT	4.8	4.0
145 mT	5.1	5.0
156 mT	5.5	6.0
166 mT	5.9	5.0

Table 3.4 Relationship between the measured applied field, gyromagnetic resonance frequencies, and non reciprocal effect.

3.5.3.2 Propagation constant

The extracted propagation constants with S parameters are shown in Figure 3.25 and Figure 3.26, it's indicated that the gyromagnetic resonance frequencies increase with the applied field, the frequency corresponding to the bend increase, when applied field increase from 46 mT to +66mT, the gyromagnetic resonance frequencies increase from about 2 GHz to 6 GHz, the difference between β_+ and β_- increase from 0.1 rad to 0.5 rad. The non-reciprocities of CPW on YIG increase with the applied field.

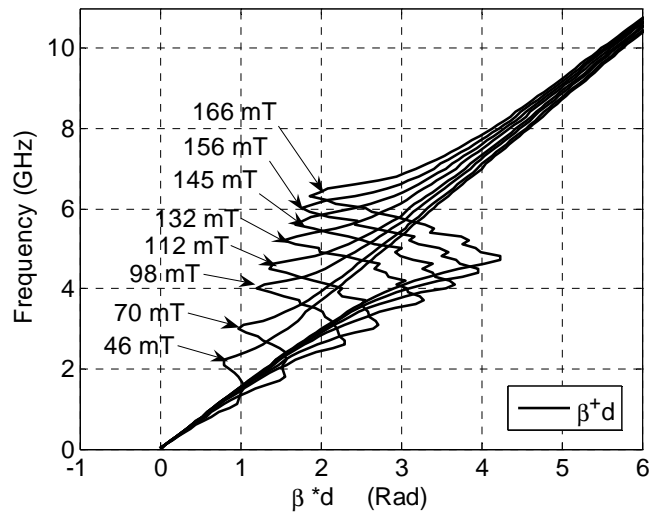


Figure 3.25 Dispersion relation on positive direction of CPW on YIG with applied field obtained from experimental data.

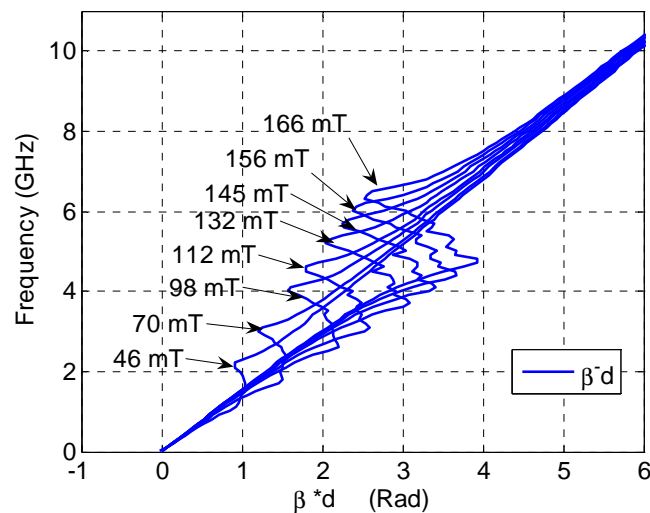


Figure 3.26 Dispersion relation on negative direction of CPW on YIG with applied field obtained from experimental data

In our work, the negative permeability as illustrated in Figure 3.7 of ferrite can be produced a left-handed behavior, in the frequency range, when the slope of the frequency as a fonction of βd is negative, as shown in Figure 3.25 and 3.26. In this frequency range, the phase velocity is positive, whereas the group velocity is negative. Note that this frequency range can be tuned by the polarizing magnetic field.

The graphs 3.25 and 3.26 are in agreement with the dispersion diagram calculated for ferrite by using equations 3.4 to 3.10. We have $\gamma = \alpha + j\beta = j\omega\sqrt{\mu_{eff}\epsilon_{eff}}$, where for simplicity $\epsilon_{eff} = (1 + \epsilon_{YIG})/2$ and μ_{eff} was assumed to be μ_r (Equation 3.8). The calculated dispersion diagram for the CPW on YIG, for low and for high losses are shown in Figures 3.27 and 3.28.

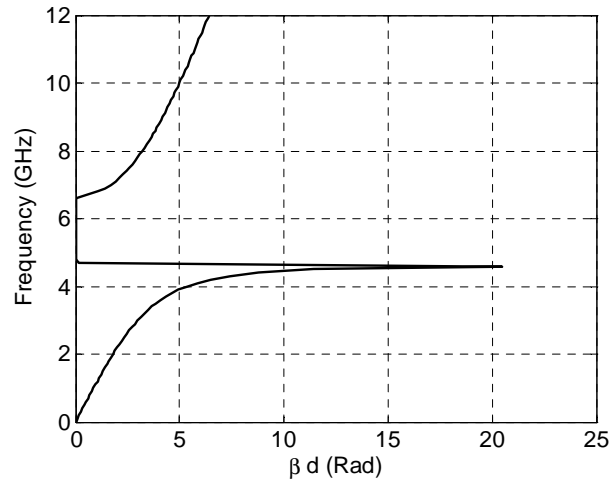


Figure 3.27 Calculated dispersion relation for low losses, applied field 166mT, saturation magnetization 175 mT, damping factor $\alpha = 0.00015$

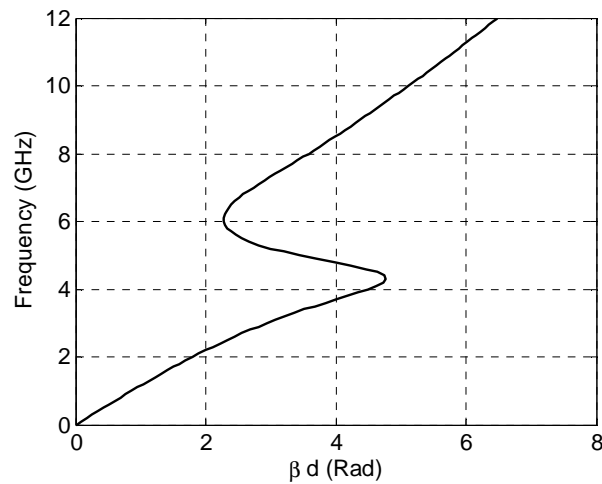


Figure 3.28 Calculated dispersion relation for high losses, applied field 166mT, saturation magnetization 175 mT, damping factor $\alpha = 0.15$

One notes that Figure 3.27 has a behavior similar to the figure reported by M. A. Abdalla et al. in [20] for the same type of component. However, our experimental dispersion curve is much smoother due to higher losses.

3.5.4 Coplanar gap capacitor on ferrite (sample 18-10 μm 22-30 μm 23-6 μm 24-20 μm)

As the capacitors have exactly the same geometry as capacitors on alumina, but YIG has a larger permittivity than alumina, we expected the capacitance to increase linearly for a gap capacitors, as shown in Equation 2.8. A CPW gap capacitor on YIG is shown in Figure 3.29, its equivalent circuit is shown in Figure 3.30, it consists of shunt capacitance C_p and series capacitance C_s . The finite element simulation approach mentioned in previous Section 2.3.1 can be used to evaluate the value of capacitor.

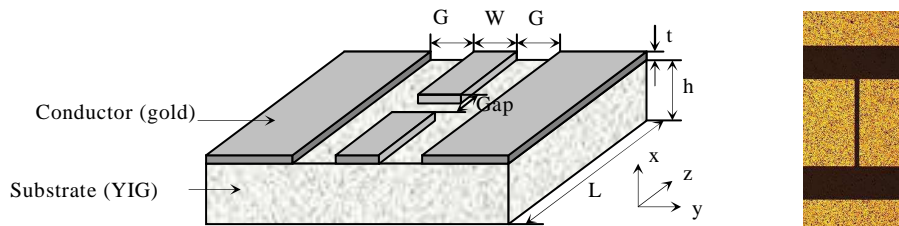


Figure 3.29 CPW gap capacitor on YIG, W - center conductor width, S - slot width, h - substrate height, t - conductor thickness, L - physical length, Gap - gap width.

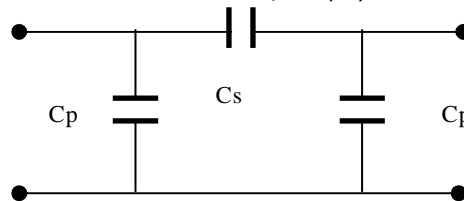


Figure 3.30 Equivalent circuit of CPW gap capacitor on YIG.

In our work, CPW gap capacitors on YIG with gap 6 μm , 10 μm , 20 μm and 30 μm are designed and fabricated, the capacitors dimensions are shown in Table 3.5.

Sample	Gap (μm)	t (μm)	Lrf (mm)
Capacitor1 (23)	6	1	4.995
Capacitor2 (18)	10	1	4.995
Capacitor3 (24)	20	1	4.99
Capacitor4 (22)	30	1	4.98

Table 3.5 Geometrical dimension of CPW gap capacitors on substrate alumina, W = 400 μm , G= 150 μm , h=900 μm . Lrf: the length of shifte reference plane.

3.5.4.1 Measured and simulated S parameters

Four gap capacitors with gap 6 μm , 10 μm , 20 μm , and 30 μm were implemented. The S parameters are given in Figure 3.31. The software COMSOL is

used to simulate the capacitors on YIG, for saving the solving time of simulation, the metal layer is replaced by perfect electronic conductor (PEC).

Here again, the gap capacitor work as a high pass microwave network, only high frequency signal can propagate in gap capacitor (Figure 3.31). The S_{21} parameter decreases with gap increases, for gap increase from 10 μm to 30 μm , the S_{21} parameters decrease from -14 dB to -19 dB at 6 GHz. Notice that the simulated results are different from measured results, that's because in simulation, the length of CPW connected to capacitor is defined as 100 μm , while in reality, the length of CPW on YIG connected to the capacitor is about 4900 μm , it has a contribution to the absorbed signal. Around the gyroresonance frequency, a part of power of electromagnetic wave is absorbed due to the gyroresonance, compared with a convention network without gyrosonance, like the one simulated. The corresponding transmission parameters S_{21} will decrease, according to Equation 3.41, the corresponding series capacitance C_s will decrease. That is what we observed in Figure 3.32.

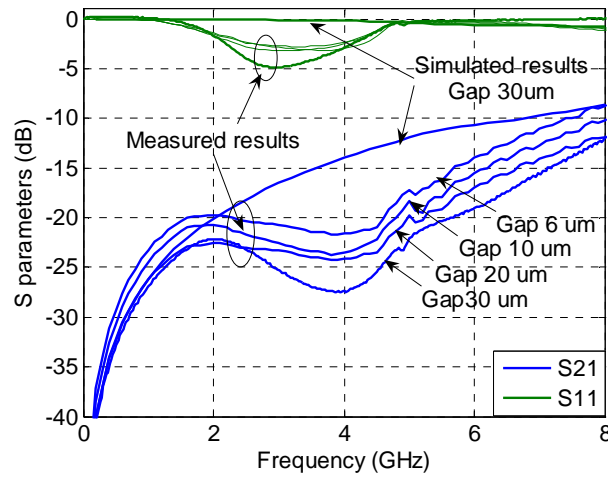


Figure 3.31 Measured and simulated S parameters of capacitors, with gap width 6 μm , 10 μm , 20 μm , and 30 μm . Simulated S parameters obtained on a 100 μm length sample without field, measured S parameters obtained on a 1cm length sample with some remanent field

3.5.4.2 Values of capacitors

As in Section 2.3.2.5, the capacitance can be extracted by ABCD parameters by using formulas giving below

$$C_s = \frac{1}{j\omega B \cdot Z_c} \quad (3.44)$$

$$C_p = (A - 1)C_s \quad (3.45)$$

Note that the S parameters used to extract capacitance values should take into account the shift of reference plane, according to the method presented in Section 2.4.1.3. The extracted capacitance values are shown in Figure 3.32.

The capacitances values that calculated by measured S parameters are shown in Table 3.6. It is shown that the capacitance values decreases with gap increase. For gaps increase from 6 μm to 30 μm , the capacitances decrease from 0.1 pF to 0.07 pF. The capacitances on YIG are bigger than the capacitances on alumina, for the permittivity of YIG (15.4) is bigger than the alumina (9.8).

The analytical results are also given by using the equations given in Section 2.3.2.2: they are almost double the experimental results. This tendency was also observed on alumina in Section 2.4.2.2. Out of the gyroresonance frequency range, the simulated results agree well with experimental results, which seem that the full wave simulation has more accuracy than analytical modelling. Moreover, if comparing the experimental capacitances on alumina and on YIG, there is a factor 1.48 which corresponding the ratio of the effective permittivities.

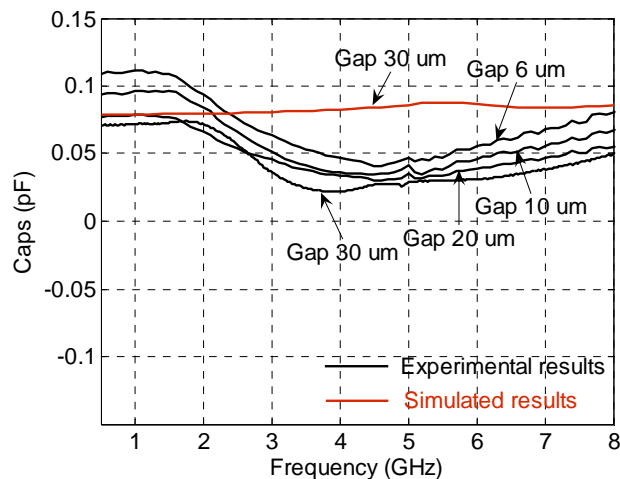


Figure 3.32 Experimental and simulated capacitances values, with gap 6 μm , 10 μm , 20 μm , and 30 μm

Sample	Gap (μm)	Experimental Cap on YIG (pF)	Analytical Cap on YIG (pF)	Experimental Cap on alumina (pF)
Capacitor1 (23)	6	0.11	0.18	X
Capacitor2 (18)	10	0.09	0.16	0.06
Capacitor3 (24)	20	0.08	0.136	0.05
Capacitor4 (22)	30	0.07	0.12	0.045

Table 3.6 Extracted capacitances values

3.5.5 Coplanar interdigital capacitor on ferrite YIG (Sa 1 2 8 ,11)

A CPW interdigital capacitor on YIG is shown in Figure 3.33, its equivalent circuit is shown in Figure 3.34. It consists of shunt capacitances and series capacitance. The finite element simulation and analytical modelling approach mentioned in previous Section 2.4.3 can be used to evaluate the capacitors.

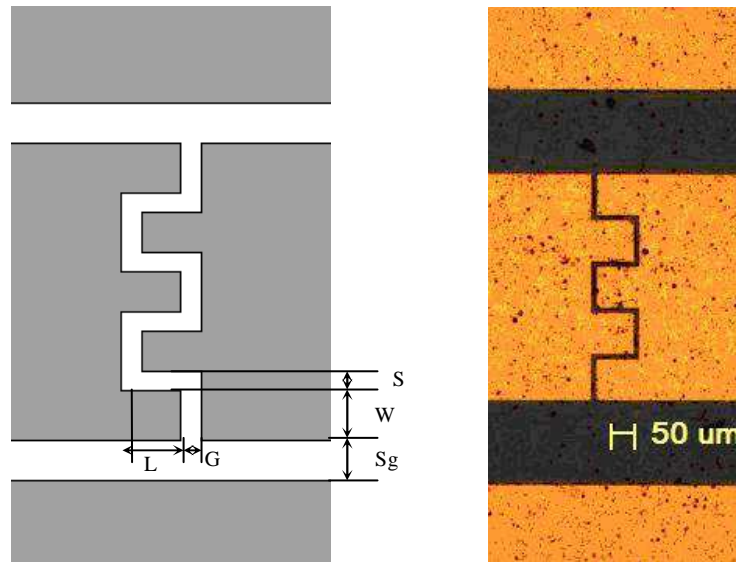


Figure 3.33 CPW interdigital capacitor (prototype), W – finger width, S – finger slot width, G – finger gap width, L – overlapped finger length, S_g – CPW slot width.

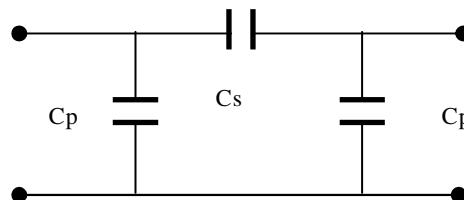


Figure 3.34 Equivalent circuit of CPW interdigital capacitor.

3.5.5.1 Measured and calculated S parameters

In our work, CPW interdigital capacitors having different dimensions are realized, the capacitors dimensions are shown in table 3.7.

Sample	S (μm)	L (μm)	W (μm)	S_g (μm)	G (μm)	L_{rf} (mm)
Capacitor 1 (8)	10	75	72	150	10	4.96
Capacitor 2 (11)	10	100	72	150	10	4.95
Capacitor 3 (1)	10	175	72	150	10	4.91

Table 3.7 Geometrical dimension of CPW interdigital capacitors on substrate YIG

The measured S parameters of the IDCs are given in Figure 3.35. The S_{21} parameter decreases with overlapped finger length increases, for lengths increasing from $75\ \mu\text{m}$ to $175\ \mu\text{m}$, the S_{21} parameters decrease from $-4\ \text{dB}$ to $-8\ \text{dB}$ at $8\ \text{GHz}$.

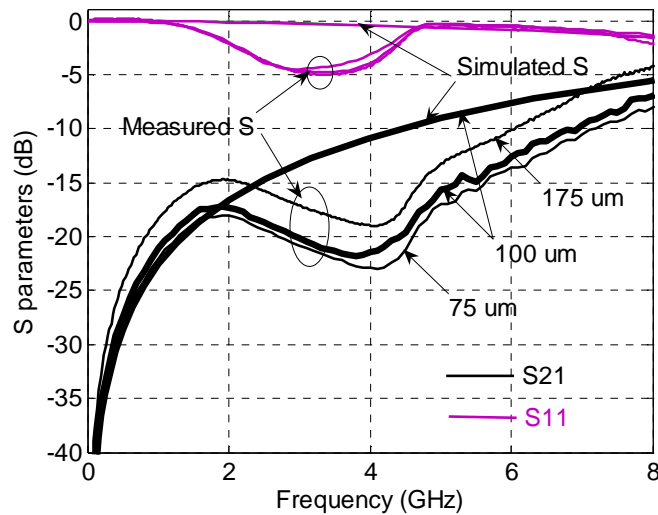


Figure 3.35 Measured and simulated S parameters of IDC, with overlapped finger length $75\ \mu\text{m}$, $100\ \mu\text{m}$, and $175\ \mu\text{m}$. Simulated S parameters obtained on a $1110\ \mu\text{m}$ length sample without field, measured S parameters obtained on a 1cm length sample with some remanent field

The simulated S parameters of capacitor on YIG with finger length $100\ \mu\text{m}$ are also shown in Figure 3.35. Notice that, for saving simulation time, the IDC in software COMSOL is connected to a short CPW with length $100\ \mu\text{m}$.

3.5.5.2 Values of capacitors

The capacitance can be extracted by ABCD parameters by using formula (2.39) given in Section 2.3.2

Figure 3.36 shows that the capacitance values increases with overlapped finger length. As expected, the CPW IDC has a larger capacitance value than CPW gap capacitor. For comparison, the CPW IDC analytical values are calculated with formulas presented in Section 2.3.2.3, the analytical capacitance results are also indicated in Table 3.8. The experimental results agree with analytical results.

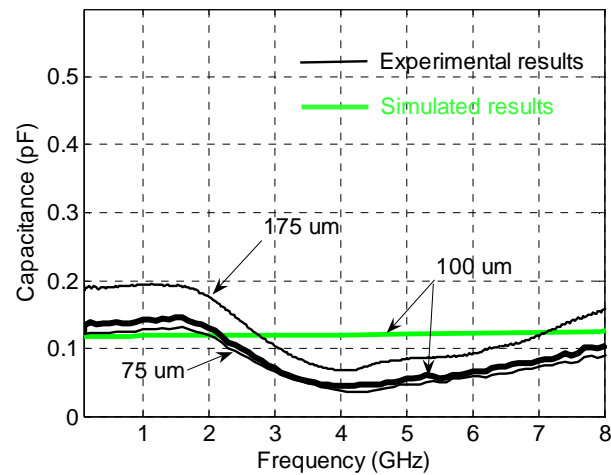


Figure 3.36 Experimental and simulated capacitance values of IDC, with overlapped finger length 75 μm , 100 μm , and 175 μm

Sample	L (μm)	Experimental cap on YIG (pF)	Analytical cap on YIG (pF)	Experimental cap on alumina (pF)
Capacitor1 (8)	75	0.1	0.09	0.078
Capacitor2 (11)	100	0.14	0.1	0.082
Capacitor3 (1)	175	0.19	0.14	X

Table 3.8 Extracted capacitances values of IDC (average at low frequency)

3.5.6 Coplanar shunt inductor on ferrite YIG

A CPW shunt inductor on YIG is shown in Figure 3.37, it's used to build the non reciprocal composite right-left handed transmission line on YIG, the properties of single CPW shunt inductor on YIG will be studied in this section. In our work, 2 inductors with different lengths are studied the dimensions of inductors are shown in Table 3.9.

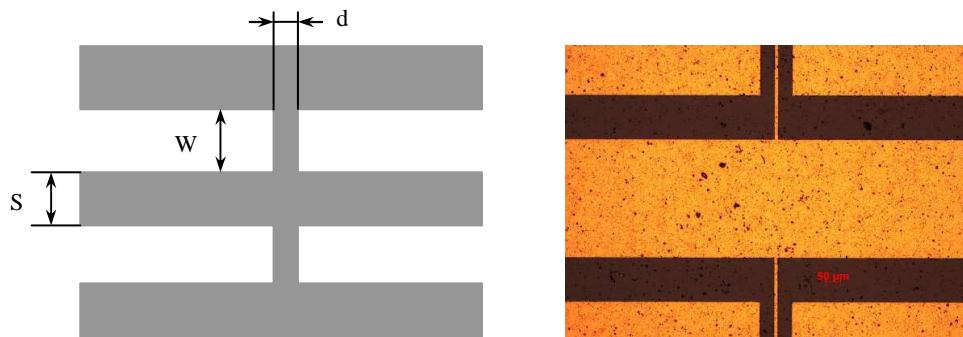


Figure 3.37 CPW shunt inductor on YIG (prototype)

Sample	W (μm)	S (μm)	D (μm)	L _{rf} (mm)	Formula 2.30 (pH)	Formula 2.31 (pH)
Inductor 1 (3)	650	400	10	4.95	640	670
Inductor 2 (19)	1150	400	10	4.95	330	340

Table 3.9 Geometrical dimension of CPW shunt inductors on YIG

Two shunt inductors with length 650 μm and 1150 μm were implemented, measured and simulated. S parameters are given from Figure 3.38 to 3.39. Without applied field, as expected, they are reciprocal networks (See Figure 3.38). For shunt inductor on YIG with length 650 μm , the S_{11} is about -5 dB at 4 GHz, which the S_{21} is about -10 dB. For shunt inductor on YIG with length 1150 μm at 4 GHz, the S_{11} is around -1.5 dB, which the S_{21} is around -15 dB. Here we can not determine the value of inductance, at gyroresonance, the permeability being anisotropic, however, the behavior of these lines is very interesting from the physical point of view.

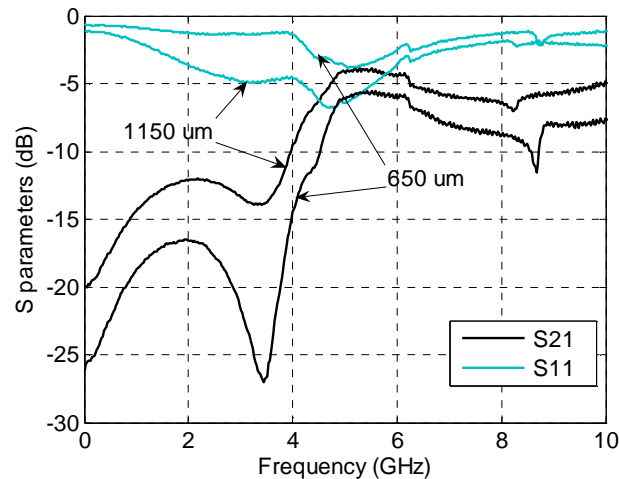


Figure 3.38 Measured S parameters of shunt inductor on YIG without applied field, with inductor length 650 μm and 1150 μm

With applied field 140 kA/m, they are nonreciprocal networks. Moreover, we get two frequency bands, one close to 8.3 GHz and another close to 5.8 GHz, where the nonreciprocal effect is enhanced by the presence of the inductances. The maximum nonreciprocity reaches indeed 20 dB at 8.3 GHz with a transmission parameter of -7 dB. Under the same applied field, the nonreciprocity of a conventional CPW on YIG reaches only 5 dB (see Figure 3.26). The simulated results under an applied field of 140 kA/m are also shown in Figure 3.41. We observe the same tendency as in the experimental results, although the frequency resolution is low. Our results can be compared with the simulated re-

sults of M.A.Abdalla et al. in [20], who simulated CPW on ferrite with shunt inductive load consisting in mending line. His simulated results also foresee an isolation ratio better than 20 dB.

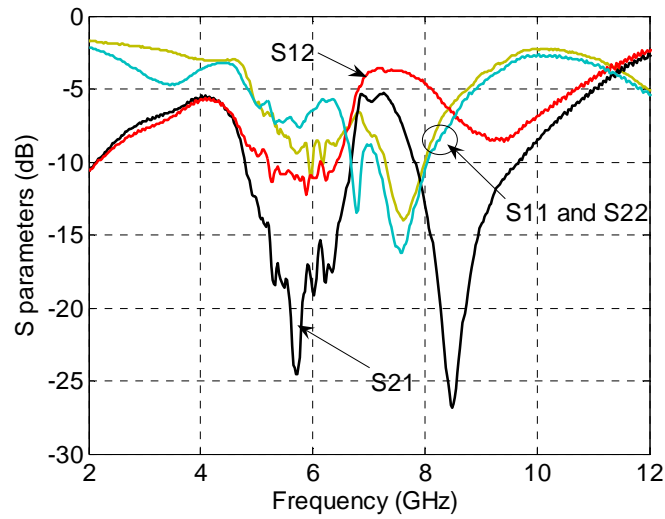


Figure 3.39 Measured S parameters of shunt inductor on YIG with applied field 140 kA/m, with inductor length 1150 μm

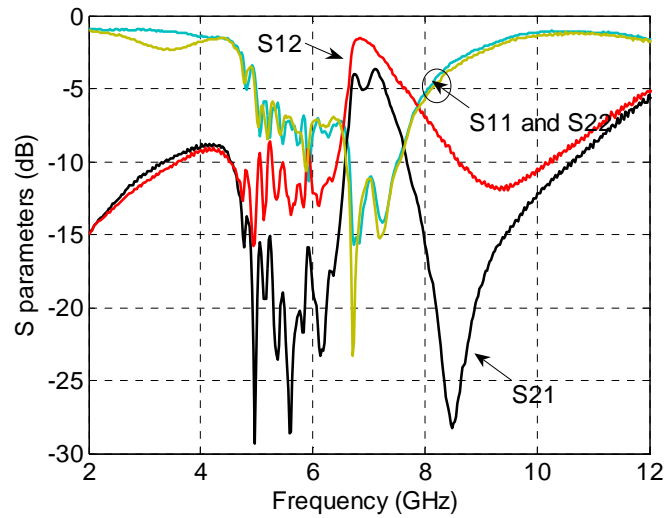


Figure 3.40 Measured S parameters of shunt inductor on YIG with applied field 140 kA/m, with inductor length 650 μm

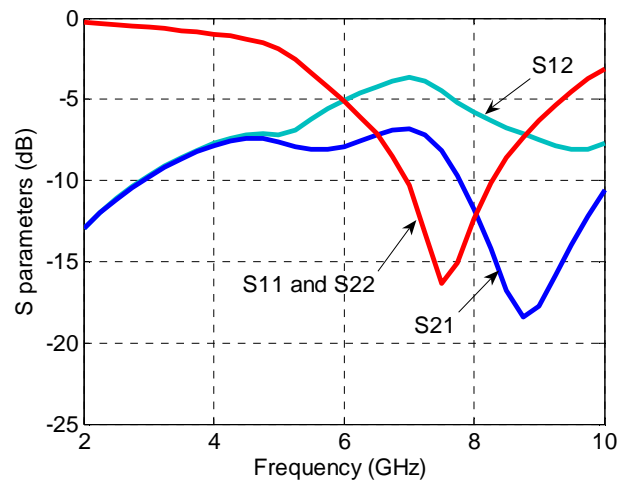


Figure 3.41 Simulated S parameters of shunt inductor on YIG with applied field 140 kA/m, with inductor length 1150 μm , (length of sample 1mm)

In a given frequency band, the negative permeability of the ferrite acts as a series capacitor. This series capacitor has to be added to the equivalent circuit of the TL model (See Figure 3.42). C_x is the series capacitor due to the negative permeability of ferrite, L_x is the shunt inductance, L_R and C_R are distributed elements of the standard CPW on YIG without applied field. The method to calculate the different terms is following:

- Using calculated alpha and beta using $\gamma = \alpha + j\beta = j\omega\sqrt{\mu_{\text{eff}}\epsilon_{\text{eff}}}$ (see Figure 3.27 and 3.28). we deduce the series capacitor C_x by equation [20] considering the properties of the ferrite.:

$$C_x = \text{imag}[Z_0 \sqrt{(\alpha^2 - \beta^2 + j2\alpha\beta)}]$$

Where Z_0 is the characteristic impedande of the transmission line.

- L_x (0.8 nH) is the loaded shunt inductance out of the gyroresonance frequency band

- L_R and C_R are determined to be equal to 390 nH/m and 237 pF/m.

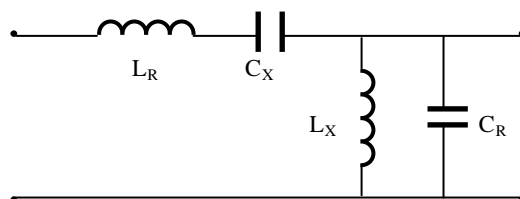


Figure 3.42 Equivalent circuit of unit cell for the ferrite CPW loaded with shunt inductor (L_x)

The estimated dispersion diagram is given below:

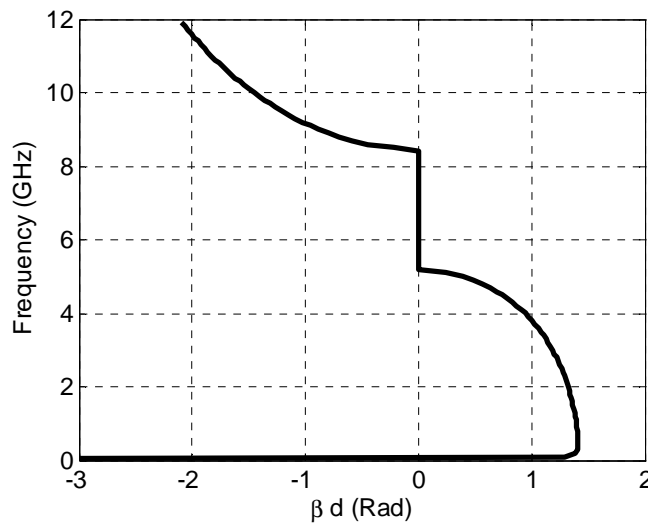


Figure 3.43 Estimated dispersion diagram of the ferrite CPW loaded with shunt inductor (L_s)

This graph will be commented in Chapter 4 using the concepts of combined right left-handed transmission lines.

3.6 Conclusions

The CPW components on ferrite are introduced in this chapter. Firstly, the different kinds of ferrite are described. The fabrication of components is presented in Section 3.3, when it differs from fabrication on alumina. In Section 3.4, the modelling of permeability of ferrite material is described, then simulation with software COMSOL is implemented, and its non-reciprocity is studied using CPW components based on ferrite BaM and YIG. For CPW on ferrite substrate, the measured and simulated S parameters, as well as propagation constant are given. For coplanar capacitors on YIG, the measured and simulated S parameters, and corresponding capacitors values are obtained outside the gyroresonance region. For gap capacitors, the highest value is 0.11 pF, and for interdigital capacitor, which is 0.19 pF. For coplanar inductors on YIG, the measured S parameters with applied field and without applied field are given. The series capacitance due to the negative permeability of YIG is introduced, and the equivalent circuit of the structure is given, as well as the estimated dispersion diagram. In conclusion, the nonreciprocity of the components on YIG with applied field is increased to 20 dB if the CPW is loaded with shunt inductors, which is much higher than that of standard CPW.

3.7 Bibliography

- [1] **Wen C.P.** Coplanar waveguide: A surface strip transmission line suitable for nonreciprocal gyromagnetic device applications. *IEEE Trans. Microwave Theory Tech.*, 1969, vol. 17, No. 12, pp. 1087-1090.
- [2] **ROBERT E. Collin.** « Foundations for microwave engineering », second edition, Wiley-IEEE Press, 2000, 944 p.
- [3] **EOIN C., SVERRE L.** « Millimeter-wave integrated circuits », Boston, Springer, 2005, 288 p.
- [4] **ESKELINEN H.** « Microwave component mechanics », New York/London, Artech House, 2003, 392 p.
- [5] **BAYARD B., SAUVIAC B., VINCENT D.** Ferrite isolators, pp1473 – 14 85. in **CHANG K.** « Encyclopedia of RF and microwave engineering », Wiley-Interscience, 2005, 5832 p.
- [6] **DEHLINGER A. S., LE BERRE M., BENEVENT E., HASSANE H., GIVORD D., LARREY V., VINCENT D.,** Development of millimeter wave integrated circulator based on barium ferrite. *Materials Science and Engineering C*, Volume 28, No. 5-6, 2008, pp. 755-758.
- [7] **PARDAVI-HORVATH M.** Microwave applications of soft ferrites, *J. Magn. Magn. Mater.* Vol. 215-216, 2000, pp. 171-183.
- [8] **SCHLOEMANN E.** Advances in ferrite materials and devices, *J.Magn.Magn.Mater.* Vol. 209, 2000, pp. 15-20.
- [9] **NICOLAS J.** « Ferromagnetic materials », Amsterdam, North-Holland, 1980, Vol. 2, Chap. 4, 604p.
- [10] TEMEX. <http://www.temex-ceramics.com>
- [11] **CAPRARO S., CHATELON J. P., JOISTEN H., LE BERRE M., BAYARD B., BARBIER D.,**

- ROUSSEAU J. J.** Magnetic Properties of sputtered barium ferrite thick films. *J Appl. Phys.*, 2003, 9898-9901
- [12] **BAYAR B., CHATELON J. P., LE BERRE M., JOISTEN H., ROUSSEAU J. J., BARBIER D.** The effect of deposition and annealing conditions on crystallographic properties of sputtered barium ferrite thin films. *Sensors & Actuators A.*, 2002, pp. 207-212.
- [13] **VINCENT D., ROUILLER T., SIMOVSKY C., BAYARD B., NOYEL G.** A new broad-band method for magnetic thin-film characterization in the microwave range. *IEEE Trans Microwave Theory Tech.*, 2005, pp. 1174-1180.
- [14] **BAYARD B., VINCENT D., SIMOVSKI C. R., NOYEL G.** Electromagnetic study of a ferrite coplanar isolator suitable for integration. *IEEE Trans Microwave Theory Tech.*, 2003, pp.1809-1814.
- [15] **CAPRARO S., BOUDIAR T., ROUILLER T., CHATELON J.P., BAYARD B., LE BERRE M., PAYET G.B.,BLANC-MIGNON M.F., ROUSSEAU J.J.** Exploration of a thin YIG film-based coplanar isolator. *Microwave and optical technology letters*, Vol. 42, No. 6, 2004, pp. 470-471.
- [16] **MARQUES R., MESA F., MEDINA F.** Generalized quasi-tem approximation and telegrapher equations for non-reciprocal ferrite-loaded transmission lines. *IEEE microwave and guided wave letters*, Vol.10, NO.6, 2000, pp. 225-227.
- [17] **MARQUES R., HORNO M.** Propagation of quasistatic modes in anisotropic transmission lines. *IEEE Trans. Microwave Theory Tech.*, Vol. 33, 1985, pp.927-933.
- [18] **LINDELL I.** On the quasi-tem modes in inhomogeneous multiconductor transmission lines. *IEEE Trans. Microwave Theory Tech.*, Vol. 29, 1981, pp.812-817.
- [19] LT2C Laboratory. <http://LT2C.telecom-st-etienne.fr/FRA/index.html>

- [20] **ABDALLA M.A., HU Z.** Nonreciprocal left handed coplanar waveguide over ferrite substrate with only shunt inductive load, Microwave and optical technology letters, Vol. 49, No. 11, 2007, pp.2810 – 2814

4 Coplanar composite right/left - handed metamaterials

4.1 Introduction

Recently, there has been a great deal of interest in the composite right/left-handed transmission lines (CRLH TLs) metamaterials (MTMs) [1-13], which introduced by Caloz and E leftheriades. The CRLH-TL can be realized by using traditional right-handed (RH) transmission lines loaded with series interdigital capacitors (IDCs) and shunt inductors. Many applications with these structures like couplers, impedance transformers, innovative filters and others have been reported. In this chapter, the theory of transmission line approach of metamaterials will be introduced first. Then, the coplanar CRLH MTMs on alumina with gap capacitors and interdigital capacitors, and the CRLH MTMs on YIG with or without applied fields will be studied.

4.2 Modelling, simulation, and calculation

4.2.1 Transmission line approach of metamaterials

There are mainly 2 approaches for designing LH metamaterials, resonant approach [10] and transmission line approach [1, 11]. For resonant approach, the LH metamaterials are based on cascaded unit-cell combining a SRR (negative permeability) with a metal wire (negative permittivity). Because SRR-based metamaterials have only LH properties around the resonance, it has several drawbacks such as narrow bandwidth, high lossy, and highly dispersive. For engineering applications, to overcome the weaknesses of resonant approach based LH metamaterials, a non resonant LH metamaterial can be realized by transmission line approach, which are based on the dual configuration of a conventional right-handed transmission line. The transmission line approach of metamaterials will be discussed in this section.

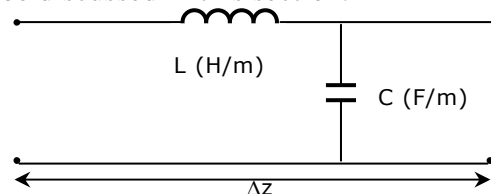


Figure 4.1 Equivalent circuit of purely-right handed transmission lines.

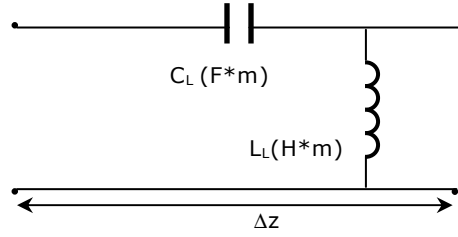


Figure 4.2 Equivalent circuit of purely-left handed transmission lines.

The conventional RH transmission line can be modelled as unit-cell with series inductance and shunt capacitance, as shown in Figure 4.1. The novel LH transmission line can be modelled as unit-cells with series capacitance and shunt inductance, which can be seen in Figure 4.2

The propagation constants for the RH and LH unit-cell [1]:

$$\beta_{RL} = \omega \sqrt{C_R L_R} \quad (4.1)$$

$$\beta_{LH} = \frac{-1}{\omega \sqrt{C_L L_L}} \quad (4.2)$$

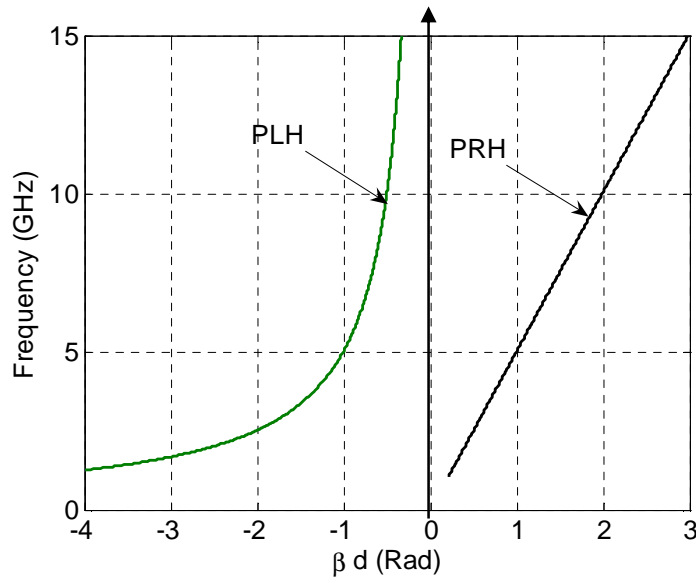


Figure 4.3 βd of a PLH TL and PRH TL ($L_R = 1$ nH, $C_R = 1$ pF, $L_L = 1$ nH, $C_L = 1$ pF)

For the lossless case LH TL ($\alpha = 0$), the complex propagation constant γ , the propagation constant β , the characteristic impedance Z_c , the phase velocity V_p , and the group velocity V_g are given by the formulas below,

$$\gamma = \alpha + j\beta = \sqrt{Z'Y'} = \frac{1}{j\omega \sqrt{L_L' C_L'}} \quad (4.3)$$

$$\beta = \frac{-1}{\omega \sqrt{L_L' C_L'}} < 0 \quad (4.4)$$

$$Z_c = \sqrt{\frac{Z'}{Y'}} = \sqrt{\frac{L_L'}{C_L'}} > 0 \quad (4.5)$$

$$V_p = \frac{\omega}{\beta} = -\omega^2 \sqrt{L_L' C_L'} < 0 \quad (4.6)$$

$$V_g = \left(\frac{\partial \beta}{\partial \omega} \right)^{-1} = \omega^2 \sqrt{L_L' C_L'} > 0 \quad (4.7)$$

where

$Z' = 1/(j\omega C_L')$ is per unit length impedance

$Y' = 1/(j\omega L_L')$ is per unit length admittance

It is shown that the phase and group velocities of LH TL are anti-parallel, $V_p \parallel V_g$. The phase velocity V_p , related to the direction of phase propagation (β), is negative, while the group velocity V_g , related to the direction of power flow (Poynting vector S), is positive. As LH TL is a non resonant structure, it exhibits low loss and broad bandwidth. In reality, a purely LH TL does not exist because of unavoidable RH parasitic series inductances and shunt capacitances effects [1], will unavoidably occur due to currents flowing in the conductors and voltage gradients developing between the conductors and the ground planes, therefore, the concept of CRLH MTMs, introduced by Caloz et al [1], present the most general form of a LH TL. The CRLH consists of a series inductance, series capacitance, shunt inductance and shunt capacitance. The Equivalent circuit of a loss-less CRLH TL is shown in Figure 4.4.

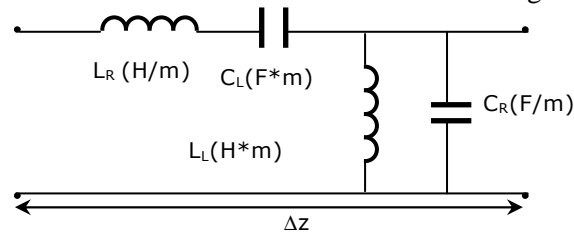


Figure 4.4 Equivalent circuit of the CRLH TL

The series and shunt resonance frequencies:

$$f_{se} = \frac{1}{2\pi\sqrt{L_R' C_L'}} = \frac{\omega_{se}}{2\pi} \quad (4.8)$$

$$f_{sh} = \frac{1}{2\pi\sqrt{L_L' C_R'}} = \frac{\omega_{sh}}{2\pi} \quad (4.9)$$

f_{se} is larger than f_{sh} or f_{sh} larger than f_{se} depending on the L C parameters.

The per-unit length impedance and per-unit length admittance:

$$Z'(\omega) = j(\omega L_R' - \frac{1}{\omega C_L'}) \quad (4.10)$$

$$Y'(\omega) = j(\omega C'_R - \frac{1}{\omega L'_L}) \quad (4.11)$$

The purely-LH impedance and purely-RH impedance:

$$Z_L = \sqrt{\frac{L'_L}{C'_L}} \quad (4.12)$$

$$Z_R = \sqrt{\frac{L'_R}{C'_R}} \quad (4.13)$$

The transition frequency (maximum attenuation):

$$f_0 = \frac{1}{2\pi\sqrt{L'_R C'_R L'_L C'_L}} = \frac{\omega_0}{2\pi} \quad (4.14)$$

The phase velocity V_p , and group velocity V_g , of the CRLH TL are given below

$$V_p = \frac{\omega}{\beta} = S(\omega) \frac{\omega}{\sqrt{(\omega/\omega'_R)^2 + (\omega'_L/\omega)^2 - k\omega_L^2}} \quad (4.15)$$

$$V_g = \left(\frac{d\beta}{d\omega}\right)^{-1} = \frac{|\omega\omega'^{-2}_R - \omega^{-3}\omega'^2_L|}{\sqrt{(\omega/\omega'_R)^2 + (\omega'_L/\omega)^2 - k\omega_L^2}} \quad (4.16)$$

where:

$$\omega_L = \frac{1}{2\pi\sqrt{L'_L C'_L}} \quad (4.17)$$

$$\omega_R = \frac{1}{2\pi\sqrt{L'_R C'_R}} \quad (4.18)$$

$$k = L'_R C'_L + L'_L C'_R \quad (4.19)$$

The equivalent constitutive parameters (permeability and permittivity) of a CRLH TL are presented below

$$\mu = \frac{Z'(\omega)}{j\omega} = L'_R - \frac{1}{\omega^2 C'_L} \quad (4.20)$$

$$\varepsilon = \frac{Y'(\omega)}{j\omega} = C'_R - \frac{1}{\omega^2 L'_L} \quad (4.21)$$

When the series and shunt resonances of the CRLH TL are different, this condition is called the unbalanced case.

The complex propagation constant γ , the propagation constant β of CRLH and the characteristic impedance are given by the formulas below

$$\gamma = \alpha + j\beta = \sqrt{Z'(\omega)Y'(\omega)} \quad (4.22)$$

$$\beta(\omega) = S(\omega) \sqrt{\omega^2 L'_R C'_R + \frac{1}{\omega^2 L'_L C'_L} - \left(\frac{L'_R}{L'_L} + \frac{C'_R}{C'_L} \right)} \quad (4.23)$$

where

$$S(\omega) = \begin{cases} -1 & \text{if } \omega < \omega_{\tau 1} = \min \left(\frac{1}{\sqrt{L'_R C'_L}}, \frac{1}{\sqrt{L'_L C'_R}} \right) \quad \text{LH range} \\ +1 & \text{if } \omega < \omega_{\tau 2} = \max \left(\frac{1}{\sqrt{L'_R C'_L}}, \frac{1}{\sqrt{L'_L C'_R}} \right) \quad \text{RH range} \end{cases} \quad (4.24)$$

$$Z_c = \sqrt{\frac{Z'(\omega)}{Y'(\omega)}} \quad (4.25)$$

When the series resonances and shunt resonances are equal ($L'_R C'_L = L'_L C'_R$), the LH and RH contribution balance each other at a frequency; this condition is called the balanced case.

The transition frequency:

$$f_0 = \frac{1}{2\pi\sqrt{L'_R C'_R}} = \frac{1}{2\pi\sqrt{L'_L C'_L}} = \frac{\omega_0}{2\pi} \quad (4.26)$$

For the balanced case, the propagation constant can be simplified as:

$$\beta = \beta_R + \beta_L = \omega\sqrt{L'_R C'_R} - \frac{1}{\omega\sqrt{L'_L C'_L}} \quad (4.27)$$

The characteristic impedance of balanced CRLH TL is:

$$Z_c = Z_L = Z_R \quad (4.28)$$

Notice that, in microwave engineering, $p = \lambda_g / 4$ is the rule to distinguish lumped components and distributed components, where p is the size of the component, λ_g is the wavelength in a media [1].

When $p < \lambda_g / 4$, the component can be considered to be a lumped component, the phase variation of the input wave and output wave can be ignored.

When $\lambda_g / 4 < p < \lambda / 2$, the component can be considered to be a quasi-lumped component;

When $p > \lambda_g / 2$, the component is a distributed component, the phase variation can not be ignored.

If the component size is smaller than $\lambda_g / 4$, we don't need to take into account the phase variation of the component, the equivalent circuit consists of lumped components. When the component size is larger than $\lambda_g / 4$, we have to take into account the phase variation of the component, the equivalent circuit is composed of distributed structures with lumped components. As we will see in the following, the CRLH MTMs studied are distributed structures with lumped components.

4.2.2 Simulation and calculation

The equivalent circuit of CRLH can be easily simulated by the software ADS. For the 3D model, the software COMSOL can be used to make full-wave electromagnetic simulation, the same as shown in Section 2.3 and Section 3.4.

For the circuit simulation, we need to input the values of capacitors and inductors, define the characteristic impedance of feed port (50 ohms), set the solver, and then solve the problem. Then, we can get the S parameters.

For the 3-d simulation in COMSOL, we made the same steps as shown in Section 2.3 and Section 3.4. When specifying the physics: if considering YIG, the permeability tensor of YIG should be defined as in Equation 3.7. Assuming that the internal field of YIG equals the applied field, the demagnetizing factors (N_x, N_y, N_z) of YIG are defined as (1/3, 1/3, 1/3).

The simulated S parameters can be applied to calculate the propagation constants. For a nonreciprocal network, the same method presented in Section 3.4 can be used to calculate the propagation constants. The software Matlab is used to make calculation.

$$\gamma^+ * d = \ln \left[\frac{(1 - S_{11}S_{22} + S_{12}S_{21}) \pm \sqrt{(1 - S_{11}S_{22} + S_{12}S_{21})^2 - 4S_{12}S_{21}}}{2S_{21}} \right] \quad (4.29)$$

$$\gamma^- * d = \ln \left[\frac{(1 - S_{11}S_{22} + S_{12}S_{21}) \pm \sqrt{(1 - S_{11}S_{22} + S_{12}S_{21})^2 - 4S_{12}S_{21}}}{2S_{12}} \right] \quad (4.30)$$

where only the denominator changes. The propagation constant is such that:

$$\alpha^+ * d = \text{real}(\gamma^+ * d) \quad (4.31)$$

$$\alpha^- * d = \text{real}(\gamma^- * d) \quad (4.32)$$

$$\beta^+ * d = \text{imag}(\gamma^+ * d) + \theta_1 \quad (4.33)$$

$$\beta^- * d = \text{imag}(\gamma^- * d) + \theta_2 \quad (4.34)$$

4.2.3 Example

To validate our calculation method of the propagation constant, we chose the lumped elements of the equivalent circuit: $L_R = 20\text{nH}$, $L_L = 5\text{nH}$, $C_L = 2.5\text{pF}$, and $C_R = 2\text{pF}$ from [12] to model an unbalanced CRLH TL. To model a balanced CRLH TL, we choose arbitrarily the equivalent circuit parameters $L_R = 5\text{nH}$, $L_L = 5\text{nH}$, $C_L = 2\text{pF}$, and $C_R = 2\text{pF}$. The circuits are simulated by ADS, the simulated S parameters are shown in Figure 4.5.

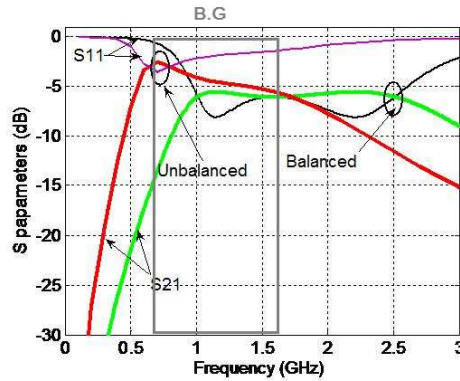


Figure 4.5 Simulated S parameters of a unbalanced and balanced CRLH TL. Correspond to the unbalanced case, the balanced case does not have bandgap

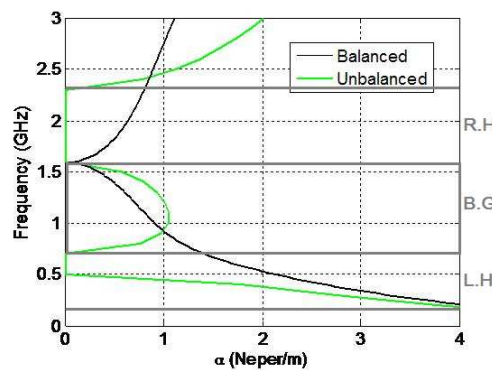


Figure 4.6 α of a unbalanced and balanced CRLH TL.

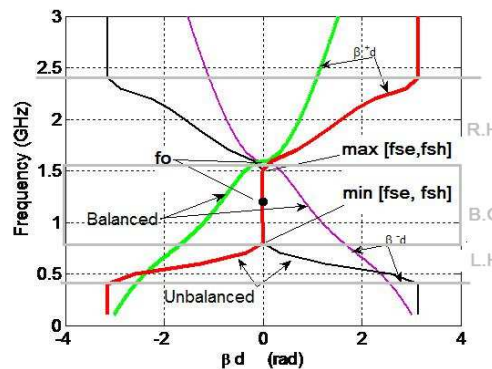


Figure 4.7 β of a unbalanced and balanced CRLH TL, f_0 indicated for balanced and unbalanced conditions, the bands left-handed (L.H), bandgap (B.G) and right-handed (R.H)

The calculated dispersion and attenuation relations are plotted in Figure 4.6 and Figure 4.7. For the unbalanced CRLH, the crystal band gap is below 0.5 GHz, the LH band (backward propagation) is 0.5 - 0.7 GHz, pure plasma band (bandstop) is 0.7 - 1.6 GHz, the RH band (forward propagation) is 1.6 GHz - 2.31 GHz, and the crystal band gap exists above 2.31 GHz. For the balanced CRLH, we can see that, a LH band (backward propagation) exists below 1.6 GHz, and a RH band (forward propagation) exists above 1.6 GHz. At 1.6 GHz, α and β is zero.

These graphs agree with the transmission line theory of CRLH, they illustrated the possible realization of CRLH TL using distributed or lumped elements.

4.3 CRLH metamaterials on alumina

The geometry of CRLH MTM on alumina substrate is shown in Figure 4.8. In general, we have 2 kinds CRLH MTM; the first one is integrated with gap capacitors, and the second one with interdigital capacitors. The properties of CPW, capacitors, and inductors on alumina have been studied in Chapter 2. The dimensions of CRLH MTM and corresponding values of capacitors and inductors are shown in Table 4.1.

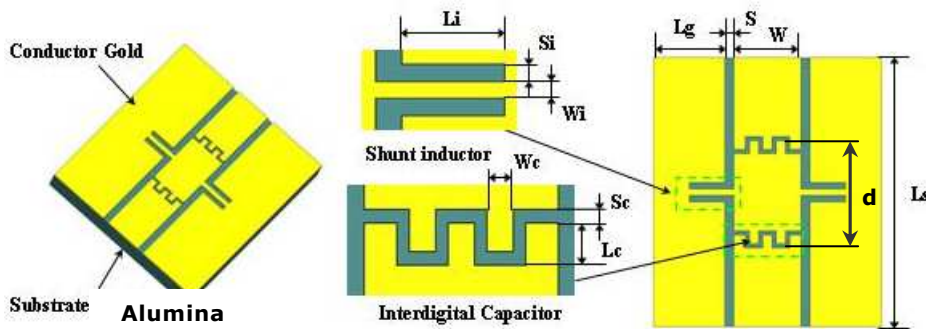


Figure 4.8 Geometry of CRLH MTM on alumina

Sample number	Unit length d(μm)	Cap gap/Finger length (μm)	Ind length (μm)	Cap (pF)	Ind (nH) measured	Lrf (mm)
16 1 unit	1520	20/	1150	0.05	0.4	2.090
20 1 unit	1520	10/	1150	0.06	0.4	2.1
7 1 unit	2195	10/75 IDC	650	0.078	0.25	2
10 1 unit	2195	10/100 IDC	650	0.082	0.25	2
13 1 unit	4195	10/75 IDC	650	0.078	0.25	5
12 1 unit	10195	10/100 IDC	650	0.082	0.25	5
6 8 units	4220	10/75 IDC	650	0.078	0.25	3
21 8 units	3020	10/	1150	0.06	0.4	5

Table 4.1 Dimensions of CRLH MTM and values of capacitors and inductors, Lrf is the length of reference plane shift

4.3.1 Equivalent circuits

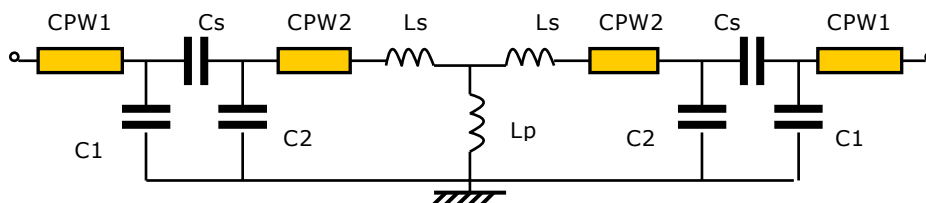


Figure 4.9 Equivalent circuit of the CRLH MTM on substrate alumina

According to the transmission line theory of CRLH, the equivalent circuit of the

CRLH MTM on substrate alumina is shown in Figure 4.9. It is composed of CPW, lumped series capacitors and shunt inductors. The influence of CPW2 length, capacitor type (different values of capacitors), and inductor length (different values of inductors) will be studied in this section.

4.3.2 Measured and simulated S parameters

The components of the CRLH MTM have been implemented and measured. For measurements, the reference planes are not shifted when representing the S parameters, however they are shifted to calculate the propagation constant. Regarding simulation, as in the previous chapters, the reference planes are always shifted for computing time sparing.

The figures 4.10 to 4.13 depict the measured and simulated S parameters of unit cell of CRLH TL. In figure 4.10 and 4.11, the unit length (length of 2 CPW2) is rather small, whereas in figure 4.12 to 4.14, it is larger. Now the major differences between figure 4.10 and 4.11 is that the decrease in the value of L_L is roughly compensated by a increase of capacitance.

In figure 4.10, the resonance frequency is about 12 GHz with capacitor gap 20 μm , and about 11.5 GHz with capacitor gap 10 μm , the resonance frequency of CRLH TL increases with the gap width (capacitor values decrease), as expected from relation Equation 4.17.

For a 1-unit CRLH MTM with IDC, the resonance frequency decreases as the overlapped finger length of IDC increases (see Figure 4.11). For the CRLH MTM with finger length 75 μm , the 2 resonance frequencies are around 12.5 GHz and 19.5 GHz; for the one with finger length 100 μm , the 2 resonance frequencies are around 12 GHz and 19 GHz.

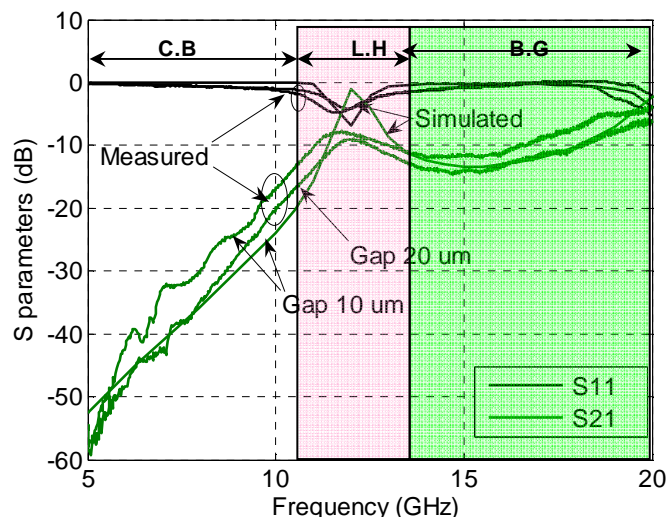


Figure 4.10 S parameters of CRLH MTM on alumina, unit length 1520 μm , capacitor gap 10 μm and 20 μm , inductor length 1150 μm (sample 16 and 20), crystal bandgap (C.B)

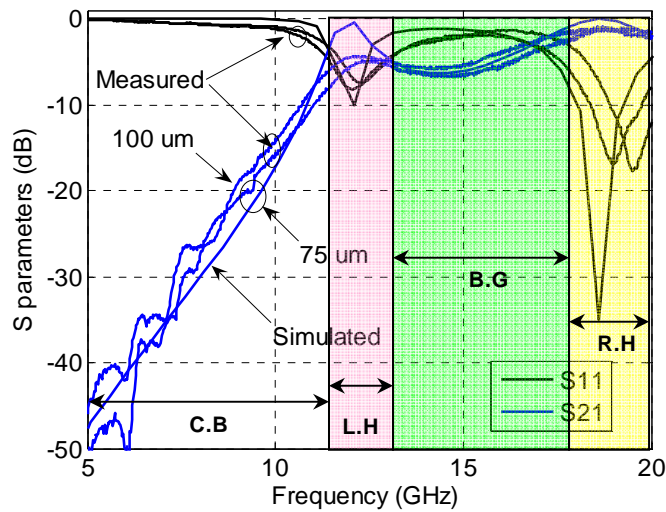


Figure 4.11 S parameters of CRLH MTM on alumina, unit length 2195 μm , IDC finger length 75 μm and 100 μm , inductor length 650 μm (sample 7 and 10)

It's found in Figure 4.12 and Figure 4.13 that, with a longer unit length of CPW2, the CRLH MTM has a lower resonance frequency, due to the increase of C_R and L_R (Equation 4.18). The increase of the IDC finger lengths between the 2 CRLH TL also act towards a lower resonance frequency. For the CRLH MTM with unit length 4195 μm , the 2 resonances are around 8.5 GHz and 12 GHz; for which unit length 10195 μm , 3 resonance frequencies are around 5.8 GHz, 14.6 GHz and 17 GHz.

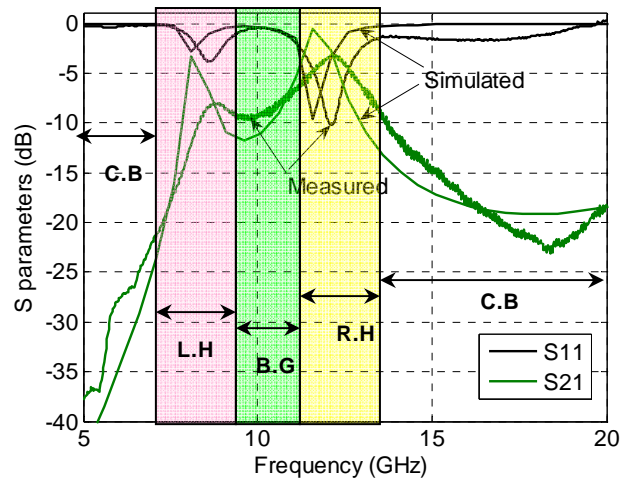


Figure 4.12 S parameters of CRLH MTM on alumina, unit length 4195 μm , IDC finger length 75 μm , inductor length 650 μm (sample 13)

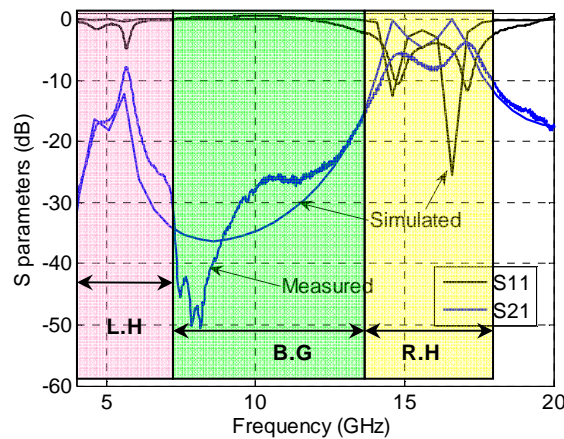


Figure 4.13 S parameters of CRLH MTM on alumina, unit length 10195 μm , IDC finger length 100 μm , inductor length 650 μm (sample 12)

The S parameters of 8-unit CRLH MTM with gap capacitor and IDC are shown in Figure 4.14 and Figure 4.15 respectively. For 8-unit CRLH MTM with gap capacitor 10 μm , the passband (several resonances) is 13.5 to 17 GHz (S_{21} and S_{12} larger than -20 dB). For the 8-unit CRLH MTM with IDC, the passband is 11-14 GHz, which is lower than the previous one, because it has a longer unit length and larger value of series capacitance. If we compare the S parameters of 1-unit cell with 8 unit cells, we observe that, when the number of cells increases, the cut off frequencies become sharper, which has also been reported elsewhere.

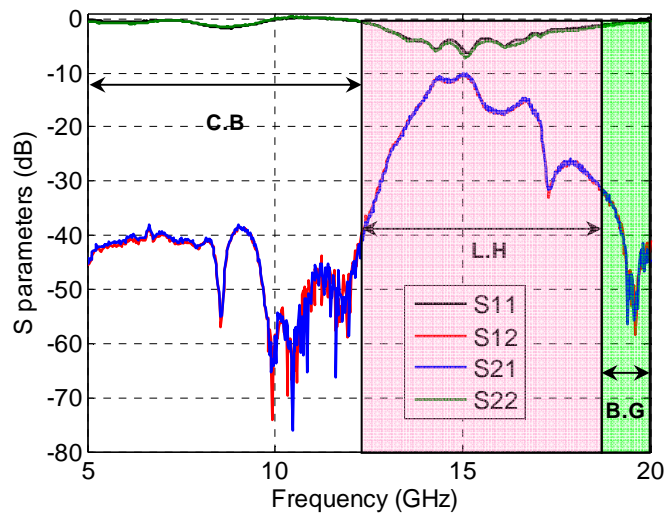


Figure 4.14 Measured S parameters of 8-unit CRLH MTM on alumina, unit length 3020 μm , capacitor gap 10 μm , inductor length 1150 μm (sample 21)

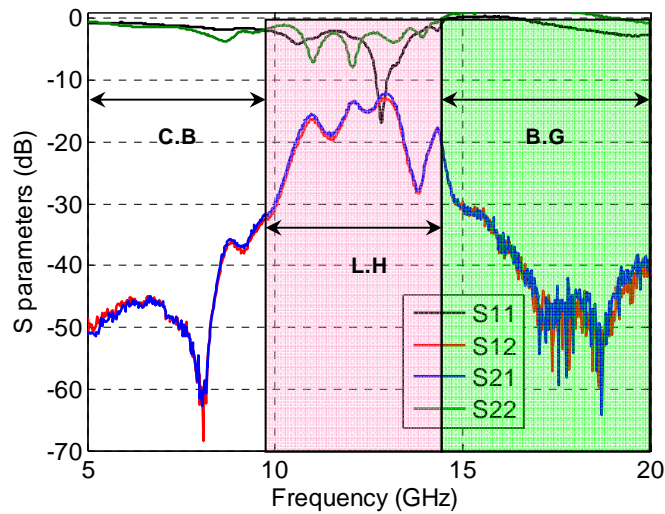


Figure 4.15 Measured S parameters of 8-unit CRLH MTM on alumina, unit length 4220 μm , IDC finger length 75 μm , inductor length 650 μm (sample 6)

4.3.3 Propagation constants

The experimental and simulated dispersion diagram obtained using the equations 4.29 and 4.30. Figure 4.16 shows the dispersion diagram of the CRLH MTMs with gap capacitance, the frequency of $\min(f_{se}, f_{sh})$ is about 13 GHz; the left-handed frequency band is obtained around 12 GHz, where the slope of frequency as a function of β is opposite to β .

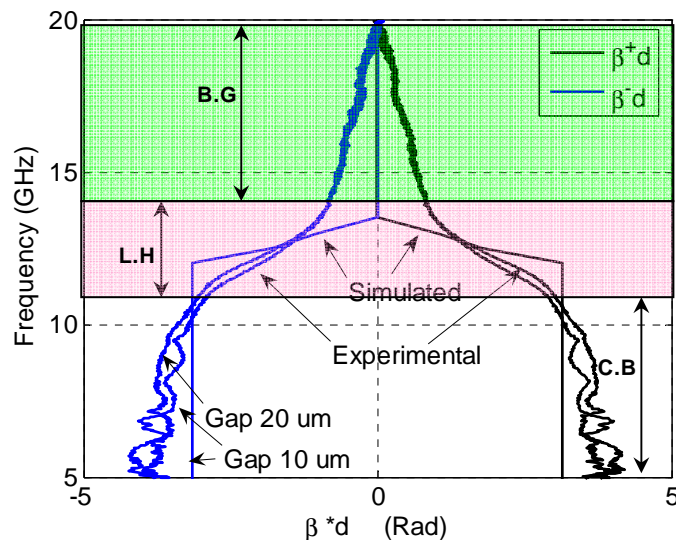


Figure 4.16 Experimental and simulated propagation constants of CRLH on alumina, unit length 1520 μm , capacitor gap 10 μm and 20 μm , inductor length 1150 μm . (sample 16 and 20)

Then, when the unit length of CRLH MTM is changed from 1520 μm to 2195 μm , and the length of shunt inductance changed from 1150 μm to

650 μm , the S parameters are shown in Figure 4.17. The frequency of frequency of $\min(f_{se}, f_{sh})$ is around 13.5 GHz; the LH frequency band is observed around 13 GHz, where the slope of frequency as a function of β is opposite to β .

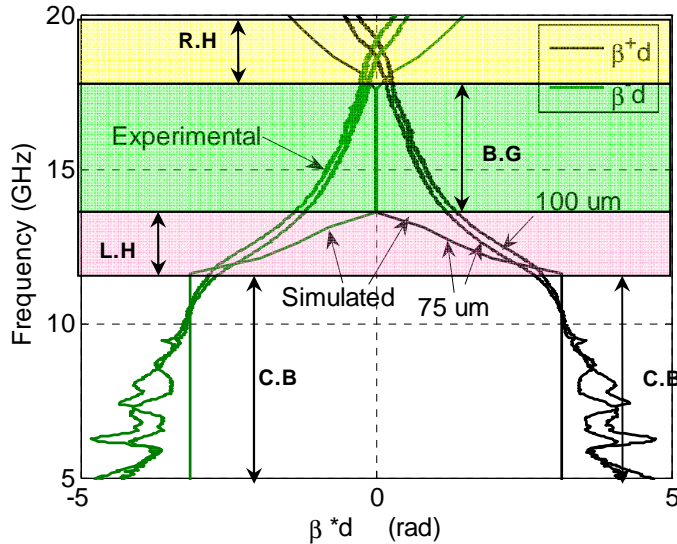


Figure 4.17 Experimental and simulated propagation constants of CRLH on alumina, unit length 2195 μm , IDC finger length 75 μm and 100 μm , inductor length 650 μm (sample 7 and 10)

We see in Figure 4.18 that, when the unit length of CRLH MTM changes from 2195 μm to 4195 μm , the frequency of frequency of $\min(f_{se}, f_{sh})$ is about 13.5 GHz to about 9.3 GHz, the LH frequency band is also observed around 9 GHz.

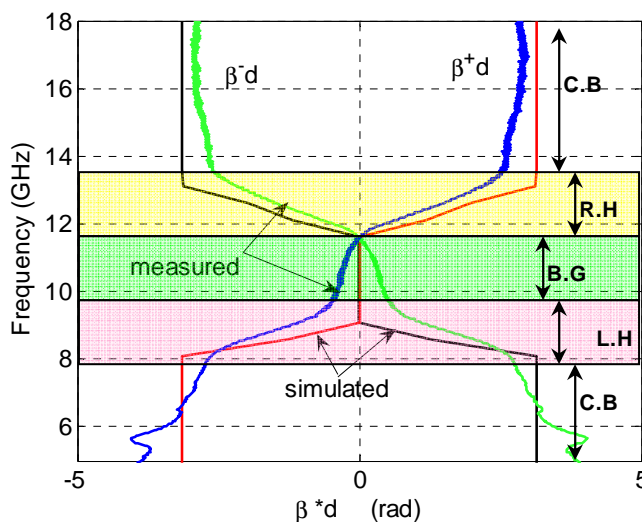


Figure 4.18 Propagation constants of CRLH MTM on alumina, unit length 4195 μm , IDC finger length 75 μm , inductor length 650 μm (sample 13)

Figure 4.19 shows that, when the unit length of CRLH MTM is

changed from 4195 μm to 10195 μm , The frequency of frequency of $\min(f_{se}, f_{sh})$ is changed from 9.3 GHz to about 6.5 GHz, the LH frequency band is also observed around 5.5 GHz, the RH frequency band is obtained around 15 GHz.

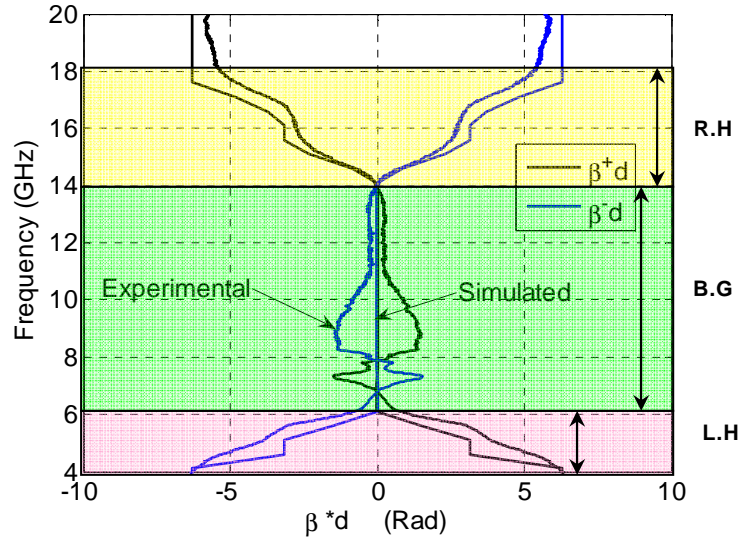


Figure 4.19 Propagation constants of CRLH MTM on alumina, unit length 10195 μm , IDC finger length 100 μm , inductor length 650 μm (12)

The propagation constants of 8-unit CRLH MTM with unit length 3020 μm , capacitor gap width 10 μm , and inductor length 1150 μm is shown in Figure 4.20, which with unit length 4220 μm , IDC finger length 75 μm and inductor length 650 μm is shown in Figure 4.21. For the first CRLH, the transition frequency f_0 is around 17 GHz, and the LH frequency band is around 15 GHz; for the later CRLH, the transmission frequency f_0 is around 17 GHz, and the LH frequency band is around 12 GHz.

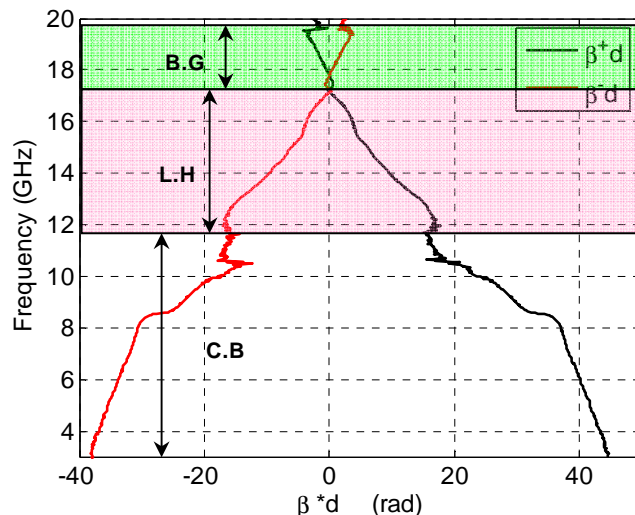


Figure 4.20 Propagation constants of 8-unit CRLH MTM on alumina, unit length 3020 μm , capacitor gap 10 μm , inductor length 1150 μm (sample 21)

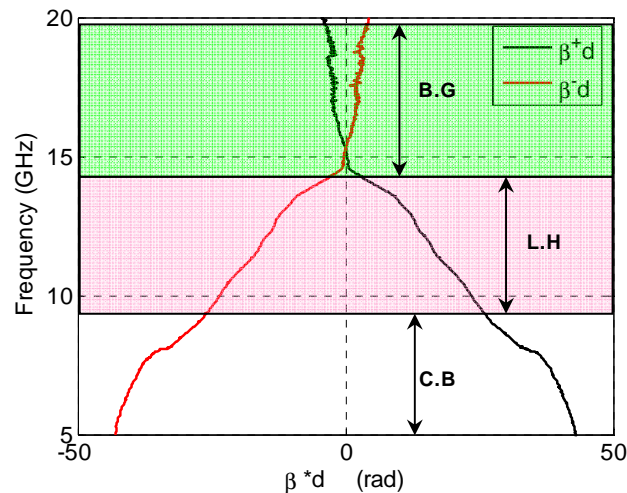


Figure 4.21 Propagation constants of 8-unit CRLH MTM on alumina, unit length 4220 μm , IDC finger length 75 μm , inductor length 650 μm (sample 6)

4.4 CRLH MTM on YIG without applied field

A CRLH MTM on YIG substrate is shown in Figure 4.22. In the same way as on alumina, 2 kinds CRLH MTM on YIG have been studied; the first one is integrated also with gap capacitors, and the second one with interdigital capacitors. The properties of CPW, capacitors, and inductors on YIG substrate are studied in previous Chapter 3. The dimensions of CRLH MTM and corresponding values of capacitors and inductors are shown in Table 4.2.

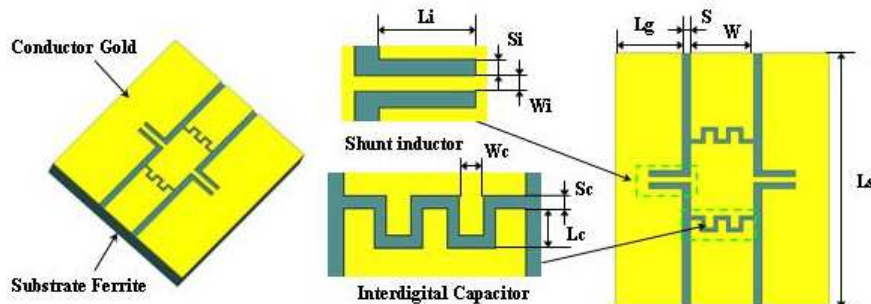


Figure 4.22 CRLH MTM on YIG

Sample	Unit length (μm)	Cap gap/Finger length (μm)	Ind length (μm)	CPW (mm)
16 1 unit	1520	20/	1150	2.090
20 1 unit	1520	10/	1150	2.1
7 1 unit	2195	10/75 IDC	650	2
10 1 unit	2195	10/100 IDC	650	2
13 1 unit	4195	10/75 IDC	650	5
9 1 unit	10195	10/75 IDC	650	5
12 1 unit	10195	10/100 IDC	650	5
6 8units	4220	10/75 IDC	650	3
5 8units	4220	10/100 IDC	650	5
21 8units	3020	10/	1150	5

Table 4.2 Dimensions of CRLH MTM

4.4.1 Equivalent circuits

The equivalent circuit of the CRLH MTM on YIG substrate is shown in Figure 4.23. It's composed of CPW on YIG substrate, shunt capacitors and shunt inductors, series capacitors and series inductors.

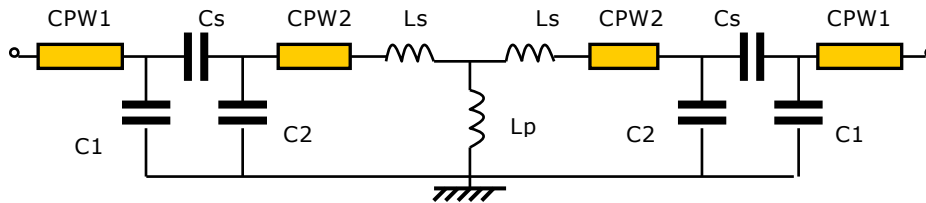


Figure 4.23 Equivalent circuit of the CRLH MTM on YIG

4.4.2 S parameters

For all samples, if we compare the localization of the bands for both alumina and YIG substrate, we observe a shift to low frequencies of the bands, related to an increase both C_R and C_L , due to the increase of the substrate permittivity. The measured and simulated S parameters of CRLH MTM on YIG substrate with gap capacitors are shown in Figure 4.24. The CRLH MTM on YIG without applied field is reciprocal component. For the CRLH with capacitor gap $20\ \mu\text{m}$, there are resonances at about 9.5 GHz and 16.8 GHz; for the CRLH capacitor gap $10\ \mu\text{m}$ are about 9.3 GHz and 16.3 GHz.

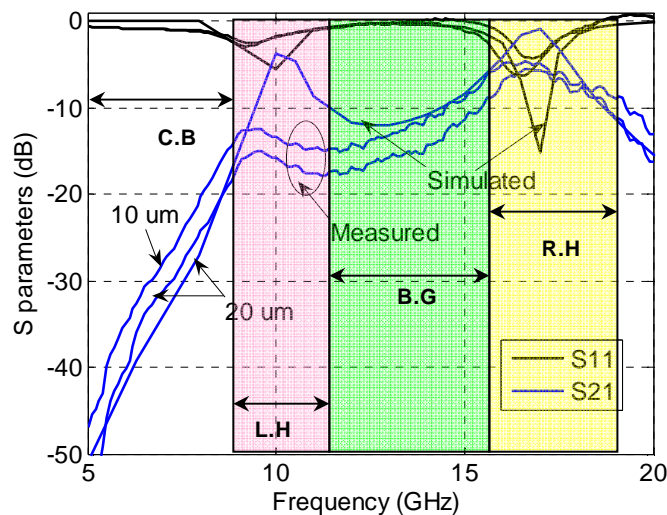


Figure 4.24 Measured S parameters of CRLH MTM on YIG, unit length $1520\ \mu\text{m}$, capacitor gap $10\ \mu\text{m}$ and $20\ \mu\text{m}$, inductor length $1150\ \mu\text{m}$ (16 20)

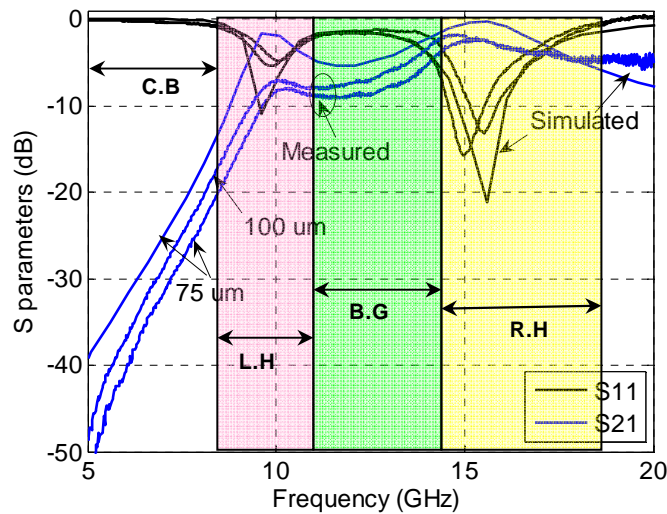


Figure 4.25 Measured and simulated S parameters of CRLH MTM on YIG, unit length 2195 μm , IDC finger length 75 μm and 100 μm , inductor length 650 μm (sample 7 and 10)

In the Figure 4.25, for 1-unit CRLH MTM on YIG substrate with interdigital capacitors, the resonance frequency increases with the overlapped finger length of IDC. For the CRLH MTM with finger length 75 μm , the 2 resonances are around 10 GHz and 15.5 GHz; for which with finger length 100 μm , the 2 resonances are around 10 GHz and 15 GHz.

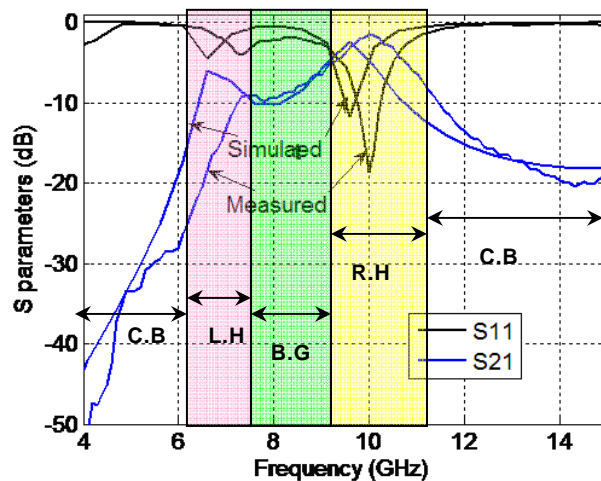


Figure 4.26 Measured and simulated S parameters of CRLH MTM on YIG, unit length 4195 μm , IDC finger length 75 μm , inductor length 650 μm (13)

In Figure 4.26 and Figure 4.27, 2 resonances exist in figures of S parameter; for the CRLH MTM on YIG with unit length 4195 μm , one resonance around 7.3 GHz, and the other around 10 GHz; for which unit length 10195 μm , 3 resonances exist around 5.2 GHz, 12 GHz, and 14 GHz. The IDC finger lengths of the 2 CRLHs are 75 μm and 100 μm respectively, the shunt induc-

tance length is $650 \mu\text{m}$. It's quite evident that, with a longer unit length (CPW2), the CRLH MTM has a lower resonance frequency.

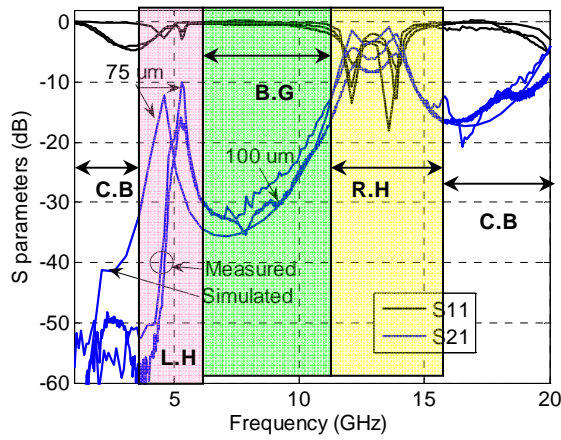


Figure 4.27 Measured and simulated S parameters of CRLH MTM on YIG, unit length $10195 \mu\text{m}$, IDC finger length $75 \mu\text{m}$, inductor length $650 \mu\text{m}$ (sample 9 12)

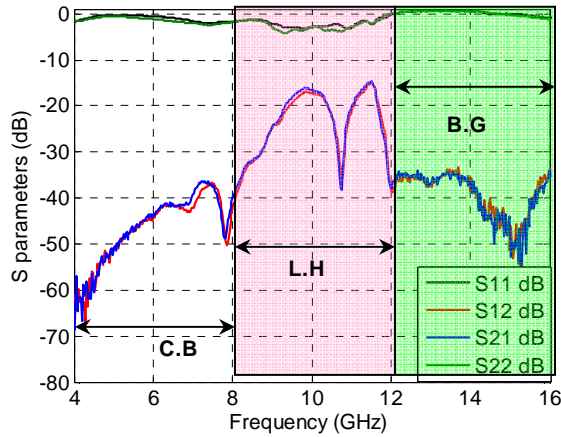


Figure 4.28 Measured S parameters of 8-unit CRLH MTM on YIG, unit length $4220 \mu\text{m}$, IDC finger length $75 \mu\text{m}$, inductor length $650 \mu\text{m}$ (sample 6)

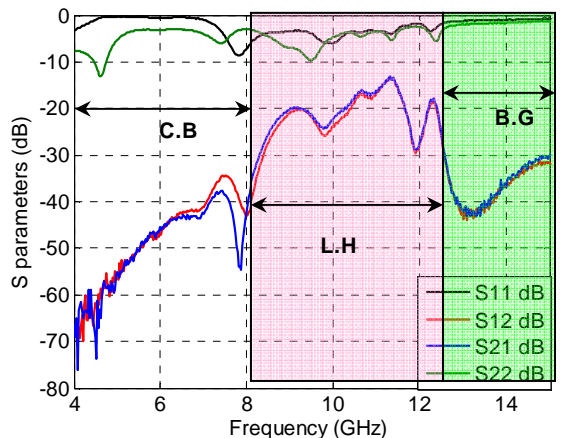


Figure 4.29 Measured S parameters of 8-unit CRLH MTM on YIG, unit length $4220 \mu\text{m}$, IDC finger length $100 \mu\text{m}$, inductor length $650 \mu\text{m}$ (5)

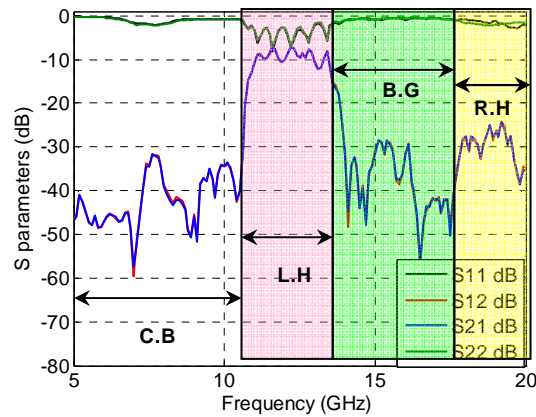


Figure 4.30 Measured S parameters of 8-unit CRLH MTM on YIG, unit length 3020 μm , capacitor gap 10 μm , inductor length 1150 μm (21)

The S parameters of 8-unit CRLH MTM on YIG are shown in Figure 4.28, Figure 4.29, and Figure 4.30. For the CRLH with unit length 4220 μm , IDC finger length 75 μm , inductor length 650 μm , the passband is around 12 GHz. For the one unit length 4220 μm , IDC finger length 100 μm , inductor length 650 μm , the passband is around 11.5 GHz. For the one with unit length 3020 μm , capacitor gap 10 μm , inductor length 1150 μm , the passband is around 12.5 GHz.

4.4.3 Propagation constants

The propagation constants $\gamma = \alpha + j\beta$ of CRLH MTM on YIG can be calculated by method presented in Section 4.3. The dispersion diagrams of the CRLH MTM on YIG are shown in figures below. From these dispersion diagram that we can establish that the bands for samples on YIG are shifted to lower frequencies, with respect to equivalent samples on alumina. The values of capacitances C_R and C_L on YIG are indeed larger than those on alumina.

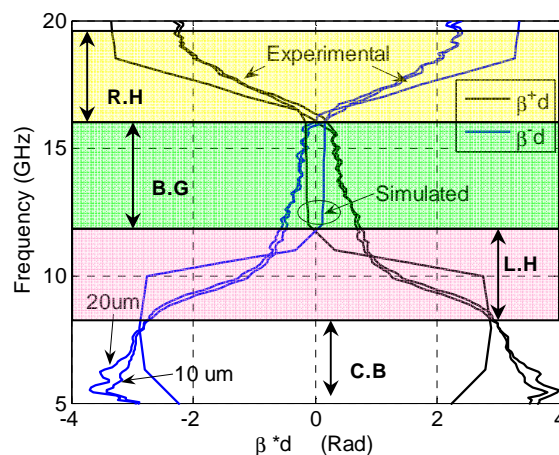


Figure 4.31 Propagation constants of CRLH MTM on YIG, unit length 1520 μm , capacitor gap 20 μm , inductor length 1150 μm (sample 16 20 inl)

As shown in Figure 4.31, for the 2 CRLH MTM on YIG with gap capacitance, the frequencies of frequency of $\min(f_{se}, f_{sh})$ are about 12, the left-hand frequency band is obtained around 10 GHz, where the slope of β as a function of frequency is negative.

We change the unit length of CRLH MTM on YIG from 1520 μm to 2195 μm , and change the length of shunt inductance from 1150 μm to 650 μm . The corresponding propagation constants are shown in Figure 4.32. The frequencies of frequency of $\min(f_{se}, f_{sh})$ are around 15 GHz, the LH frequency band is also observed around 10 GHz.

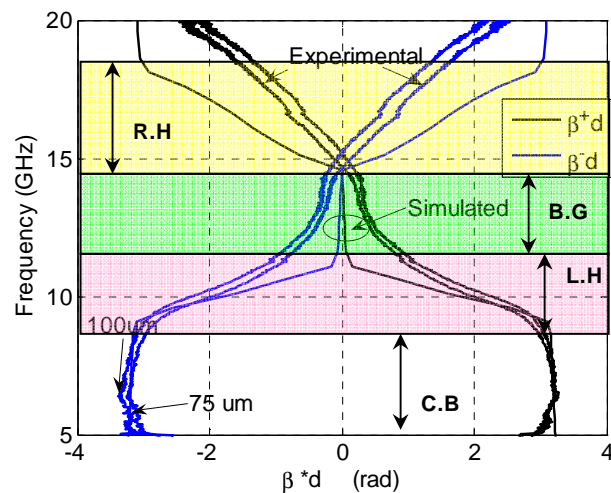


Figure 4.32 Propagation constants of CRLH MTM on YIG, unit length 2195 μm , IDC finger length 75 μm and 100 μm , inductor length 650 μm (sample 7 10)

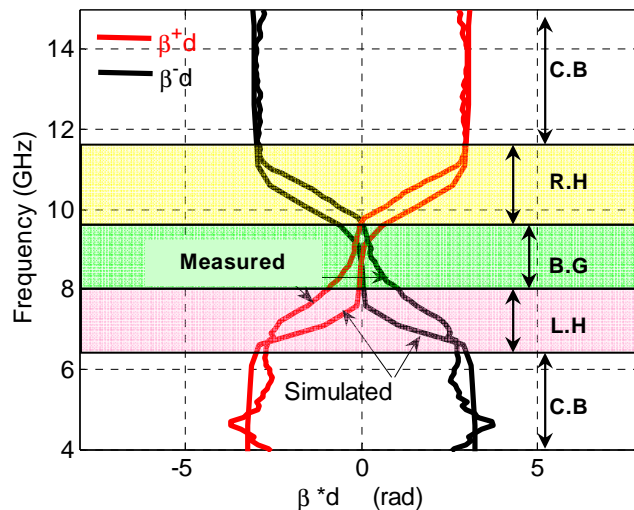


Figure 4.33 Propagation constants of CRLH MTM on YIG, unit length 4195 μm , IDC finger length 75 μm , inductor length 650 μm (sample 13)

Then, we change the unit length of CRLH MTM from 2195 μm to 4195 μm , in Figure 4.33, the frequency of frequency of $\min(f_{se}, f_{sh})$ is about

7.5 GHz, the LH frequency band is observed around 7 GHz, where the slope of β to frequency is negative

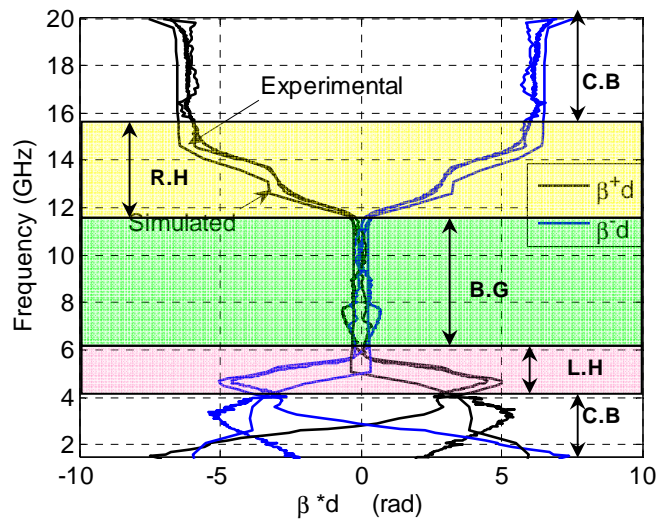


Figure 4.34 Propagation constants of CRLH MTM on YIG, unit length 10195 μm , IDC finger length 75 μm , inductor length 650 μm (sample 9 12)

As shown in Figure 4.34, when the unit length of CRLH MTM changes from 4195 μm to 10195 μm , the transition frequency f_0 changes from about 7.5 GHz to about 5.5 GHz, the LH frequency band changes from around 7 GHz to about 5 GHz; the RH frequency band is around 13 GHz, where the slope of β to frequency is positive.

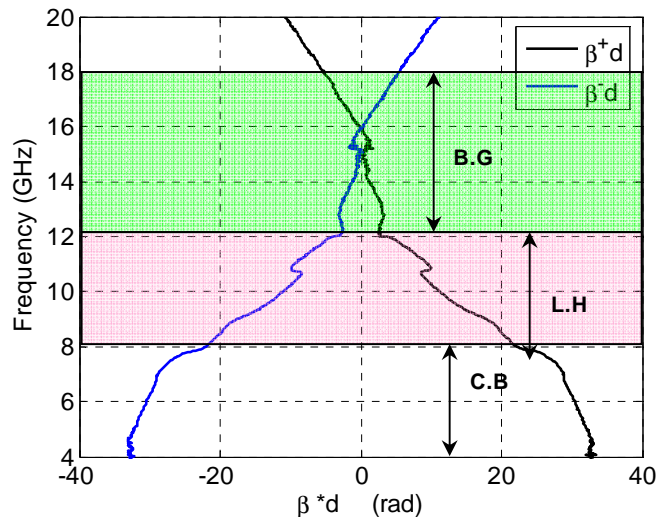


Figure 4.35 Propagation constants of 8-unit CRLH MTM on YIG, unit length 4220 μm , IDC finger length 75 μm , inductor length 650 μm (sample 6)

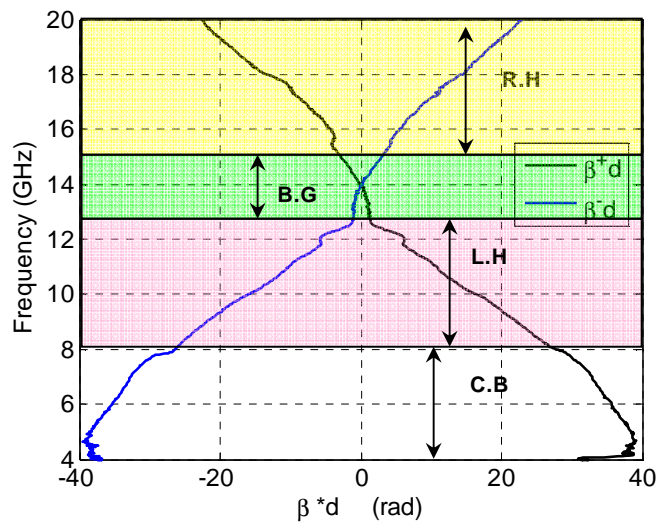


Figure 4.36 Propagation constants of 8-unit CRLH MTM on YIG, unit length 4220 μm , IDC finger length 100 μm , inductor length 650 μm (sample 5)

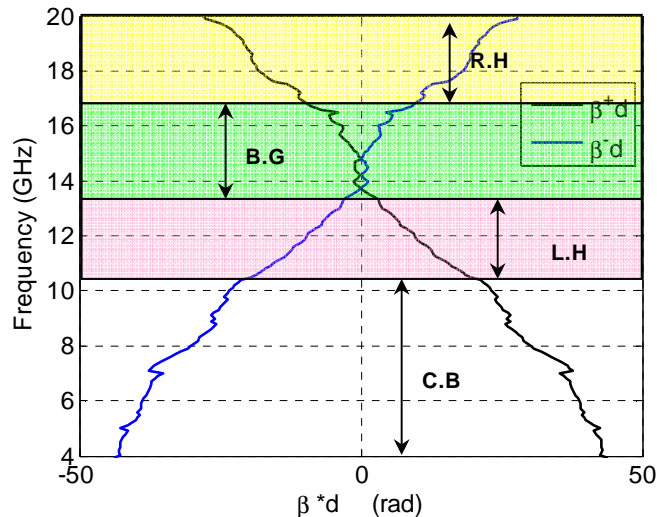


Figure 4.37 Propagation constants of 8-unit CRLH MTM on YIG, unit length 3020 μm , capacitor gap 10 μm , inductor length 1150 μm (sample 21)

The propagation constants of 8-unit CRLH MTM on YIG are shown in Figure 4.35, Figure 4.36 and Figure 4.37. For the CRLH with unit length 4220 μm , IDC finger length 75 μm and inductor length 650 μm , the LH frequency band around 10 GHz is obtained, $\beta = 0$ at about 14.5 GHz. For the CRLH with unit length 4220 μm , IDC finger length 100 μm and inductor length 650 μm , the LH frequency band is around 10 GHz, $\beta = 0$ at about 14 GHz. For the one with unit length 3020 μm , capacitor gap width 10 μm and inductor length 1150 μm , the LH frequency band is around 10 GHz, $\beta = 0$ at about 14 GHz.

4.5 CRLH on YIG with applied field

The CRLH MTM on ferrite YIG with applied field in y direction will be studied in this section. At the beginning, samples with applied field fixed 130 kA/m and 140 kA/m are studied, then a typical sample with different applied fields is studied, the S parameters and propagation constants are given.

4.5.1 Measured and simulated S parameters

For the samples with 1-unit cell under field, what we observe on the S parameters that we didn't have previously, is the gyroresonance and frequencies slightly higher than the gyroresonance (6-9 GHz under applied field 140 kA/m), where the tensor of permeability has negative terms. The 2 resonance frequencies due to the structure CRLH, f_{sh} and f_{se} are shifted to higher frequency compared to YIG without applied field. This is due to the fact that under field, due to the negative permeability, a series capacitance C_X adds up to C_L (see chapter 3), the equivalent capacitance is smaller than C_L , so there is a increase in the resonance frequency, compared to the case without applied field. As a consequence, the bandwidth of bandgap decreases with field compared to without field. The nonreciprocal effect due to the negative permeability terms can be observed whether in the left-handed band (sample 16), in the bandgap (sample 9) or in the crystal band (sample 20) depending on the sample geometry. When we have several cells the cut of frequencies are sharper than for one cell components, and the effect of nonreciprocity is also observed.

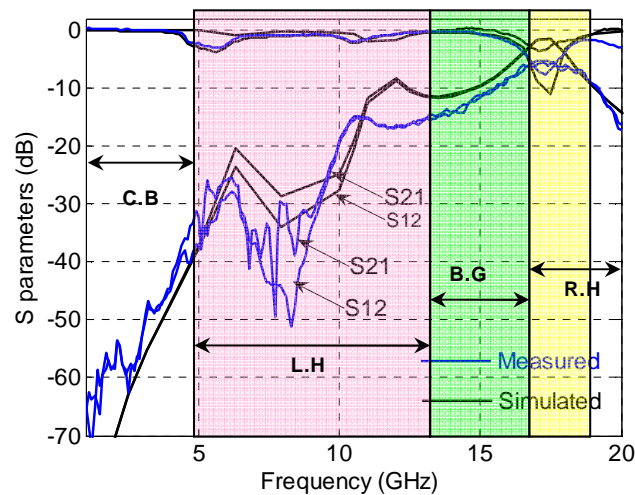


Figure 4.38 Measured and simulated S parameters CRLH MTM on YIG with applied field 130 kA/m, unit length 1520 μm , capacitor gap 20 μm , inductor length 1150 μm (sample 16)

The measured S parameters of CRLH MTM on YIG substrate with applied field 130kA/m are shown in Figure 4.38. The 1-unit CRLH MTM on YIG substrate with applied field is a nonreciprocal structure, the gyroresonance frequency is around 6 GHz, the nonreciprocity between S_{21} and S_{12} is about 20 dB

at 8 GHz; the other 2 resonance frequencies are around 11 GHz and 15.8 GHz; for the frequencies up 15 GHz, the S parameters of CRLH with applied field are almost the same as that of CRLH without applied fields.

We can find in the Figure 4.39 that, for a 1-unit CRLH MTM on YIG substrate with applied field 140 kA/m, it's a nonreciprocal structure, the gyroresonance frequency is around 6 GHz, S_{21} is different from S_{12} around 8 GHz (a little higher than gyroresonance frequency); the other 2 resonance frequencies are around 11 GHz and 15.8 GHz.

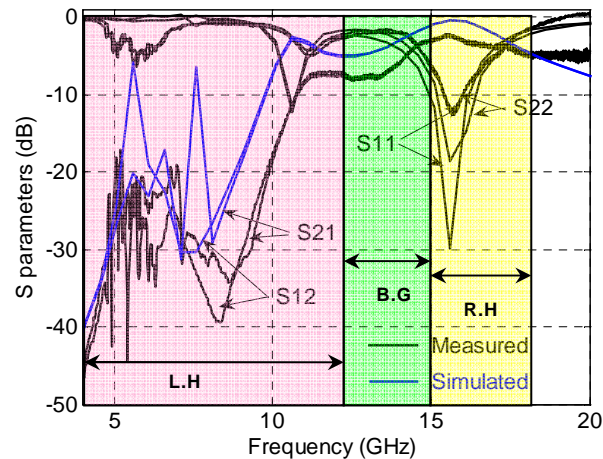


Figure 4.39 Measured and simulated S parameters of CRLH MTM on YIG with applied field 140 kA/m, unit length 2195 μm , IDC finger length 75 μm , inductor length 650 μm (sample 7)

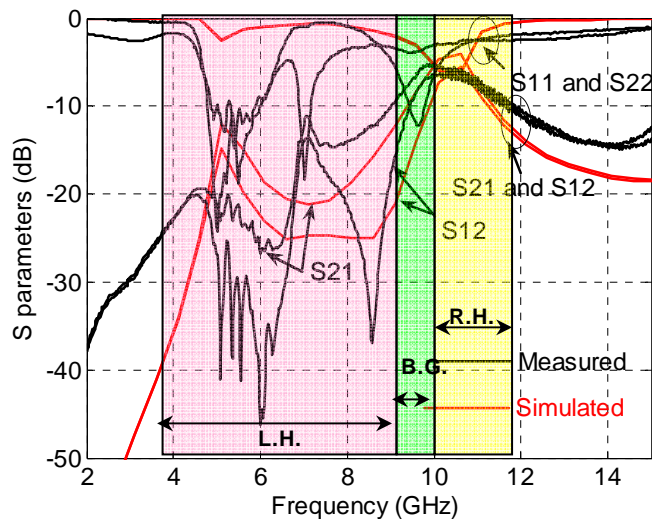


Figure 4.40 Measured and simulated S parameters of CRLH MTM on YIG with applied field 140 kA/m, unit length 4195 μm , IDC finger length 75 μm , inductor length 650 μm (13)

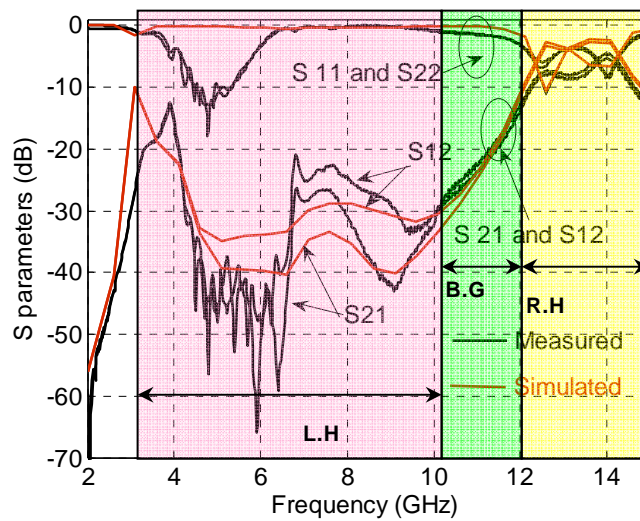


Figure 4.41 Measured and simulated S parameters of CRLH MTM on YIG with applied field 140 kA/m, unit length 10195 μm , IDC finger length 75 μm , inductor length 650 μm (sample 9)

For the CRLH with unit length 4195 μm , IDC finger length 75 μm , inductor length 650 μm , the gyroresonance frequency is around 5.5 GHz, the difference between S_{21} and S_{12} is about 8 dB around 6 GHz, and 22dB around 8.2 GHz, as shown in Figure 4.40. For the CRLH with unit length 10195 μm , IDC finger length 75 μm , inductor length 650 μm , the gyroresonance frequency is around 5 GHz, the difference of S_{21} and S_{12} is about 20 dB around 6.5 GHz, and 7 dB around 9 GHz; which can be seen in Figure 4.41. At the frequencies apart from the gyroresonance frequencies, the S parameters of CRLH with applied field are almost the same as that of the CRLH without applied fields.

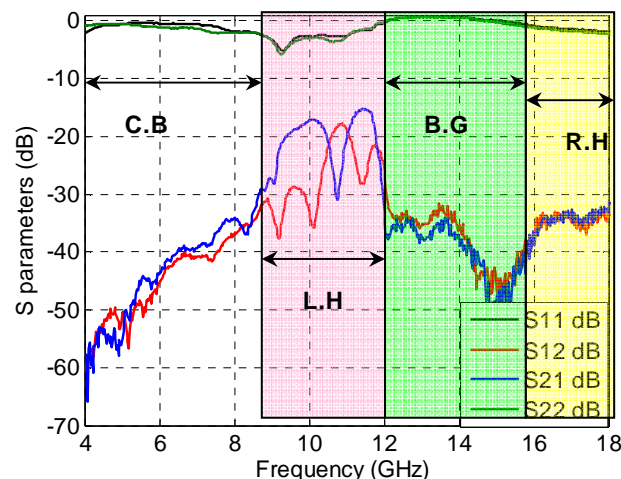


Figure 4.42 Measured S parameters of 8-unit CRLH MTM on YIG with applied field 140 kA/m, unit length 4220 μm , IDC finger length 75 μm , inductor length 650 μm (sample 6)

For the 8-unit CRLH MTM on YIG with applied field 140 kA/m, the measured S parameters are shown in Figure 4.42, Figure 4.43, and Figure 4.44. For the CRLH with unit length 4220 μm , IDC finger length 75 μm , inductor length 650 μm , the difference between S_{21} and S_{12} is 20 dB around 10 GHz. For the CRLH with unit length 4220 μm , IDC finger length 100 μm , inductor length 650 μm , the difference between S_{21} and S_{12} is 9 dB around 10 GHz. For the CRLH with unit length 3020 μm , capacitor gap 10 μm , inductor length 1150 μm , the difference between S_{21} and S_{12} is 20 dB around 9.3 GHz.

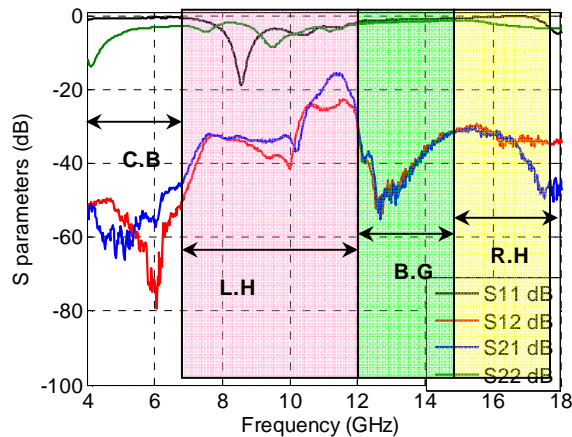


Figure 4.43 Measured S parameters of 8-unit CRLH MTM on YIG with applied field 140 kA/m, unit length 4220 μm , IDC finger length 100 μm , inductor length 650 μm (sample 5)

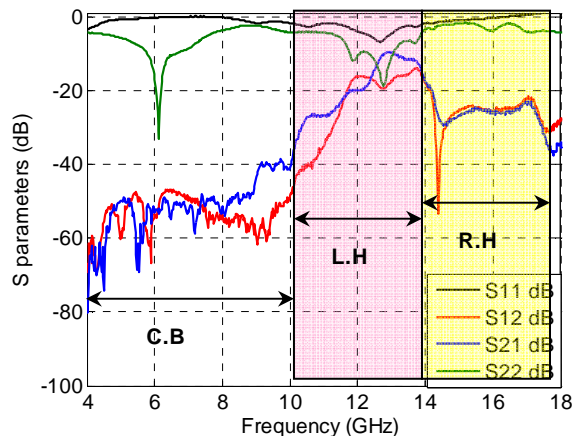


Figure 4.44 Measured S parameters of 8-unit CRLH MTM on YIG with applied field 140 kA/m, unit length 3020 μm , capacitor gap 10 μm , inductor length 1150 μm (sample 21)

On sample 20, we are going to show the influence of the applied field on the S parameters (Figure 4.45), and on the beta (Figure 4.53).

In Figures 4.45, when the applied field increases from 60 kA/m to 130 kA/m, the gyroresonance frequency increases from 3 GHz to 5.5 GHz, the difference between S_{21} and S_{12} increases from 20 dB to 30 dB; in general, the gy-

resonance frequencies and the difference between S_{12} and S_{21} parameters increase with applied field increase.

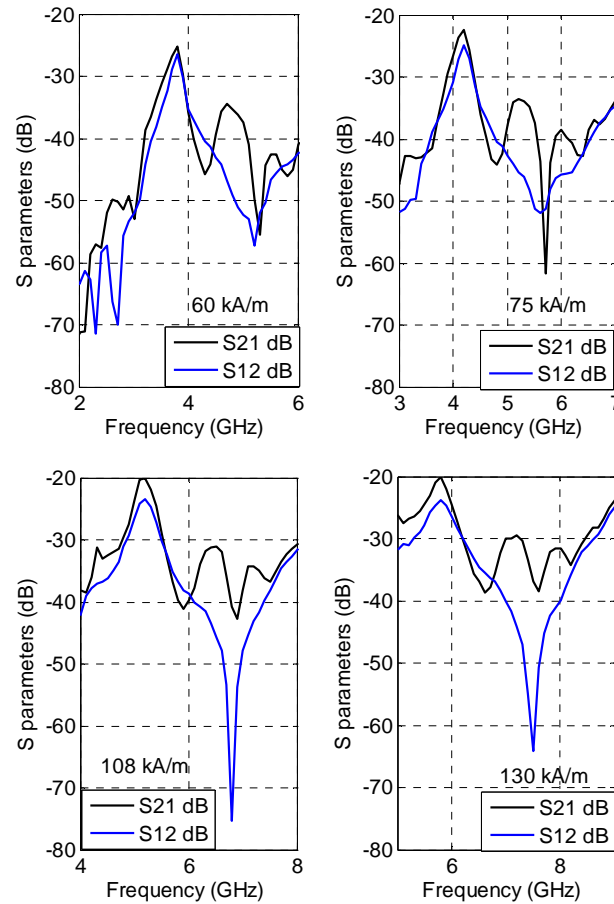


Figure 4.45 Zoom around the gyroresonance on the measured S_{21} and S_{12} parameters with different applied fields. Unit length $1520 \mu\text{m}$, capacitor gap $10 \mu\text{m}$, inductor length $1150 \mu\text{m}$ (sample 20 comparable to sample 16)

Under field of 130 kA/m , the components have an enhanced nonreciprocal effect, compared to a standard CPW. In this work, we obtain the highest nonreciprocity that reaches 30 dB (Figure 4.45 under the highest field). At the end of chapter 3, we had already reported an enhanced nonreciprocity of 20 dB when inductors are inserted to the CPW. Note that the transmission parameters for the CRLH on YIG are smaller than the CPW with inductors.

4.5.2 Propagation constants

The dispersion diagrams of the CRLH MTM on YIG with applied field are studied in this section, the propagation constants $\gamma = \alpha + j\beta$ can be calculated by method presented in Section 4.3. In Figure 4.46, for 1-unit CRLH MTM on YIG with applied field 130 kA/m , unit length $1520 \mu\text{m}$, and capacitance gap $20 \mu\text{m}$, $\beta = 0$ at about 16.5 GHz ; $\beta^+ d$ are different from $\beta^- d$ in the frequency

band 6.5 to 11 GHz due to the anisotropy of the permeability of ferrite, the difference between β^+d and β^-d is about 2 rad around 7.8 GHz, the LH bands are obtained around 11 GHz. For the one with capacitance gap 10 μm , $\beta = 0$ at about 16 GHz, the difference between β^+d and β^-d is about 1.5 rad around 7 GHz, the LH bands are obtained around 5 GHz and 11 GHz.

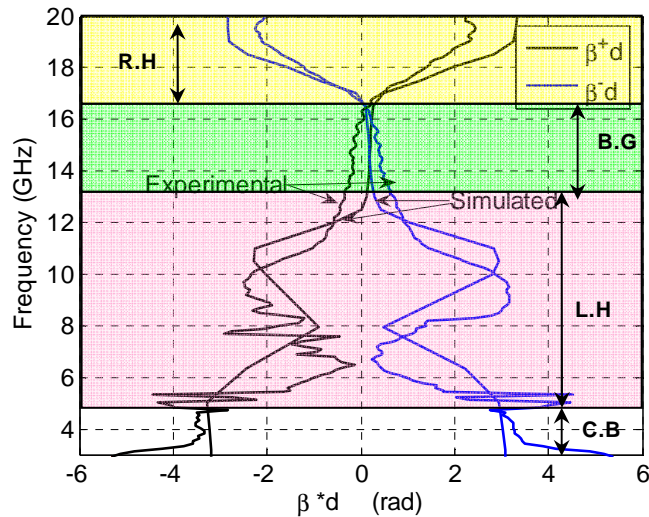


Figure 4.46 Propagation constants of CRLH MTM on YIG with applied field 130 kA/m, unit length 1520 μm , capacitor gap 20 μm , inductor length 1150 μm (sample 16)

In Figure 4.47, for 1-unit CRLH MTM on YIG with applied field 140 kA/m, unit length 2195 μm , IDC finger length 75 μm , inductor length 650 μm , $\beta = 0$ at about 15 GHz, the difference between β^+d and β^-d is about 6 rad around 7 GHz, a LH band is obtained around 11 GHz.

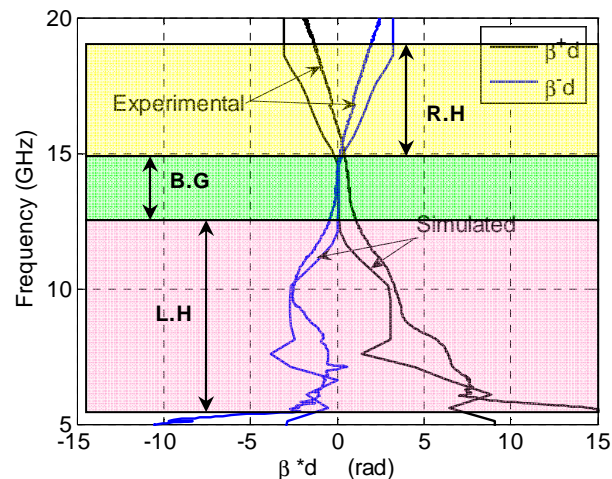


Figure 4.47 Propagation constants of CRLH MTM on YIG with applied field 140 kA/m, unit length 2195 μm , IDC finger length 75 μm , inductor length 650 μm (sample 7 10)

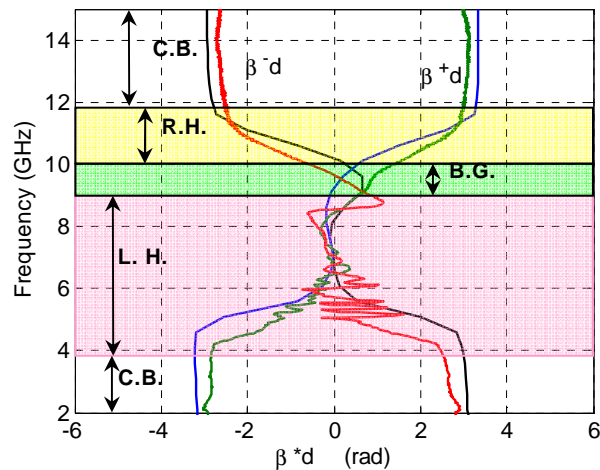


Figure 4.48 Propagation constants of CRLH MTM on YIG with applied field 140 kA/m, unit length 4195 μm , IDC finger length 75 μm , inductor length 650 μm (sample 13)

Figure 4.48 shows that, for 1-unit CRLH MTM on YIG with applied field 140 kA/m, unit length 4195 μm , IDC finger length 75 μm , inductor length 650 μm , the difference between β^+d and β^-d is about 2 rad around 7 GHz, a LH band is obtained at frequency band 4- 9GHz.

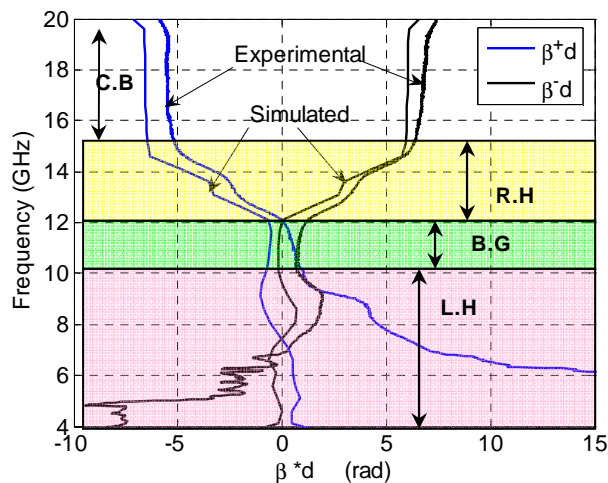


Figure 4.49 Propagation constants of CRLH MTM on YIG with applied field 140 kA/m, unit length 10195 μm , IDC finger length 75 μm , inductor length 650 μm (sample 9 12)

Sample 9 has the longest unit length (CPW2), and consequently the lowest upper limit for the left-handed band without field. In Figure 4.49, due to the effect of gyroresonance, a new nonreciprocal left-handed band is observed at frequencies that were previously, in the case without field, in the bandgap (see Figure 4.34). $\beta = 0$ upon 10 GHz, the difference between β^+d and β^-d is about 3 rad around 8 GHz, a LH band is obtained around 7 GHz. For 1-unit CRLH MTM with unit length 10195 μm , IDC finger length 100 μm , inductor

length $650 \mu\text{m}$, $\beta = 0$ around 10 GHz , the difference between β^+d and β^-d is about 1 rad around 8.5 GHz , a LH band is obtained around 8 GHz .

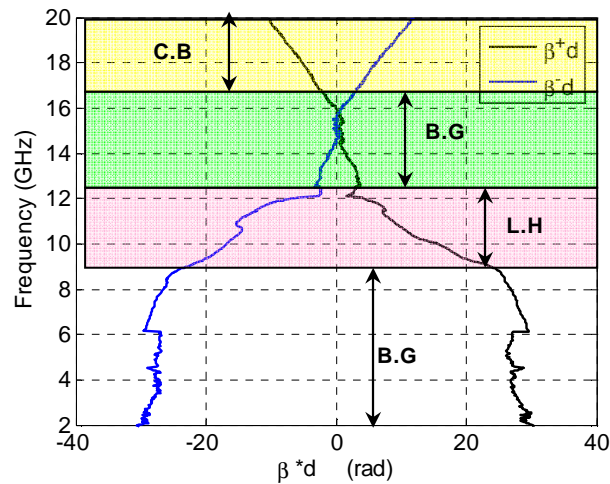


Figure 4.50 Propagation constants of CRLH MTM on YIG with applied field 140 kA/m , unit length $4220 \mu\text{m}$, IDC finger length $75 \mu\text{m}$, inductor length $650 \mu\text{m}$ (sample 6)

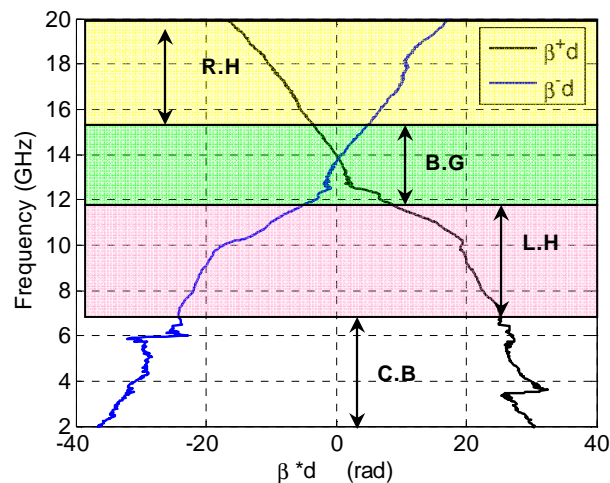


Figure 4.51 Propagation constants of CRLH MTM on YIG with applied field 140 kA/m , unit length $4220 \mu\text{m}$, IDC finger length $100 \mu\text{m}$, inductor length $650 \mu\text{m}$ (sample 5)

Figure 4.50 indicates that, for the 8-unit CRLH MTM with unit length $4220 \mu\text{m}$, IDC finger length $75 \mu\text{m}$, inductor length $650 \mu\text{m}$, $\beta = 0$ around 15 GHz , the difference between β^+d and β^-d is about 2 rad around 10 GHz , a LH band is obtained around 10 GHz . For the one with IDC finger length $100 \mu\text{m}$, $\beta = 0$ around 14 GHz , the difference between β^+d and β^-d is about 1 rad around 10 GHz , a LH band is obtained around 10 GHz , as shown in Figure 4.51. For the one with unit length $3020 \mu\text{m}$, capacitor gap $10 \mu\text{m}$, inductor length $1150 \mu\text{m}$, $\beta = 0$ around 14 GHz , the difference between β^+d and β^-d is about 1 rad around 9 GHz , a LH band is obtained around 12 GHz , which can be seen in Figure 4.52.

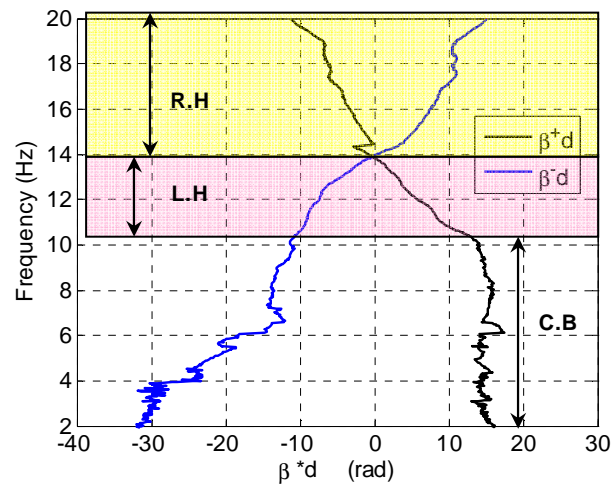


Figure 4.52 Propagation constants of CRLH MTM on YIG with applied field 140 kA/m, unit length 3020 μm , capacitor gap 10 μm , inductor length 1150 μm (sample 21)

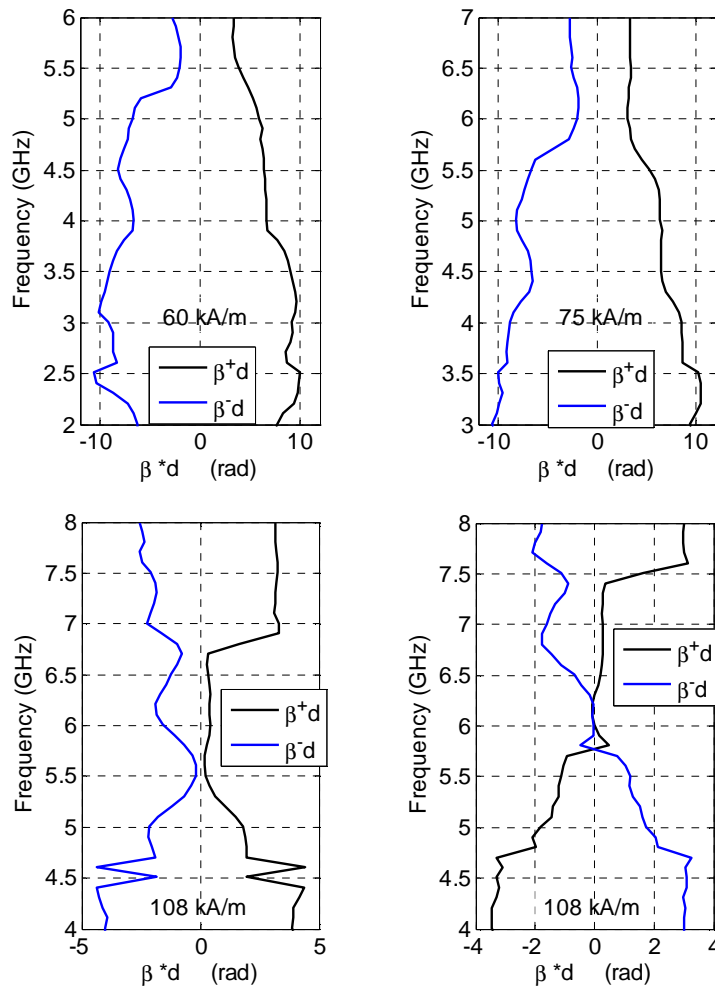


Figure 4.53 Zoom around the gyroresonance on the propagation constants of CRLH MTM on YIG with different applied field, Unit length 1520 μm , capacitor gap 20 μm , inductor length 1150 μm (sample 20)

A zoom on the propagation constants of CRLH MTM on YIG with different applied field are shown in Figure 4.53, the difference of $\beta^+ d$ and $\beta^- d$ (non-reciprocity) increases with the applied field increases. With a big applied field (108 kA/m and 130 kA/m), a new LH frequency band is obtain at frequency band below 5.5 GHz and 6 GHz respectively, and a new LH frequency band is obtained at frequency band higher than 5.5 GHz and 6 GHz respectively. Where previously without applied field, we had a crystal band.

4.6 Conclusions

In this chapter, the modelling of CRLH transmission line and the CRLH transmission line theory have been presented. Then a parametric study of this components on alumina and on YIG (with and without field) has been driven. The geometric parameters were the left-handed inductances, left-handed capacitances and the length of the CPW separating them (CPW2). Both experimental and simulated scattering parameters are shown, and the corresponding propagation constants are given, that enables to identify the different frequency bands: left-handed band, right-handed band and bandgap.

On alumina, the cutoff frequencies f_{se} and f_{sh} which are due to the structure CRLH, are comprised between 5 and 20 GHz depending on the length of CPW2, the series capacitance C_L and shunt inductance L_L . An increase in L_L and C_L reduce the resonance frequencies, an increase of CPW2 also acts towards a decrease of the resonance frequencies. When the number of cells increases, the cutoff frequency become sharper.

On YIG substrate without field, due to the increase of the equivalent permittivity, all the bands identified previously are shifted to lower frequencies. The behaviour of these components and the preceding ones is reciprocal.

On YIG substrate with field, there is a nonreciprocal behaviour, due to the anisotropy of the permeability tensor of ferrite. Depending on the geometry of the components, the nonreciprocity due to the negative permeability terms is located whether in the left-handed band, in the bandgap or in the crystal band. Just above the gyroresonance frequency, the terms of permeability tensor are negative. As a consequence, the resonance frequency (f_{sh} or f_{se}) which is the closest to the gyroresonance frequency, but higher to it, is shifted to higher frequency compared to YIG without applied field. In fact, under field, due to the negative permeability, a series capacitance C_X adds up to C_L , resulting in an equivalent capacitance smaller than C_L , so there is an increase in the resonance frequency, compared to the case without applied field. We note a decrease of the bandgap bandwidth with the field compared with the case without the field. When we have several cells the cut of frequencies are sharper than for one cell components, and the effect of nonreciprocity is also observed.

Finally, under field of 130 kA/m, the CRLH components have an enhanced nonreciprocal effect, compared to a standard CPW, we obtain the highest nonreciprocity that reaches 30 dB. When only inductors are inserted into the CPW, we had an enhanced nonreciprocity of 20 dB with transmission parameter -7dB.

4.7 Bibliography

- [1] **CALOZ C., ITOH T.** « Electromagnetic metamaterials: transmission line theory and microwave applications », Wiley-IEEE Press, 2005, 376 p.
- [2] **CUI T.J., DAVID S., LIU R.P.** « Metamaterials: theory, design and applications », Springer, 2009, 392 p.
- [3] **LAI A., CALOZ C., ITOH T.** Composite right/left-handed transmission line metamaterials, IEEE microwave magazine, 2004, pp.34 – 50.
- [4] **SANDADA A., CALOZ C., ITOH T.** Novel Zeroth-order resonance in composite right/left-handed transmission line resonators, 2003 Asia-Pacific Microwave Conference.
- [5] **CALOZ C., ITOH T.** Transmission line approach of left-handed (LH) materials and microstrip implementations of an artificial lh transmission line, IEEE transactions on antennas and propagation, Vol.52, No.5, 2004, pp. 1159 - 1166.
- [6] **KIM T.-G., Lee B.** Metamaterial-based compact zeroth-order resonant antenna, Electronics Letters, Vol. 45, No.1, 2009, pp. 12 - 13.
- [7] **CHANG W.-C., Lee, B.** Wideband one-unit-cell ENG zeroth-order resonant antenna, Electronics Letters, Vol. 45, No. 25, 2009, pp. 1289 - 1291.
- [8] **ALLEN C.A., LEONG K.M.K.H. ITOH T.** Dual-mode composite-right/left-handed transmission line ring resonator, Electronics Letters, Vol. 42, No.2, 2006, pp. 96 - 97.
- [9] **ZHOU T., SUN B. H., LIU Q. Z., LI J. F., XU Z.** Novel compact circularly polarized microstrip antenna using left-handed transmission lines, J. of Electromagn. Waves and Appl., Vol. 22, 2008, pp. 625 - 634.
- [10] **CALOZ C., ITOH T.** Application of the transmission line theory of left-handed (LH) materials to the realization of a

microstrip "LH line", IEEE antennas and propagation society international symposium, Vol. 2, 2002, pp. 412-415.

- [11] **SMITH D. R., PENDRY J. B., WILTSHIRE M. C. K.**
Metamaterials and negative refractive index, Science, Vol. 305, No. 5685, 2004, pp. 788-792.

- [12] **CUI T. J., MA H. F., LIU R., ZHAO B., CHENG Q., CHIN J. Y.** A symmetrical circuit model describing all kinds of circuit metamaterials, Progress In Electromagnetics Research B, Vol. 5, 2008, pp. 63-76.

- [13] **ELEFThERIADES G.V., IYER A.K., KREMER P.C.**
Planar negative refractive index media using periodically L-C loaded transmission lines. IEEE Transactions on microwave theory and techniques, Vol. 50, No. 12, 2002, pp. 2702-2712.

General conclusion

In this thesis we studied some passive components based on metamaterials. Our goal was to assess the physical properties of CRLH lines combined with a ferrite substrate. When the CRLH TLs are integrated with ferrite substrate, new properties based on the “CRLH” structure and nonreciprocity of ferrite can be obtained. Samples were processed on dielectric substrate (alumina) as well as on YIG substrate, according to fabrication steps which are described in this work. These samples have been characterized, in particular for the YIG substrate, with and without a magnetic polarization field. 3D Finite element simulation was used to get the scattering parameters. Lastly, dispersion diagrams were extracted from both measured and simulated data. We can get nonreciprocity by modeling the ferrite substrate, and “left-handed” property by modeling the structure of CRLH.

The first chapter of this manuscript focuses on theories of microwave transmission lines, coplanar waveguides, magnetic materials and metamaterials. We began with the theories of traditional transmission lines and non-reciprocal transmission lines, and then we presented transmission lines analysis, methods of calculation of the parameters characterizing wave propagation (matrix $[Z]$ matrix $[Y]$, matrix $[ABCD]$ and matrix $[S]$). Regarding the magnetic materials, we present the different groups they belong to. Finally, we introduced the metamaterials. The definition, history, and applications of metamaterials in microwave and millimetre wave were discussed.

In the second chapter, we designed and implemented conventional CPW components as well as stand-alone capacitors and inductors on alumina substrate. We completed the fabrication process in NANOLYON. Then the simulations in software COMSOL and the analytical modelling approaches in Matlab are presented. The measured, simulated and analytical S parameters are given, the corresponding propagation constants of CPW, the extracted values of capacitance and inductance are given and discussed. For the gap capacitors, the highest capacitance is obtained when the gap is 10 μm , and it reaches 60 fF. A slightly larger value of the capacitance is obtained for a 5 finger IDC that reaches 80 fF. The overlap length between 2 fingers is then 90 μm . For the inductances, measured values of inductances of 200 and 400 pH can be measured for a length of 650 to 1150 μm respectively.

The CPW components on ferrite are introduced in the third chapter. Firstly, different kinds of ferrite and the fabrication of components are presented. Then the modelling of permeability of ferrite material is detailed, and implemented in the 3D finite element simulation. The nonreciprocity is studied using CPW components based on ferrite BaM and YIG. For CPW on ferrite substrate, the measured and simulated S parameters, as well as propagation con-

stant are given. For coplanar capacitors on YIG, the measured and simulated S parameters, and corresponding capacitors values are obtained outside the gyroresonance region. For gap capacitors, the highest value is 0.11 pF and for interdigital capacitor 0.19 pF. For coplanar inductors on YIG, the measured S parameters without applied field and with applied field are given. The series capacitance due to the negative permeability of YIG is introduced, and the equivalent circuit of the structure is given, as well as an estimated dispersion diagram. Finally, the nonreciprocity of the components on YIG with applied field is increased to 20 dB if the CPW is loaded with shunt inductors, which is much higher than that of standard CPW.

In chapter four, the modelling of CRLH transmission line and the CRLH transmission line theory were presented. This type of TL allows a negative phase velocity in the so-called left-handed frequency band. Examples of balanced and unbalanced CRLH TL are presented and the dispersion diagram is given. Then a parametric study of the components realized on alumina and on YIG (with and without field) has been driven. The geometric parameters were the left-handed inductances, left-handed capacitances and the length of the CPW separating them (equivalent to a unit-cell length, denoted CPW2). Both experimental and simulated scattering parameters are shown and the corresponding propagation constants are given. That enables to identify different frequency bands: left-handed band, right-handed band and bandgap. Moreover, we establish that the band structure of these components can be tuned with the magnetic applied field.

On alumina substrate, the cutoff or resonance frequencies f_{se} and f_{sh} which are due to the structure CRLH, are comprised between 5 and 20 GHz depending on the length of CPW2, the series capacitance C_L and shunt inductance L_L . An increase of L_L , C_L or the length of CPW2 also acts towards a decrease of the resonance frequencies. When the number of cells increases, the cutoff frequencies become sharper. On YIG substrate without field, all the bands identified previously are shifted to lower frequencies.

On YIG substrate with field, there is a nonreciprocal behaviour, due to the anisotropy of the permeability tensor of ferrite. The nonreciprocity is located whether in the left-handed band, in the bandgap or in the crystal band, depending on the geometry of the components. Under field, there is an increase of a resonance frequency, and a decrease of the bandgap bandwidth. Indeed, when the terms of permeability tensor are negative, a series capacitance C_X adds up to C_L , resulting in an equivalent capacitance smaller than C_L . When we have several cells the cutoff or resonance frequencies are sharper than for one cell components and the effect of nonreciprocity is also observed.

Finally, under field of 130 kA/m, the CRLH components have an enhanced nonreciprocal effect, compared to a standard CPW, the highest nonre-

reciprocity reaches 30 dB. When only inductors are inserted into the CPW, we had an enhanced nonreciprocity of 20 dB with transmission parameter -7dB .

In this thesis, the equivalent series capacitors are tuned by magnetic applied field. As a perspective, we can also use the varactors with bias network to replace the series capacitors in CRLH. The varactor diodes can be used as tunable capacitors, the capacitance of the varactor diodes can be controlled by the applied reverse voltage of bias network. Many novel properties can be obtained by the varactors, which are interesting for some non linear active components like phase shifter and leaky-wave antenna.

List of publications

Journal

[1] T. Zhou, M. Le Berre, E. Benevent, A.-S. Dehlinger, F. Calmon, E. Verney, S. Perrot, B. Payet-Gervy, Coplanar waveguides with or without barium ferrite thin films; Microwave and Optical Technology Letters, Vol. 52, No 9, 2010, pp. 2007-2010.

Conferences

[1] T. Zhou, M. Le Berre, F. Calmon, D. Vincent; Anisotropic Composite Right/Left-handed Transmission Line Metamaterials with Ferrite Substrate; 29^{èmes} Progress in Electromagnetic Research Symposium, 20-23 March 2011, Marrakesh, Morocco. EI source

[2] F. Boukchiche, T. Zhou, M. Le Berre, D. Vincent; Novel composite non reciprocal right/left-handed line made from ferrite material; 28^{èmes} Progress in Electromagnetic Research Symposium; 5-8 Juillet 2010, Cambridge, USA. EI source

[3] T. Zhou, E. Benevent, M. Le Berre; Caractérisation expérimentale et modélisation de guides d'ondes coplanaires avec et sans couche de ferrite; 16^{èmes} Journées Nationales Microondes, 27-29 Mai 2009, Grenoble, France.

[4] T. Zhou, E. Benevent, M. Le Berre ; Guides d'ondes et isolateurs coplanaires pour applications hautes fréquences ; 12^{èmes} Journées Nationales du Réseau Doctoral de Microélectronique; 18-20 Mai 2009, Lyon, France.

[5] T. Zhou, M. Le Berre, F. Calmon, D. Vincent; Applications des ferrites et des métamatériaux aux lignes de transmission coplanaires; 13^{èmes} Journées Nationales du Réseau Doctoral de Microélectronique; 7-9 Juin 2010, Montpellier, France, France.

[6] F. Boukchiche, B. Payet-Gervy, D. Vincent, T. Zhou; Milieu non réciproque à indice négatif en structure planaire; 11^{èmes} Journées de Caractérisation Micro-ondes et Matériaux; 31 Mars-2 avril 2010, Brest, France.

[7] T. Zhou, E. Benevent, M. Le Berre; Caractérisation expérimentale et modélisation de guides d'ondes coplanaires avec et sans couche de ferrite; 2^{èmes} colloque du LIA-LN2, 1-3 Juillet, 2009, Domaine Bellevue - Anse - et Hôtel de Ville de Lyon, France.